UNIVERSITY OF OKLAHOMA

GRADUATE COLLEGE

METEOROLOGICAL BENEFITS OF DUAL-POLARIZATION,

RAPID-SCANNING RADAR SYSTEMS ON HAIL PRODUCING STORMS

A THESIS

SUBMITTED TO THE GRADUATE FACULTY

in partial fulfillment of the requirements for the

Degree of

MASTER OF SCIENCE IN METEOROLOGY

By

LAURA SHEDD
Norman, Oklahoma
2022

METEOROLOGICAL BENEFITS OF DUAL-POLARIZATION,
RAPID-SCANNING RADAR SYSTEMS ON HAIL PRODUCING STORMS

A THESIS APPROVED FOR THE
SCHOOL OF METEOROLOGY

BY THE COMMITTEE CONSISTING OF

Dr.David Bodine, Chair

Dr.Anthony Reinhart

Dr.Robert Palmer

Dr.Cameron Homeyer

Acknowledgments

First, I would like to thank my advisors, Dr. David Bodine and Dr. Tony Reinhart for their support and mentorship throughout these past 2 years. It is because of their advisement that I was able to successfully complete this project. Their guidance and feedback along the way and their challenges to look at things from a different lens has only served to make me a better scientist. Thank you for helping me navigate the transition to grad school and for the encouragement along the way when things got stressful. I am very much looking forward to continuing to work with both of them in the years to come. I also want to thank Dr. Robert Palmer and Dr. Cameron Homeyer for their willingness and time to serve on my thesis committee. Thank you also to Howie Bluestein and his research group for collecting the RaXPol data and for sharing it so that I could use it for the completion of this project.

I would also like to thank my family for constantly encouraging me to follow my passions and for opening the roads to be able to do so. I would not be here without their love and support especially over these past two years. Thank you for never stopping me to follow my dreams, even if that took me halfway across the country. Thanks also for reminding me to call home sometimes, I promise to try and do that more often. Thanks also to Alec, my constant rock, for constantly being there when I needed it the most. You have helped to make grad school less stressful and have been one of my biggest sources of encouragement in helping me pursue my goals. I would also like to thank my friends, both here and far, for their encouragement and support navigating grad school in the midst of a pandemic. To my research group - Brandon, Rachael, Morgan and Sam - thank you for being an ounce of sanity navigating fundies online and for being a constant source of poorly made figures that we can laugh over together. You all have made coming to the lab something I look forward to each week! To my roommates - Emily and Angela - thanks for being part of my first year covid bubble and for the memories made across the hallway photo wall. To my bible study, thank you for being

my constant support each and every week, especially in the midst of thesis writing, y'all have been a constant source of encouragement and growth. Thanks also to my cat, Radar, for being an excellent research assistant and for the constant demand of playtime and cuddles.

Table of Contents

List Of Tables

List Of Figures

Abstract

Hailstorms continue to be one of the leading economic natural hazards in the United States, amounting to ten billion dollars in damage, on average, annually. Radar technology is one of the best means of detecting hailstorms, especially from an operational standpoint, and the implementation of dual-polarization radars has enhanced this capability. However, most operational radar systems to date have temporal update times that are insufficient for understanding some of the rapidly evolving microphysical and dynamical processes of hailstorms, such as drop shedding, melting of hail or variability of hailfall associated with updraft changes. As such, past studies have heavily relied on models and radar observations with insufficient update times on the order of $5-7$ minutes.

Recent advances in radar technology have paved the way for a better analysis of hailstorms through the implementation of rapid scanning radar systems and innovative approaches to obtain faster scans. This study uses two radars providing rapid-scan observations, the Rapid X-band Polarimetric Radar (RaXPol) and KOUN to examine what rapidly evolving features can be resolved in hailstorms. RaXPol, a mobile X-band radar system, provides full volumetric update times of 24 seconds and with its close proximity to the storm, also provides high spatial resolution, thus allowing for some microphysical processes to be resolved in more detail. While KOUN does not update as quickly as RaXPol, it completes fast sector scans in $90-120$ seconds, providing more detail than a conventional NEXRAD over a storms lifetime. RaXPol data were obtained from the 15 June 2017 supercell near Hays, KS that produced 2.5" hail. Using vertical cross sections, RaXPol is able to capture the rapid growth of the Z_{DR} column as well as a hail fallout signature that becomes stratified into distinct layers. We hypothesize these layers to be associated with 1) large, dry hail, 2) smaller, melting hail, and 3) large drops from melting hail or drop shedding with the stratification resulting from size sorting. Since the hailfall occurs into a precipitation-free region,

this provides a unique view of the temporal evolution of melting hail and size-sorting processes.

KOUN data were obtained from 4 hail-producing storms across 3 days. Similar to RaXPol, KOUN was able to capture vertically evolving features such as the growth and decay of the Z_{DR} column and the three-body scatter spike. Vertical cross sections of Z_H, Z_{DR}, and ρ_{hv} allowed for hail fallout to be resolved, though the extent of the microphysical processes ongoing was more limited, especially when compared to the RaXPol data. Through the use of derived parameters, such as MESH and an HCA, KOUN was able to better capture the full lifecycle of a hailstorm, including the cyclic evolution of hail production and its relation to storm mode. This dataset was also emulated to a NEXRAD update time range to explore what features, such as the evolution of the TBSS, would not be resolved with a rapid-scanning radar system. Understanding the benefits of using a rapid scanning radar system will be advantageous for future phased-array systems and will provide more detail on the processes affecting hail growth and production both from the research realm, as well as detecting hail and other precursor signatures in warning operations.

Chapter 1

Introduction

Hailstorms are one of the leading economic disasters across the United States. On average, losses related to hail exceed $10 billion each year, which is larger than losses related to tornadoes, hurricanes or floods (Gunturi and Tippett 2017; Allen et al. 2020). These estimates do not include losses related to agriculture, so the total average annual loss per year related to hailstorms is higher. Metropolitian areas can routinely exceed $1 billion dollar losses from just a single hailstorm that occurs in the area. Despite the substantial economic loss, however, Allen et al. (2020) argued that that the losses in recent years have been outpacing the research of associated hailstorms, thus necessitating an increased focus in studying this hazard.

Hail is associated with convective storms, with the largest hailstones typically a result of supercell storms. Hail most commonly occurs during the spring months and most commonly across the Great Plains in the United States, though hail can occur at anytime of the year in any location (Allen et al. 2017). Across the Great Plains, hail can exceed a maximum diameter of 4" annually, with a mean diameter of >3" annually (Figure 1.1). In addition, hail occurs globally, typically most often in Europe, Australia, South America and China, though this may be tied to the observing networks available in these locations. In fact some of the largest hailstones have come out of South America in recent years, such as the gargantuan hailstone discussed in Kumjian et al. (2020). As such, studies of hailstorms have been of global interest.
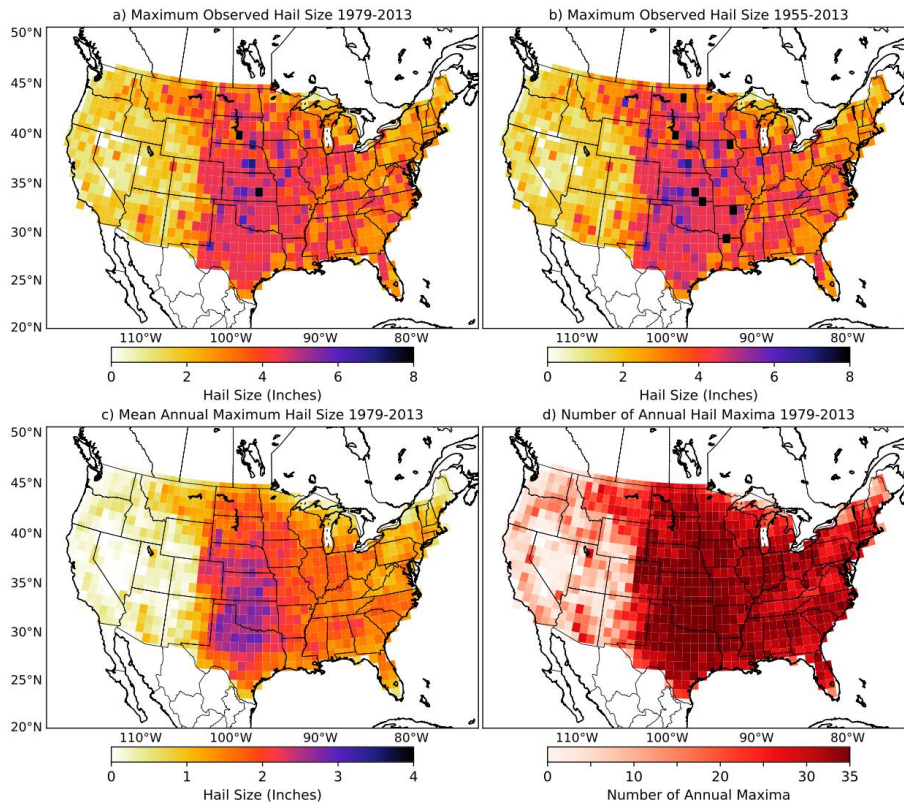
Figure 1.1: Plots of the a–b) maximum and c) mean hail size from the NCEI database and d) the number of annual max from this dataset. Figure taken from Allen et al. (2017).

Hail research began in the 1950s with the Alberta Hail Studies Project, but did not receive substantial field project attention again until the 1970s, which brought both the National Hail Research Experiment and the Joint Hail Research Project (Goyer 1970; Barge et al. 1973). These early projects and associated studies provided initial insight into the growth processes associated with hailstorms. However, after the 1970s and 1980s, substantial progress on hail research became limited until the mid-2000s. The Severe Hazards Analysis and Verification Experiment (SHAVE) was conducted from 2006 – 2015. This project helped to increase verification of hail reports by calling residents in the areas where hail was suspected to have fallen to collect hail reports (Ortega et al. 2009). The hail spatial and temporal observation network

effort (HailSTONE) project sought to increase spatial and temporal observations of hailstorms and through this found that forecasted hail sizes were generally larger than observed hail sizes from convective storms (Blair et al. 2017). Additionally, since 2012 the Insurance Institute for Business and Home Safety (IBHS) has conducted yearly field campaigns focused on collecting size and strength distributions of hailstones across the Great Plains. In 2015, 3D laser scanning began as a part of the IBHS field campaign, which has provided high resolution accurate measurements of hailstones at the surface. This technology has since been used to verify state hailstone records, such as the Hondo, TX hailstone in 2021 (Giammanco et al. 2017; Brown-Giammanco and Giammanco 2018).

Radar technology has continually proven to be one of the best ways to observe and study hailstorms. Recent upgrades to dual-polarization (dual-pol) technology have further aided this capability, as dual-pol parameters can leverage information about the hailstone's physical properties through the use of both horizontal and vertical polarizations. For example, differential reflectivity (Z_{DR}) can give information about the relative apparent shape of a hailstone and differential phase (ϕ_{DP}) can provide information on the wetness of the surface of the hailstone (Kumjian 2013a). This technology has also allowed for derived quantities to be calculated, such as the hydrometeor classification algorithm (HCA). Parameters such as the HCA combined with the maximum expected size of hail (MESH) which takes the vertical profile of Z_H to estimate hail size and hail swaths, can help to improve warning operations for hailstorms (Witt et al. 1998).

Typical NEXRAD systems utilize an update time of 5–7 minutes, on average. While this means that the detection of most severe hailstorms will not be missed, this has its limitations for the microphysical understanding and evolution of hailstorms. For example, Rasmussen et al. (1984) found that hail melt and drop shedding occurs on

the order of seconds, which is going to be on a timescale much shorter than what the current NEXRAD system observes. As a result of this limitation, modeling studies of hail trajectories and associated processes have been heavily favored in recent years (e.g. Kumjian et al. 2014, 2021; Ryzhkov et al. 2013a; Dennis and Kumjian 2017). This has allowed for an increased understanding in hail growth processes through the use of convective allowing models, but little has been done to provide observational confirmation of rapidly evolving features that these models have resolved, such as hail growth, melting and size sorting.

Further upgrades to rapid-scanning dual-pol radar observations have continued to advance our understanding and operations associated with convective hazards. Most of these observations have been applied to tornado research, though some studies such as Kuster et al. (2019) have been used for microphysical processes, such as the evolution of the Z_{DR} column depth. Witt et al. (2018) utilized multiple rapid-scanning radar systems on the 2013 El Reno supercell to look at the storm dynamics that produced hail up to 16 cm in diameter and found that the mid-level rotational velocity using these systems was more than double than what had been thought previously. Operationally, these observations have been shown to be useful as warning times and probability of detection have improved when using the faster update times compared to a NEXRAD update time (Bowden et al. 2015).

Phased-Array Radar (PAR) is a new emerging radar technology that will allow for even higher temporal resolution observations of severe convective storms than what some current rapid-scanning systems provide. Systems such as the National Weather Radar Testbed (NWRT) and the Atmospheric Imaging Radar (AIR) have provided a first look into the benefits of using PAR systems, as update times were on the order of seconds, allowing for fine-scale features to be quickly detected (Heinselman et al. 2008; Isom et al. 2013). For hail, PARs can prove advantageous not only because of the high

4

temporal resolution, but because of the ease in capability to complete deep vertical scans, thus allowing the entire depth of a convective storm to be observed. While these early studies and systems have shown utility, there was only single-polarization capabilities so the evolution of microphysical processes that are best captured using parameters, such as Z_{DR}, remained limited. Upgrades to these systems and newly emerging radars are beginning to provide dual-pol observations, thus allowing for a detailed microphysical view of convective storms on the order of a few tens of seconds or less. However, with a relatively limited amount of work done using rapid-scan dual-pol radars, insight into the meteorological benefits of the dual-pol PARs remains limited.

This study seeks to evaluate the meteorological benefits of using rapid-scanning dual-pol radar systems for hail-producing storms. Specifically, it aims look at the benefits within three areas:

1. Science: What microphysical processes associated with hailstorms can rapid-scanning radar systems observe that have not been able to be observed with conventional NEXRAD systems?

2. Operations: How can rapid-scanning radar systems help to improve our warning operations for hailstorms?

3. Technology: How can we apply these rapid-scan observations to future PAR systems, specifically in designing scanning strategies for research and operational systems?

    (a) How can future PAR technology in turn continue to help warning operations and mitigation strategies for hailstorms?

The rest of this thesis is as follows. Chapter 2 provides a background on hail microphysics, along with dual-polarization radar variables and signatures used to observe hailstorms. Chapter 3 gives the methodology, including a background on the radar systems used for this project. Chapters 4 and 5 provide the results and discussion to this study, which will be split up by operating system. Chapter 6 provides the conclusions and future work, including applications to future PAR technology.

Chapter 2

Background

2.1 Hail Microphysics and Dynamics

2.1.1 Environmental Conditions Supporting Hail Growth

Five environmental conditions are needed in order to get sufficient hail growth. First, ample moisture within the hail growth zone (HGZ) is needed. The HGZ is typically defined as the -10°C to -25°C region within a convective updraft (Knight et al. 1975; Nelson 1983; Foote 1984). This moisture should contain ample supercooled liquid droplets, as the primary growth mechanism for hail is through the riming or accretion of supercooled liquid drops on the surface of the hailstone (Heymsfield 1982; Nelson 1983). In order for riming or accretion to begin, hail embryos are needed, which primarily come from either graupel or frozen droplets. Graupel embryos are common in storms with of cool cloud bases, where the base of the cloud is above the T = 0°C height. Frozen drop embryos are common in storms with warm cloud bases, where the base of the cloud is below the T = 0°C height, which then get swept upward and freeze (Knight and Knight 1970; Knight 1981; Heymsfield 1982).

Ample residence time is needed for sufficient hail growth, where the residence time is defined as the time that a growing hailstone spends within the HGZ. In order to maximize the residence time, the updraft within a convective storm needs to be of sufficient strength and breadth. First, there needs to be a balance between the updraft

speed and the fall speed of the hailstone in order to keep the growing hailstone lofted within the HGZ (Heymsfield 1982; Foote 1984). Additionally, Dennis and Kumjian (2017) found that the width of the updraft plays an important role in maximizing residence time, as a wider updraft kept hailstones within the HGZ longer than their narrower counterparts for an updraft of similar strength. In general, the residence time has been seen to be approximately 10–15 min, but vary depending on the size and growth rates of the hydrometeors as well as the properties of the storm's updraft (Nelson 1983; Dennis and Kumjian 2017).

2.1.2 Hail Growth

Hail typically takes on a singular cyclonic trajectory through a convective updraft, though the path of these trajectories vary widely based on the storm mode and shape (Figure 2.1; Nelson 1983; Dennis and Kumjian 2017; Kumjian et al. 2021). In order to get hail growth to initiate, hail embryos, such as frozen drops or graupel particles, are needed. These embryos are assumed to originate from either feeder cells or were already residing within the primary updraft (Lamb and Verlinde 2011). These embryos begin growing through ice-growth processes such as vapor deposition or riming. With time, embryos from the feeder cells get ejected into the primary updraft and rapid growth initiates. This rapid growth processes require that there is a constant ample balance between the concentration of growing hydrometeors and supercooled droplets (Nelson 1983; Allen et al. 2020). The primary growth mechanism for hail is riming or accretion of the supercooled liquid water droplets onto the surface of the hailstone. Riming results in the immediate freezing of the droplets, whereas accretion causes the droplets to remain a liquid after contacting the hailstone. Vapor deposition can also occur within growing hailstones, but this is less common (Rasmussen et al. 1984).

8
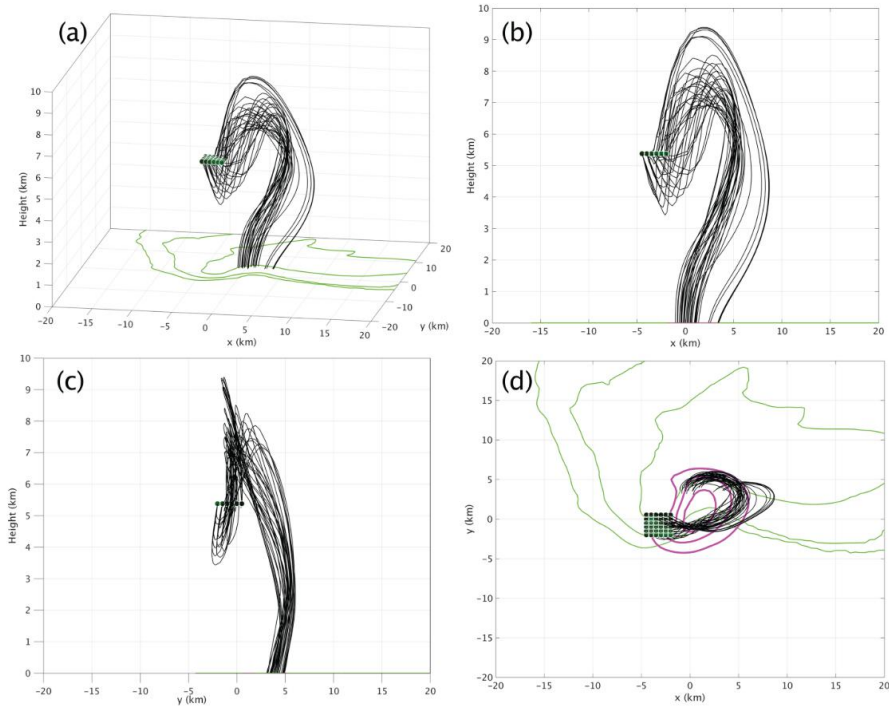
Figure 2.1: Hail trajectories from Dennis and Kumjian (2017).

The growth of hailstones occurs under a thermal energy balance between the cooling rates due to freezing and the warming rates due to thermal conduction, sublimation and the warming of accreted water on the surface of the hailstone (Lamb and Verlinde 2011). Mathematically this is given by

$$l_f(\frac{\pi}{4}D_H^2 v_H E_{coll}\omega_L) = 2\pi D_H k_{T,air} f_T(T_{sfc} - T_\infty)$$

$$+ 2\pi D_H f_v D_v(\rho_{v,\infty} - \rho_{v,sfc})l_s + K\omega_L c_L(T_{sfc} - T\infty) \quad (2.1)$$

where l_f is the latent heat of freezing, D_H is the hailstone diameter, v_H is the hailstones velocity, E_{coll} is the collision efficiency and ω_l is the liquid water content, with the first term representing the freezing of accreted water. The second term represents the rate of thermal conduction where $k_{t,air}$ is the thermal conductivity of air, f_T is the thermal

energy ventilation coefficient, and T_{sfc} and T_0 are the temperature of the air and hailstone, respectively. The third term, or the sublimation term, is given by f_v the vapor transport ventilation coefficient, D_v the diameter of the vapor particle, $\rho_{v,\infty}$ and $\rho_{v,sfc}$, the density of the air and hailstone respectively. The last term represents the warming of accreted water and is represented by K, the collection kernel, ω_L, the crtical water vapor content, and c_L, the specific heat capacity of liquid.

There are two primary growth regimes that hailstones can undergo: wet growth and dry growth. The thermal energy balance in Equation (2.1) can be used to determine the growth regime that a hailstone is undergoing given its ambient environmental conditions and surface properties of the hailstone. A rearrangement of Equation (2.1) gives the "Schumann-Ludlam" limit, which is typically used to delineate between the growth regimes and is given by

$$\omega_L = \frac{2\pi D_H[f_T k_{T,air}(T_o - T_\infty) + f_v D_v(\rho_{v,sfc} - \rho_{v,\infty})l_s]}{K[l_f - c_L(T_o - T_\infty)]} \tag{2.2}$$

where ω_L is the supercooled critical liquid water content (LWC) needed for wet growth to occur, which is based on the environmental conditions surrounding a growing hailstone (Schumann 1938; Ludlam 1958). If the terms on the right hand side of Equation (2.2) exceeds the threshold ω_L, then wet growth is expected to occur on the surface of the hailstone and if the right hand side is less than ω_L, dry growth is expected to occur. In more simplified terms, for a given hailstone diameter, wet growth is the favored regime when the environmental temperature and concentration of supercooled liquid water is high.

During dry growth, the surface of the growing hailstone is frozen. This results in supercooled liquid water droplets to freeze upon contact with surface of the hailstone. In order to maintain the thermal energy balance given in Equation (2.1), this means

that the surface of the hailstone warms (Rasmussen and Heymsfield 1987; Lamb and Verlinde 2011). If the surface of the hailstone sufficiently warms to be at or exceed T = 0°C, the collected supercooled liquid drops won't freeze upon contact and the surface of the hailstone becomes a liquid. Continued collection of droplets then means that the hailstone is undergoing wet growth conditions. Growing hailstones can oscillate between growth regimes during its lifecycle, though it is thought that large hailstones especially most often end in the wet growth regime (Knight and Knight 1970).

2.1.3   Hail Descent and Melting

As a hailstone grows, the fall speed of the hailstone increases. The terminal velocity that a hailstone acquires is strongly dependent upon the physical characteristics of the hailstone, as this impacts the drag coefficient of the hailstone. Allen et al. (2020) noted that using a power-law relationship gave a terminal velocity to maximum diameter relationship of

$$v_t = 12.43 D^{0.4792} \tag{2.3}$$

though other studies such as Heymsfield and Wright (2014) have found alternative relationships. These variations may be due to a lack of consensus on the fall patterns of hailstones as well as the fact that there is not a direct relationship between the drag coefficient and the maximum dimension (Shedd et al. 2021).

As the hailstone grows, its fall speed eventually surpasses the updraft speed or the hailstone gets advected out of the updraft and it begins to descend. When hail falls below the T = 0°C level, melting can occur. Rasmussen et al. (1984) and Rasmussen and Heymsfield (1987) did much of the foundational work on the melting processes associated with ice and hail. As hail melts, water accumulates across the surface of the

Transitions during melting; melting proceeds left to right.

	A	B	C	D	E
	Dry Hailstone	Just Wet	Soaking of Water	Just Soaked	Equilibrium Mass of Water on Surface (shedding of water occurs to maintain equilibrium as ice core gets smaller).
High Density Hailstone	◯	◯	N/A	N/A	(droplet with upward arrows)
Low Density Hailstone	(hatched)	(hatched)	(cross-hatched)	(cross-hatched)	(droplet with upward arrows)

Legend:
- High Density Ice ($\rho_i = 0.91$ g cm^{-3})
- Low Density Ice ($\rho_i < 0.91$ g cm^{-3})
- Low Density Ice Soaked with Water
- Water

Figure 2.2: The hail melting process outlined in Rasmussen and Heymsfield (1987).

hailstone and small drops can be shed off of its surface. Since the hailstone is descending, the upward drag force causes the liquid surface to accumulate towards the center of the hailstone. With time, this causes a torus of water to develop along the center of the major axis, which stabilizes the orientation of the hailstone. Water continues to grow this torus and eventually it becomes unstable, resulting in instantaneous shedding of the drops (Figure 2.2). This process continues until the hailstone reaches the surface or until most of the hailstone becomes melted, as which point a water droplet with a ice core develops and continues melting the ice. Thus, with large melting rates, only the largest hailstones will reach the surface, though typically they will be smaller than they were aloft.

2.1.4 Physical Properties of Hail

Hail at the surface takes on a variety of physical appearances, which is dependent upon the growth and melting processes it underwent (Figure 2.3). Hailstones with a maximum diameter <6 cm are most common, though hail can exceed a maximum diameter of 15 cm. In general, hailstones are not spherical, but rather are considered to be oblate spheroids (Knight 1986; Allen et al. 2020; Shedd et al. 2021). Smaller hailstones may retain some spherical nature, but larger hailstones progressively return lower sphericity values. This is partly due to more vigorous wet growth, which can lead to an increased number of irregularites on its surface as well as how the fall properties of the hailstone, which is not presently fully understood.

The growth regime that a hailstone undergoes is strongly tied to the physical appearance of the ice throughout the hydrometeor. During dry growth, ice instantaneously freezing on the surface of the hailstone results in air bubbles to develop and then get trapped as the hailstone continues to grow. This lowers the density of the hailstone and causes the ice to appear opaque (Knight and Knight 2005; Allen et al. 2020). During wet growth, the surface of the hailstone is a liquid, so supercooled particles do not freeze upon contact with the surface. In this case, the liquid surface is able to seep into the cracks that may have developed. This results in an increase of the density of the hailstone and will result in clear ice in appearance (Rasmussen and Heymsfield 1987). As a hailstone grows, these two growth regimes can alternate based on the ambient environment it's in, resulting in alternating layers of opaque and clear ice.

Cusps and lobes can develop on the surface of hailstones, giving irregular and non-spherical shapes, such as those in Figure 2.3. Lobes develop almost exclusively in wet growth, as they are commonly observed to be entirely clear ice (Knight and Knight
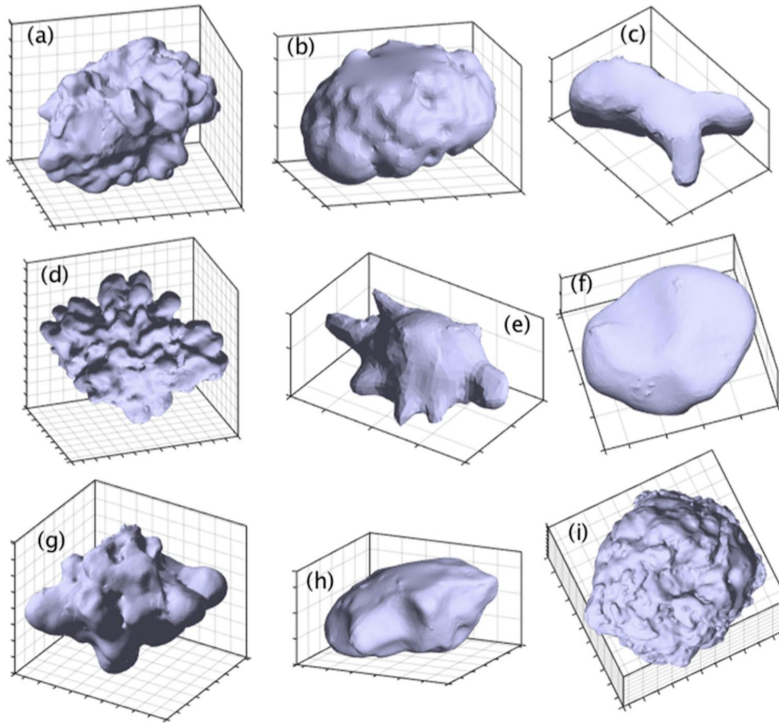
Figure 2.3: Examples of some 3D scanned hailstones, taken from Shedd et al. (2021) their Figure 3.

1970a). They develop through water being pushed across the surface of the hailstone, which then freezes and cause a bump or icicle appearance extending outward from the hailstone. For especially vigorous wet growth, these lobes can extend substantial distances from the primary surface. The development of these lobes can shield other portions of the hailstones surface, which can result in craters, or cusps on the hailstone (Knight and Knight 1970a, 2005). As is the case for the alternating growth regimes, a single hailstone can feature both cusps and lobes on its surface.

2.1.5 Hailstorm Forecasting

In the United States, hail most commonly occurs to the east of the Rocky Mountains during the warm season, which is tied strongly to the environmental conditions that are most favorable for convective activity during this time (Figure 1.1; Allen et al. 2017).

14

Forecasting hail occurrence, and most importantly hail size, however, continues to be a challenge due to the complex nature of hail microphysics and storm mode (Allen et al. 2020). However, some forecasting parameters can be utilized to garner information on where the potential for a hailstorm may occur, and in some cases where the potential for significantly severe hailstones may be. In hail forecasting, severe hail is considered to be hailstones with a $D_{max} >1$" and significant severe hail is hail with a $D_{max} >2$". Hailstones with a $D_{max} >6$" have recently been termed to be gargantuan hail (Kumjian et al. 2020). Forecasters will also reference hailstones in terms of physical objects, such as those given in Table 2.1.

Convective parameters are most commonly assessed in forecasting the occurrence of hail, assuming that the model is initiating storms. The most important forecasting parameters are related to the properties of the updraft, in particular the strength and width of it. Convective available potential energy, or CAPE, can give a proxy to updraft strength and the magnitude of the 0–6 km vertical wind shear or the 0-3 km storm relative helicity (SRH) can give an indication to the width of the updraft (Brooks et al. 2003; Johnson and Sugden 2014; Dennis and Kumjian 2017; Kumjian et al. 2019). The depth of the HGZ is also used, as this can give a further indication of the potential for an updraft sufficient for substantial hail growth (Allen et al. 2015). Many of these individual parameters have shown limited skill in forecasting hail size, but have proven useful in forecasting the occurrence of hail across a given region.

Forecasters also utilize composite parameters in order to predict hail occurrence. The Significant Hail Parameter (SHIP) is commonly used to distinguish between the potential for significant and non-significant hail environments and is a combination of the most-unstable CAPE (MUCAPE), the mixing ratio of a most unstable air parcel, the 700–500mb lapse rate, the 500mb temperature, and the 0–6km vertical wind shear.

Table 2.1: Commonly used objects associated with a given hailstone maximum dimension

D_{max}	Object
0.25"	Pea
0.5"	Marble
0.75"	Penny
1"	Quarter
1.25"	Half Dollar
1.5"	Ping-Pong Ball
1.75"	Golf Ball
2"	Hen Egg
2.5"	Tennis Ball
2.75"	Baseball
3"	Tea Cup
4"	Softball
4.5"	Grapefruit
5"	DVD
6"	Honeydew Melon

SHIP values >1 are indicative of the potential for significant severe hail, but does not give an actual forecasted hail size. Similarly, the Large Hail Parameter (LHP) is used to distinguish between environments capable of significant severe hail, though the parameters are different than what is used in SHIP. The LHP utilizes a combination of MUCAPE, 700–500mb lapse rates, the depth of the HGZ, and 3 components related to vertical wind shear, under the assumption that the shear and MUCAPE are capable of producing supercells (Johnson and Sugden 2014).

2.2 Radar Observations of Hail

2.2.1 Dual-Pol Variables

Radar returns can give indications of active hailfall occurring both aloft and at the surface. The advent of dual-pol has both improved detection capabilities and has also provided some insight into the apparent physical properties of the hydrometeors, based on the range of values associated with the magnitude of the returns. The most commonly used dual-pol variables for hail include reflectivity (Z_H), differential reflectivity (Z_{DR}), cross-correlation coefficient (ρ_{hv}) and specific differential phase (K_{DP}), all of which vary across scattering volumes, as indicated in Figure 2.4.

Radar reflectivity factor gives a measure of the range-corrected returned power a radar receives across a single polarization, which can provide information on the concentration and size of the hydrometeors within the scattering volume. For Rayleigh scattering, it is calculated by

$$Z_H = \int_0^\infty N(D)D^6 \, dD \tag{2.4}$$

Reflectivity is often viewed on a logarithmic scale, with a typical range of values from -10 to >80 dBZ. For hail, reflectivity values are typically >40 dBZ. Larger values of reflectivity are commonly assumed to be associated with larger hailstones, but it is also possible that the highest reflectivity values are actually associated with higher concentrations of smaller sized hailstones (Blair et al. 2011; Kumjian 2013b). Reflectivity alone has proven to generally be a poor indicator of hail size. This is in large part because hailstones with a D_{max} exceeding the wavelength of the radar enters into the Mie regime, which results in more forward scattering by the hydrometeor, compared to uniform scattering for hydrometeors within the Rayleigh regime (Rauber and Nesbitt
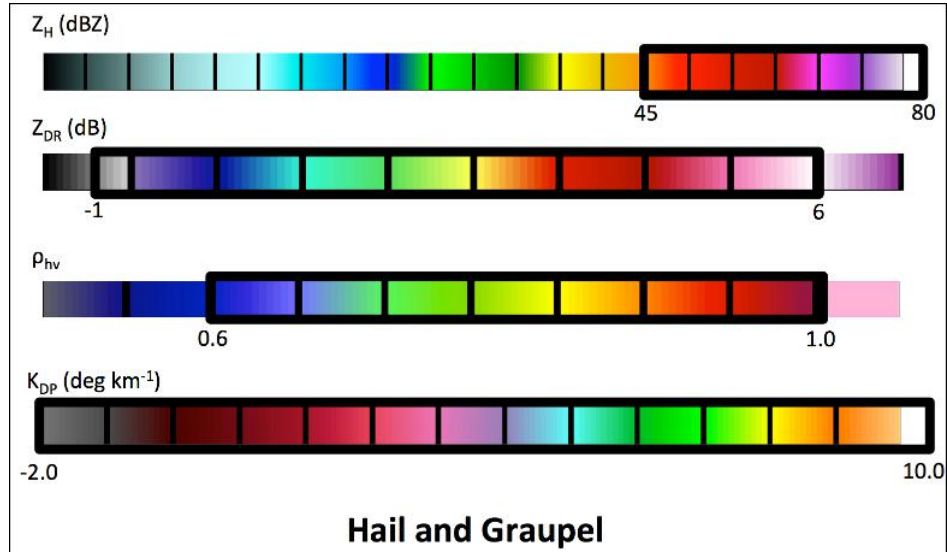
Figure 2.4: Expected radar return values of Z_H, Z_{DR}, ρ_{hv}, and K_{DP} for hail and graupel hydrometeors. Taken from Kumjian (2013a), their Figure A2.

2018). This results in ambiguous Z_H measurements, thus limiting utility in estimating hail size.

Differential reflectivity (Z_{DR}) provides a measure of the ratio between the horizontal and vertical polarization returns. Z_{DR} is calculated by

$$Z_{DR} = 10 \log_{10} \left(\frac{Z_H}{Z_V} \right) \tag{2.5}$$

where Z_V is the vertical polarization radar reflectivity factor. For hail, Z_{DR} provides information on the relative shape and size of the hydrometeors in the scattering volume. Z_{DR} values near 0 dB are generally assumed to be either small hailstones or hail that is randomly tumbling as the tumbling can cause the relative Z_H and Z_V to be nearly identical (Bringi et al. 1984; Kumjian 2013a). As hail becomes larger, it typically becomes more oblate, which means that the backscattering in the horizontal will progressively become larger than the backscattering in the vertical. This will result in progressively larger positive values of Z_{DR} with increasing hail size, assuming that the

hail D_{max} remains within the Rayleigh regime. If the size of the hydrometeors exceed the wavelength of the radar, the hydrometeor enters into the Mie scattering regime. This can then result in negative Z_{DR} returns (Kumjian et al. 2010; Picca and Ryzhkov 2012). Thus, the general assumption is that a region of negative Z_{DR} is associated with large hailstones. In addition, as melting hailstones develop a torus of water around the central axis, they appear more oblate in nature (Rasmussen and Heymsfield 1987). This results in an enhancement in the Z_{DR} returns, in some cases exceeding 3–4 dB (Kumjian 2013a; Ryzhkov et al. 2013b). Melting is less for large hailstones compared to their smaller counterparts, which can result in their Z_{DR} to be near 0 dB as it descends towards the surface (Ortega et al. 2016).

Cross correlation coefficient (ρ_{hv}) provides a measure of how similar the horiztonal and vertical backscattered signals are within a radar volume. This can provide information on how similar the hydrometeors are within a scattering volume. ρ_{hv} is calculated by

$$\rho_{hv} = \frac{< |S_{VV}S_{HH}^*| >}{\sqrt{|S_{HH}|^2 |S_{VV}|^2}} \tag{2.6}$$

where S_{HH} and S_{VV} are the horizontal and vertical scattering amplitudes, respectively. Values of ρ_{hv} range from 0 to 1, where increasing values indicate more similarity of the hydrometeors within the radar volume. Hail typically has ρ_{hv} returns between 0.6 and 1 (Figure 2.4). In contrast, ρ_{hv} for pure rain is near 1, making ρ_{hv} useful for hail detection as a region of locally lower ρ_{hv} returns. Differences in ρ_{hv} can be due to differences in the growth regime of hail, as dry hailstones will typically have higher ρ_{hv} values than wet hailstones. In addition, differences in ρ_{hv} can result from differences in hail size, as more irregularly shaped larger hailstones have been shown to reduce the magntiude of ρ_{hv} (Picca and Ryzhkov 2012; Kumjian et al. 2010; Kumjian 2013a,b).

2.2.2 Polarimetric Radar Signatures

The advent of dual-pol has brought forth numerous polarimetric radar signatures that can be indicative of ongoing or upcoming surface hailfall (Figure 2.5). One such signature is the Z_{DR} column, which is a vertical column of positive Z_{DR} returns that extends past the environmental T = 0°C level in close proximity to the updraft of a thunderstorm (Conway and Zrnic 1993). Typically the Z_{DR} column is slightly offset from the highest Z_H returns, especially near the surface (Kumjian and Ryzhkov 2008). The Z_{DR} column arises from large drops, which have a positive Z_{DR} return due to their oblateness, being lofted into the updraft. The development of the Z_{DR} column has been shown to be a potential pre-cursor signature to surface hailfall as it has been seen as a proxy for an intensifying updraft. Kumjian et al. (2014) found that the Z_{DR} column development can indicate that hail will reach the surface in roughly 10–15 min as it was found to precede an increase in Z_H near the surface as well (Picca and Ryzhkov 2012).

Other proxies for the updraft are the bounded weak echo region, or BWER and the appearance of Z_{DR} or ρ_{hv} rings in the mid-levels. The BWER is spatially offset from the Z_{DR} column and marks the location of the updraft within a convective storm. BWERs on radar appear as a column of a locally low Z_H returns, surrounded by high Z_H. It forms as a result of a strong updraft that advects newly formed hydrometeors aloft, but these hydrometors are small enough that their Z_H returns are low (Lakshmanan and Witt 1997; Kumjian and Ryzhkov 2008). The Z_{DR} or ρ_{hv} rings are areas of positive Z_{DR} or reduced ρ_{hv}, respectively that wrap around the location of the mesocyclone at the mid-levels (see Figure 2.5). They are associated with mixed-phase hydrometeors and in some cases, non-Rayleigh scatterers, which is assumed to be large hydrometeors (Kumjian and Ryzhkov 2008; Snyder et al. 2013; Kumjian 2013b).
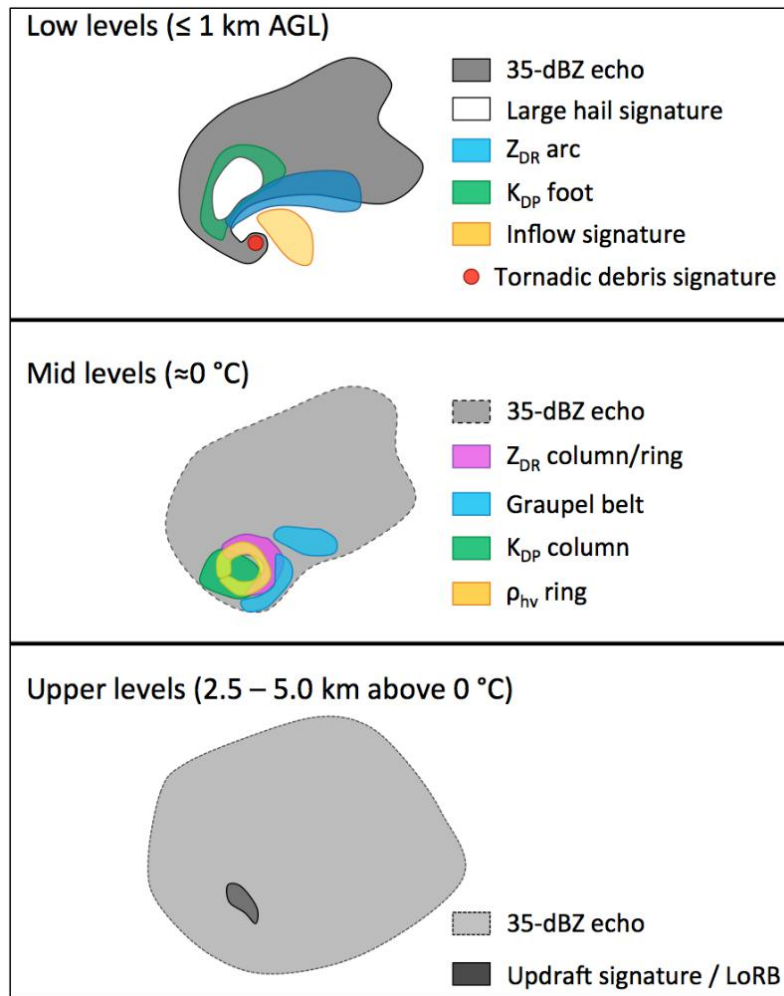
Figure 2.5: Commonly observed polarimetric signatures in supercells, taken from Kumjian (2013b).

Near the surface, the Z_{DR} arc is a common feature associated with supercells. It is an arc of positive Z_{DR}, usually >3 dB, returns located along Z_H gradient in the forward flank of a supercell. The Z_{DR} arc is assumed to arise from size sorting of hydrometeors, where the larger drops are embedded within the Z_{DR} arc as they do not get advected as far as smaller, lighter drops (Kumjian and Ryzhkov 2008). Recent studies such as Dawson et al. (2014) have found the size sorting of hail specifically serves as a strong contributor to the structure and appearance of the Z_{DR} arc. It is also thought that

the Z_{DR} arc could give a precursor signal to tornadogenesis or the strengthening of the mesocyclone, though further investigation of this is still needed. In addition, the demise of the Z_{DR} arc is thought to cause a disruption to the mesocyclone and may indicate large hailfall occurring at the surface (Tanamachi and Heinselman 2016).

The three-body scatter spike (TBSS) is a radar artifact that is commonly associated with the potential for large hail occuring at that elevation angle (Figure 2.6). They can be found both near the surface or aloft, or can expand across some vertical depth of the storm. The TBSS appears as a spike of lower backscattering returns extending downradial from a hail core or a region of heavy precipitation. It forms as the result of hydrometeors sidescattering the transmitted radar beam towards the ground, which travels back up to the hydrometeors and then are backscattered to the radar system (Zrnić 1987; Kumjian 2013c). This implies that the transmitted energy takes longer to return back to the radar than if it just hit the hail, which makes the TBSS appear downradial. The lower Z_H returns within the TBSS are due to radiation being scattered in multiple directions, which lowers its return power. While the TBSS characteristics have yet to provide a direct relationship to hail size, it is a common feature associated with hail-producing storms (Lemon 1998; Zrnic et al. 2010). In a similar manner, the sidelobe spike is commonly assumed to be associated with large hail cores. Presently, more work is needed for both of these signatures to understand its association with hail properties and sizing.

2.2.3   Derived Quantities

Dual-pol capabilities have allowed for algorithms related to microphysics to be developed, which can aid in the nowcasting and research associated with convective studies. A hydrometeor classification algorithm (HCA) takes the polarimetric variables
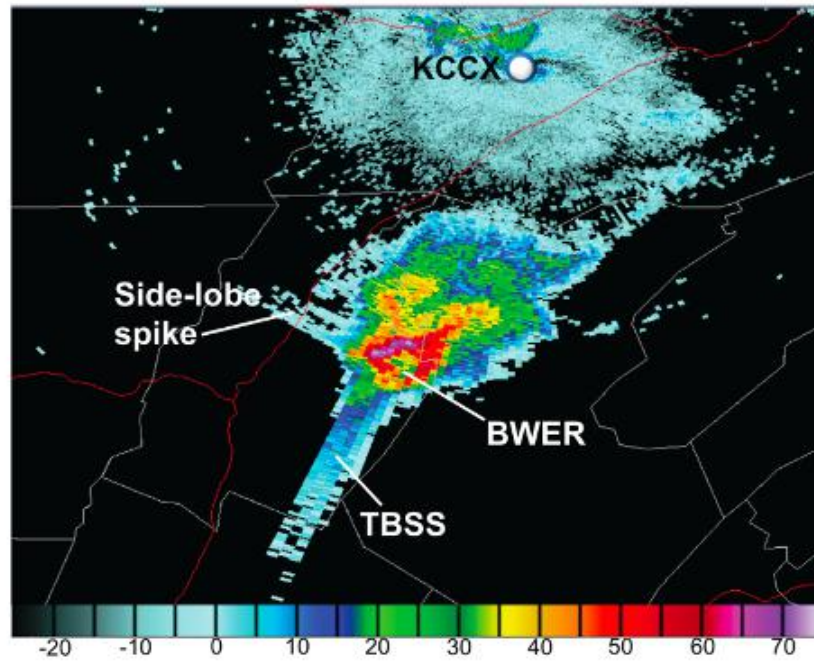
Figure 2.6: Radar imagery of a TBSS and a sidelobe spike observed by the KCCX radar in State College, PA on 30 April 2017. Taken from Allen et al. (2020).

at a given range bin along with information on the environmental temperature and outputs a best guess at the dominant scattering type within that range bin (Straka and Zrnić 1993; Kumjian 2013b). The dominant assumption is that each hydrometeor type has a specified range of returns for each polarimetric variable. Membership functions take the polarimetric returns within an elevation angle and gives the chance that a certain hydrometor type is associated with that variables return, ranging from 0 to 1. In the HCA used by the present NEXRAD system, the membership functions are assumed to be trapezoidal and follows the fuctions outlined in Park et al. (2009). Presently, the HCA is thought to perform well for warm-season applications, such as hailstorms, but still has some performance issues associated with cold-season applications.

Radar echo tops provide a measure of the maximum elevation that a specified reflectivity threshold is detected within a sampling volume. Echo tops are commonly

used to assess storm severity and changes within the echo tops can be used to indicate a potentially intensifying storm (Smith et al. 2016). Studies such as Blair et al. (2011) found that utilizing these echo tops showed potential in distinguishing between large and giant hail cases, as giant hail typically had higher echo top heights. Calculations of echo tops have varied, but recent studies such as Lakshmanan et al. (2013) have used a linear interpolation method to estimate echo top heights in order to limit calculation errors and bias.

The maximum expected size of hail, or MESH, is a quantity that estimates the size of hail within the scattering volume. MESH is derived through the severe hail index, which is based upon the vertically integrated Z_H. It was first developed by Witt et al. (1998) with an operational emphasis to aid in improving warning time for hailstorms. MESH is the forecasted maximum hail size and so it inherently overpredicts the actual observed hail size. Other MESH algorithms have since been developed and have shown similar skill as the one developed by Witt et al. (1998) (Lakshmanan et al. 2007; Smith et al. 2016; Murillo and Homeyer 2019). MESH has been used both in forecasting and climatological applications as its use of only convective echoes gives it a high skill score in identifying and estimating hail size based on radar data.

Chapter 3

Data & Methods

3.1 Rapid-Scanning Radar Systems

This study utilized two rapid scanning radar systems: the Rapid X-Band Polari-metric Radar (RaXPol) and the KOUN WSR-88D research radar (Table 3.1; Snyder et al. 2020). RaXPol is a mobile, X-band radar system at the Advanced Radar Research Center at the University of Oklahoma (Figure 3.1; Pazmany et al. 2013). It has dual-pol capabilities, so it is able to capture the microphysical processes associated with severe, convective storms. Additionally, since its a mobile system, it is able to get within close proximity to severe storms, in some cases <10km, allowing for a better view into the low-levels of a storm. Since RaXPol is an X-band system, it can be heavily affected by attenuation, especially in the presense of large hydrometeors, such as large hail. However, the angular resolution is high with close-range observations, allowing for smaller scale features to be resolved when compared to WSR-88Ds that typically provide longer range observations. Additionally, the pedestal is able to rotate at a rate of 180° per second, meaning it can complete one full rotation in 2 seconds. This can result in a volume coverage pattern that covers 20° in elevation in <1 min, which allows for rapidly evolving features to be observed through a vertical column.

Figure 3.1: Image of the Rapid X-Band Polarimetric Radar (RaXPol) at the University of Oklahoma

This capability is largely due to a process called frequency hopping, in which the frequency of the pulses are shifted each time in order to ensure independent samples when operating in rapid-scan mode.

KOUN is the National Severe Storms Laboratory (NSSL) WSR-88D radar, similar to the present NEXRAD system. It it located a Max Westhemier Airport in Norman, OK and is most often used for hazardous and severe weather observations (Figure 3.2). Similar to RaXPol, KOUN has dual-pol capabilities so microphysical processes are able to be resolved. KOUN is an S-band radar so its longer wavelength means it is less affected by attenuation when compared to RaXPol. Since the two systems have nearly identical beamwidths, the difference in range will dictate a direct relationship to the difference in the angular resolution. Thus, the higher observable range of KOUN means that its angular resolution will also be lower. This higher observing range is partly due to the longer wavelength and higher power of KOUN, which means that KOUN is able to observe more storms at once, including storms that are farther away. This means that it can also capture the full vertical depth of a storm. However, KOUNs fixed position means it cannot always observe within close proximity to a storm. KOUN is

Figure 3.2: Image of KOUN, located in Norman, OK. Photo from Charles Kuster.

also unable to rotate as fast as RaXPol, but it is able to get full volumetric update times in as little as 90 seconds, which is faster than the present WSR-88Ds. This is the result of KOUN being able to operate in a rapid sector scanning mode, which means that it only scans a portion of the 360° plane of view. As an example, KOUN is able to scan an 80° plane of view, which can give full volumetric update times of <2 min (Kumjian et al. 2010; Kuster et al. 2019). This does mean that some storms are missed if they are not within the operating sector, but it still allows for rapidly evolving features across the depth of the storm to be observed.

For purposes of this study, a case study using RaXPol and a composite analysis with KOUN was performed. Data from RaXPol came from 15 June 2017 near Hays, KS, where a long-lived supercell produced 2" hail during the observation period. This case was also selected due to the long duration of observations of the storm, which exceeded one hour, allowing for the full evolution of the hail growth and descent processes to be captured. Data from KOUN came from three days: 19 May 2013, 9 May 2016 and 26

Table 3.1: Comparisons of the specifications of RaXPol and KOUN.

Parameter	RaXPol	KOUN
Wavelength	3.1 cm	10.3 cm
Max Rotation Rate	180° s⁻¹	30° s⁻¹
Average Update Time	24 s	90 s
Beamwidth	1°	1°
Range Resolution	75 m	250 m

March 2017, outlined in Table 3.2. These days were chosen as all featured numerous hail-producing storms across a variety of storm modes, allowing for an investigation into rapidly-evolving features in hailstorms to be performed. KOUN data were analyzed individually in a similar manner to the RaXPol case study and were then investigated together to look for similarities and to investigate the benefits of the rapid update times using a fixed S-band system.

Table 3.2: Summary of the cases selected for study using KOUN, including their observed time by KOUN and evolution of the storm modes.

Day	Storm	Observed Time (UTC)	Storm Mode
19 May 2013	Edmond-Carney, OK	2030 – 2121	Non-Tornadic
		2121 – 2234	EF-1 Tornadic
		2241 – 2324	EF-3 Tornadic
9 May 2016	Katie, OK	2003 – 2106	Non-Tornadic
		2106 – 2127	EF-4 Tornadic
		2138 – 2217	EF-3 Tornadic
26 March 2017	Seminole, OK	2100 – 0044	Non-Tornadic
26 March 2017	Wynnewood, OK	2125 – 0018	Non-Tornadic
		0018 – 0028	EF-0 Tornadic

3.2 Methodology

For both the RaXPol and KOUN data, initial visualization was done using plan position indicator (PPI) plots. RaXPol data were plotted using MATLAB, whereas KOUN data were initially plotted using the NSSL Warning Decision Support System - Integrated Information (WDSS-II) software (Lakshmanan et al. 2007; Smith et al. 2016). Where the PPIs gave a feature of interest across multiple elevation angles, such as a potential Z_{DR} column, a range-height indicator (RHI) plot was created. For both datasets, these RHIs are considered to reconstructed RHIs, in which the PPI data along a given azimuth were stacked together and are characterized by a larger time offset between elevations compared to a true RHI scan. The data were converted into a gridded format and it was assumed that the range gate spacing was uniform throughout, thus allowing for the each elevation angle at a given gate to be stacked on top of one another. Vertical heights were provided in the dataset and so those were included within the gridding process preserve the observable heights of the radar signatures. In the case of the RaXPol data, RHIs were created along a given azimuth at increments of every degree. For KOUN, RHIs in the same manner as RaXPol were not created, but rather cross sections along a user specified distance were created. This was largely due to the utility of WDSSI-II, though cross sections were also able to be created through a Python script where the user specified the location of the cross section on a PPI at a given elevation angle.

Since PPIs of KOUN data were in 80° sectors with a maximum range of 150km, multiple storms could be present in the same sector. This required individual storms data to need to be isolated in order to properly observe dual-pol signatures and trends within a given storm. To isolate the storms, the Lasso Selector tool embedded within the Python matplotlib package was used. Data were first plotted as a PPI at a given

elevation angle using PyArt (Helmus and Collis 2016). The Lasso Selector tool was then implemented in which the lasso was drawn by the user around the perimeter of the storms, beginning where Z_H typically exceeded 20 dBZ, with particular emphasis on making sure to capture the convective core and to not overlap onto another storm. Data and the PPIs were then saved with an identifying name specified by the user and the process was repeated over all elevation angles, as the shape of a given storm was not consistent over elevation angles. An example of a lassoed PPI across two elevation angles is given in Figures 3.3 and 3.4.

Since KOUN data were able to be implemented into WDSS-II and in order to explore the utility of rapidly evolving features using MRMS data, some derived quantities were calculated (Eilts and Coauthors 1996; Lakshmanan et al. 2007; Smith et al. 2016). First, an HCA following the membership functions outlined in Park et al. (2009) was calculated. This HCA did not include the TDS classification, so careful attention was given during analysis for storms that were tornadic and especially those that were strongly tornadic as debris can impact the radar returns. The HCA was used predominately in identifying areas where there may have been hail and/or graupel at the mid-levels. In many instances, it was used to then extract the dual-pol variables of the hail core itself, in order to investigate the evolution of the hail core across all elevation angles, such as descending Z_H cores. The HCA was also used to approximate the area of the hail core at a given elevation angle by calculating the area of each gate bin and then summing together the bins that were classified as hail.

WDSS-II was used to calculate the 50 and 60 dBZ echo tops for each storm at each time step (Lakshmanan et al. 2013). These echo tops were used primarily to investigate any relationships to changes within the relative depth of the storm to the evolution of the hail production. The 50 and 60 dBZ thresholds were thus chosen as studies like
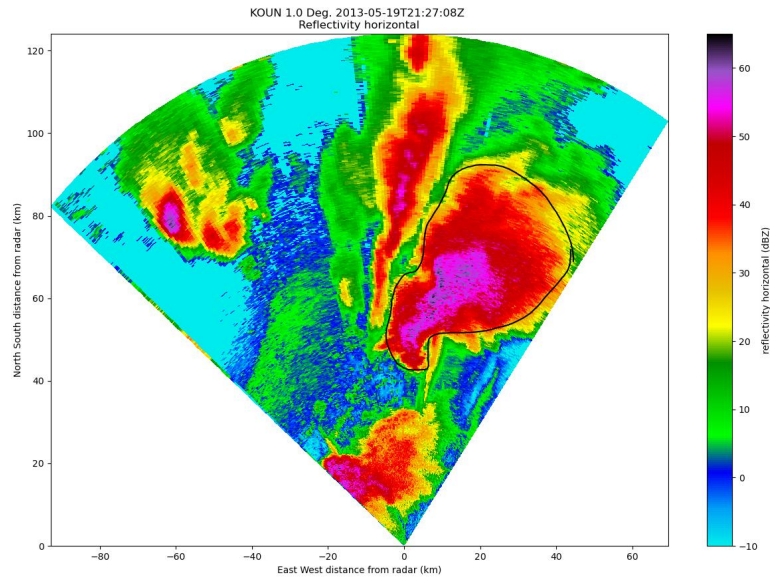
Figure 3.3: Example of the Lasso Selector Tool used to isolate individual storm data from KOUN at the 0.97° elevation on 19 May 2013. The black line indicates the lasso that was drawn around the respective storm for analysis.

Kumjian (2013a) have shown that these can be returns indicative of hail in an S-band system and two thresholds were chosen for comparisons in the potential usability.

MESH was also calculated across all KOUN datasets using the MRMS calculations (Witt et al. 1998). It was used first for identifying the time of peak hailfall within a storm. The 95th percentile of MESH at each time step was calculated and was then used to identify this peak hail time across the duration of the storm. This percentile was used in order to eliminate any possible outliers in the calculations or dataset. Once this peak hail time was identified, PPIs and RHIs from roughly 15–20 min preceding were analyzed, with particular emphasis on rapidly evolving features within this time frame. It was also used to detect when the possibility of descending hail cores could occur around or after this 15–20 min time frame. This analysis time frame was selected as it is the average time that hail takes to grow and fall out of a storm. MESH was
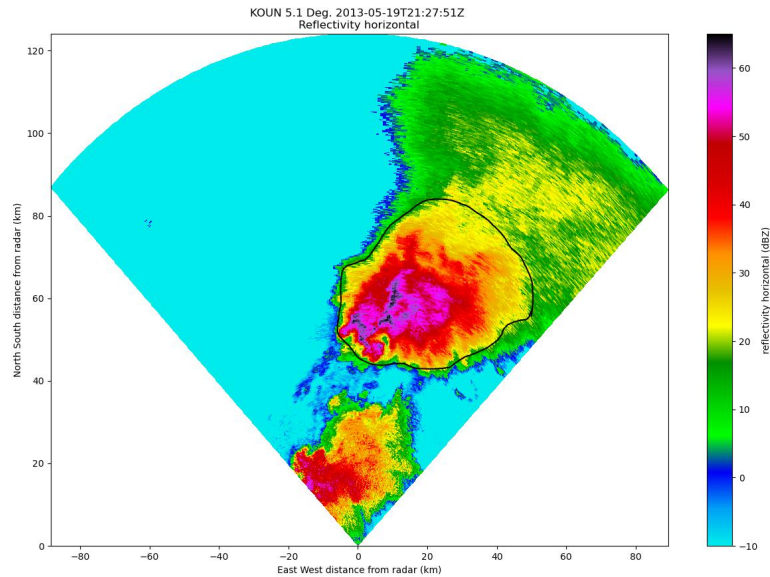
Figure 3.4: Same as Figure 3.3, but for the 5.1° elevation angle.

also utilized to investigate the overall evolution of hail within the storm as many of the selected storms spanned hours. These were also cross compared to investigate the potential impact of storm mode on the evolution of hail production and sizing.

KOUN data were also down-sampled in order to compare how the rapid-scan observations would evolve if they were updating on the conventional NEXRAD time of 5–7 min. This down-sampling process was done in two ways. First, the lassoed datasets were down-sampled to an average update time of roughly six minutes as many of the update times were roughly 90 seconds. This was done by starting at the beginning of a storm's dataset and extracting every 4$^{\text{th}}$ time step based on the update timing, in order to make it close to a 5–6 min update time. In this way, an investigation on the time series on parameters such as MESH were able to be conducted to see the impacts of the rapid-update observations. Rapid-scan data were also compared to native 5 – 6 min volume scans from KTLX, located in Norman, OK. KTLX was selected as this is a operational NEXRAD radar and was located the closest to KOUN. The update

times from KTLX were identified and the PPIs and RHIs were compared to see what observations may be lost if the dataset were updating the same as KTLX. An analysis of both these methods of downsampling will be presented together in Chapter 5.

Chapter 4

Rapid-Scan X-Band Observations of Hailstorms

4.1 Storm Background

On 15 June 2017, a surface low pressure center over Kansas brought forth the potential for severe storms. The Storm Prediction Center (SPC) issued an enhanced (3/5) risk for severe thunderstorms across central and southern Kansas at 1200 UTC, which was upgraded to a moderate risk (4/5) for portions of central Kansas by 1630 UTC (Figure 4.1). Hays, KS, which is the location of interest for this study, was under a slight risk (2/5), as this was near the expected convection initiation (CI). A severe thunderstorm watch was issued across much of the state at 1830 UTC, with the potential for hail up to 3" in maximum diameter. CI began across central KS between 18 – 19 UTC initially in supercell mode. These supercells eventually developed into a mesoscale convective system by 0000 UTC with the primary threats for severe wind and hail.

RaXPol was deployed on a supercell near Hays, KS from 1835 – 1940 UTC. This particular storm was a long-lived supercell that during the RaXPol operations was non-tornadic, though it was tornado warned for most of the deployment. These warnings included the potential for up to 2.5 – 4" hail across the span of warnings issued on this storm. The supercell ended up producing >2" hail, which included a 2.5" report on the SPC database at 1910 UTC near Hays, KS. As such, this made the supercell
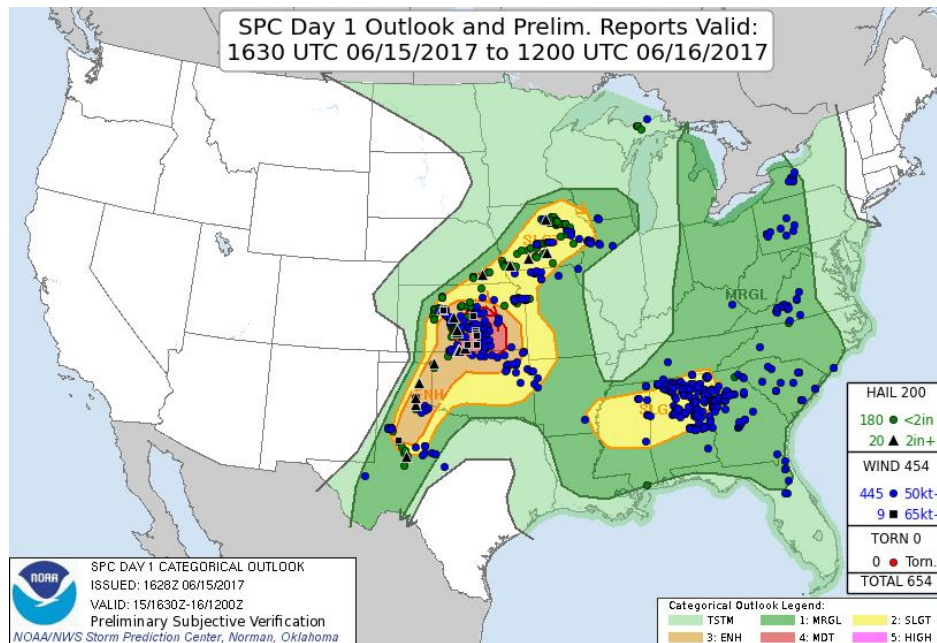
Figure 4.1: Storm Prediction Center Convective Outlook issued 1630 UTC on 15 June 2017 with the verified storm reports overlaid. Note that underneath the core of the reports over central Kansas is a moderate risk.

viable for analysis of the rapidly evolving dual-pol signatures, as full residence time of the hailstones was observed.

During this deployment, RaXPol was in rapid scan mode, with a rotation rate of 180° per second. It was scanning every 2°, up to 20°, allowing for a 12 km maximum altitude view of the storm in roughly 24 sec. This scanning strategy had a maximum range of roughly 40 km and was positioned within 10 − 20 km of the forward flank of the supercell when it was at its most intense. Proximity soundings revealed the environmental freezing level was at approximately 4 km above ground level (AGL). Thus, for gates located >10 km away from RaXPol, observations were made above the freezing level.

The rest of this chapter will focus on PPIs and reconstructed RHIs along the 340° azimuth angle, which is indicated in Figure 4.2. This angle was chosen as the most
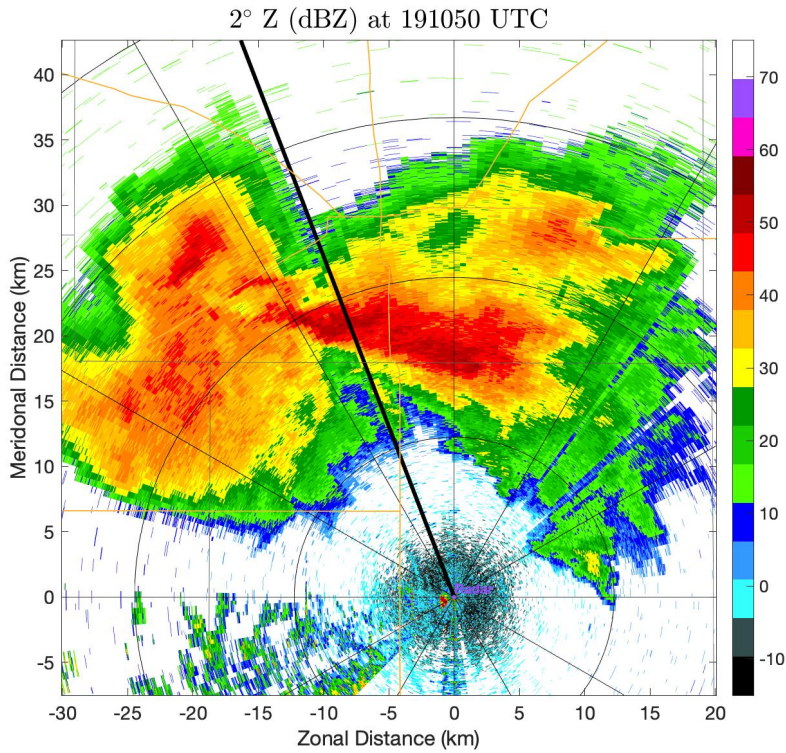
Figure 4.2: RaXPol PPI from 15 June 2017 at 1910:50 UTC near Hays, KS. The black line indicates the location of the 340° azimuth angle that was utilized for the creation of RHIs.

signatures of interest occurred along this azimuth angle and as this was closest to the 2.5" hail report. Emphasis will be placed on the evolution of the dual-pol variables, in particular Z_{DR} and ρ_{hv}.

4.2 Pre-Hail Evolution

RaXPol began operations at 1835 UTC. At this time, the Hays supercell already underwent CI and for the first few minutes underwent rapid intensification (not shown). A new cell began developing at 1845 UTC to the south of the most dominant cell, which quickly intensified and became the primary supercell in this area (Figures 4.3 - 4.4). As
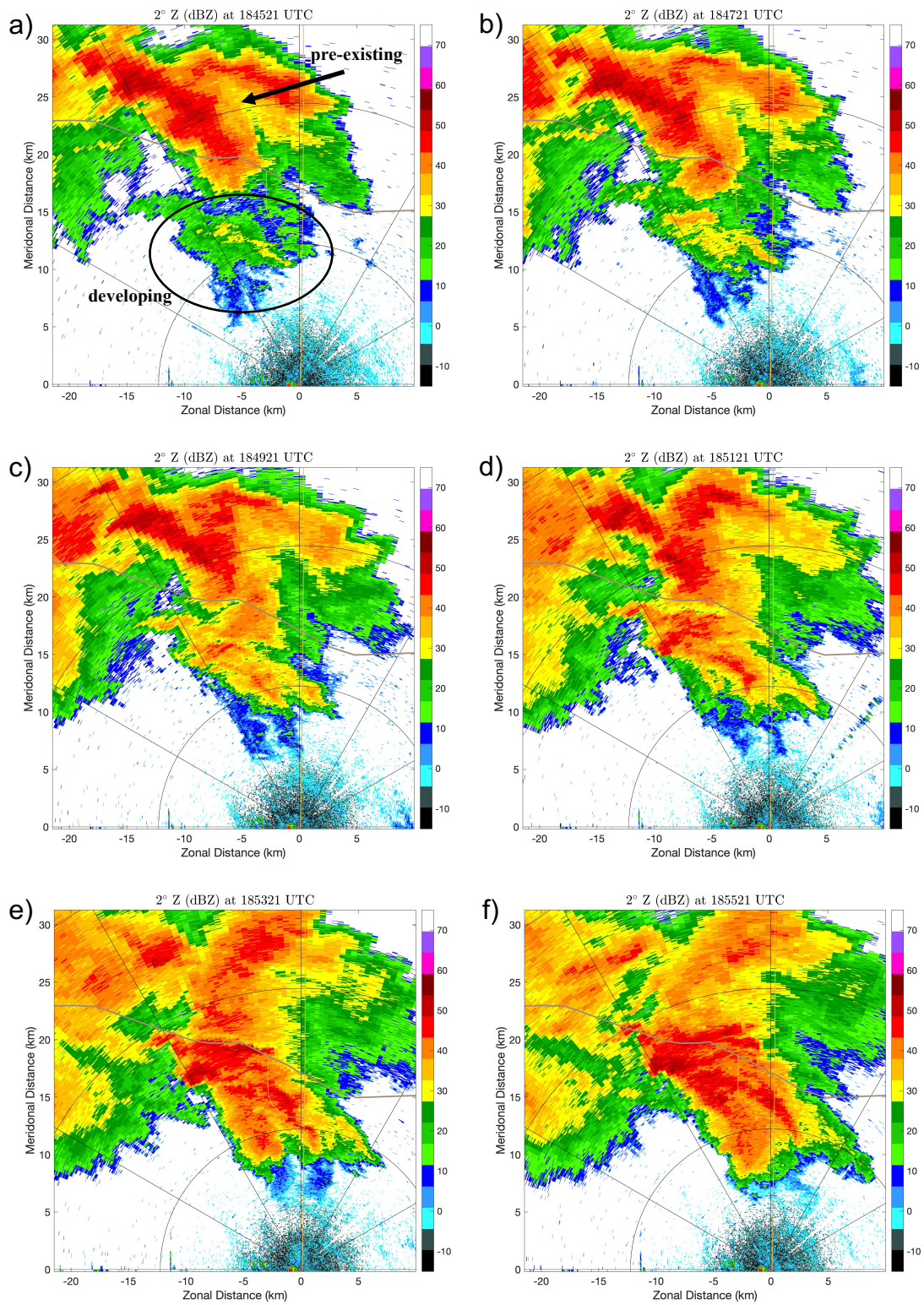
Figure 4.3: RaXPol PPIs of the 2° elevation angle for Z_H on 15 June 2017 from 1845:21 – 1855:21 UTC. In panel a) the arrow indicates the pre-existing storm and the circle indicates the region where a new cell developed.

the storm matured, it took on the appearance of a classic supercell, with the highest Z_H returns associated along the southern forward flank downdraft with more stratiform precipitation located behind it.

The evolution and appearance of the low-level PPIs of Z_{DR} further support the development of a mature supercell prior to peak hail fallout (Figures 4.5 - 4.6). For purposes of this study, the low-level PPIs shown are at the 2° elevation angle. As the southern cell started developing at 1845 UTC, Z_{DR} across much of the developing cell was 4–5 dB, with some lower Z_{DR} near 2–4 dB along the northern edge of the cell. This most likely was the result of size sorting, with the largest drops falling out of the developing cell first, which coincides with the lower Z_H at this time as well. The highest Z_{DR} returns of $4-5$ dB took on the appearance of a Z_{DR} arc along the forward flank until 1851 UTC. At this time, a burst of high positive Z_{DR} returns, exceeding 5 dB, appeared along the eastern portion of the cell (Figure 4.5e). This was coupled with a rapid increase in the Z_H returns at the same location (Figure 4.3e). This burst occurred until roughly 1853 UTC, at which point the positive Z_{DR} field spreads out and decreases slightly in magnitude to be closer to 3–5 dB (Figure 4.5f). By 1900 UTC, the core of the storm was located 15–20 km from RaXPol and was a mature supercell. A Z_{DR} arc was present in the low-levels with differential attenuation occurring as a result of the storm's strong core. Another small burst in Z_{DR} occurred between 1901 and 1903 UTC, which further reinforced the presence of a Z_{DR} arc from 10–20 km (Figure 4.6c–e). From 1905 UTC to the hail fallout time at 1910 UTC, the Z_{DR} arc weakened with returns spanning 3–5 dB, as hydrometeors were advected into the rear flank of the supercell. This is evident as the Z_{DR} arc propagated to this region and the leading edge of the supercell was marked with Z_{DR} returns of 2–3 dB (Figure 4.6f).
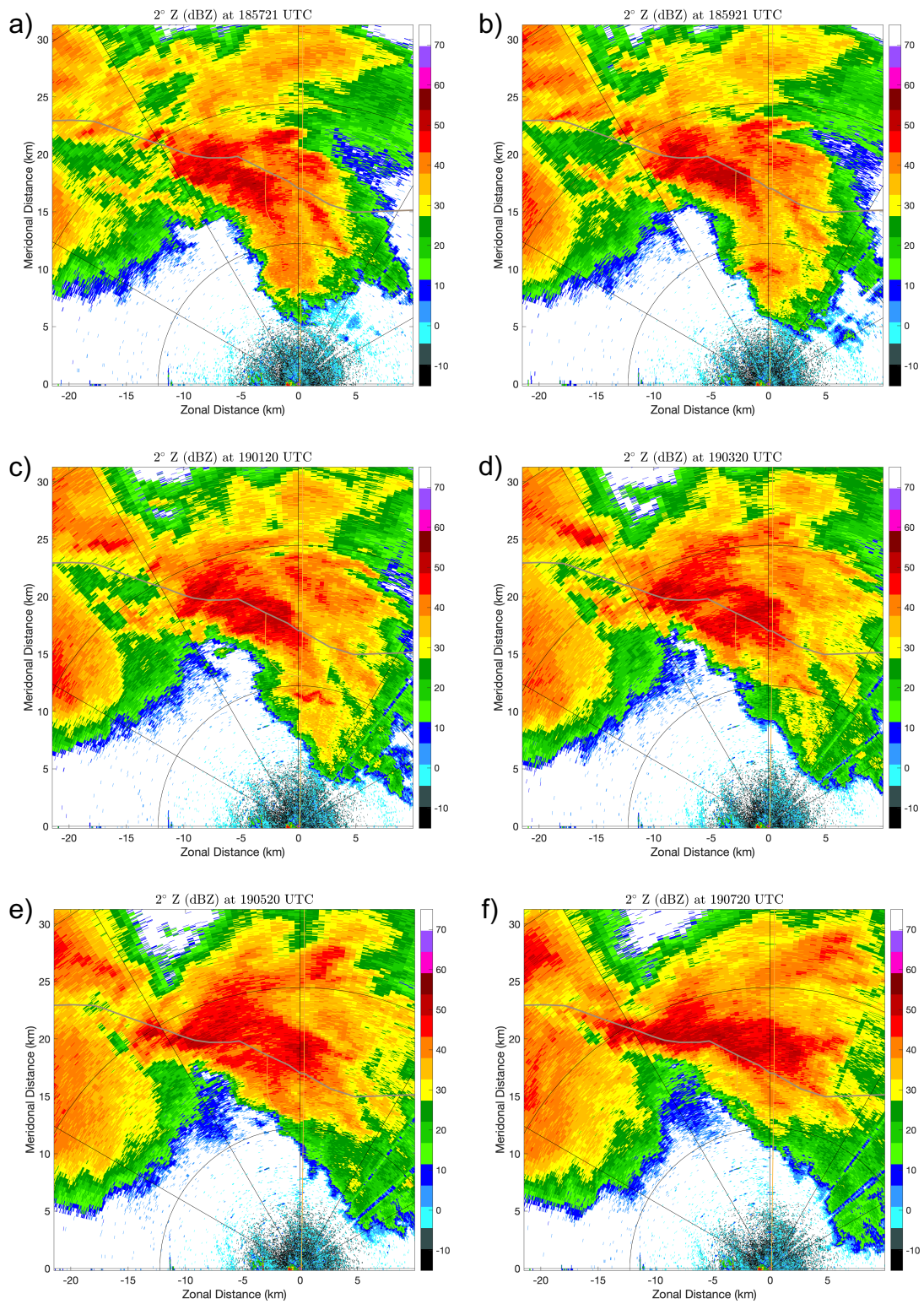
Figure 4.4: Same as Figure 4.3, but from 1857:21 − 1907:20 UTC.
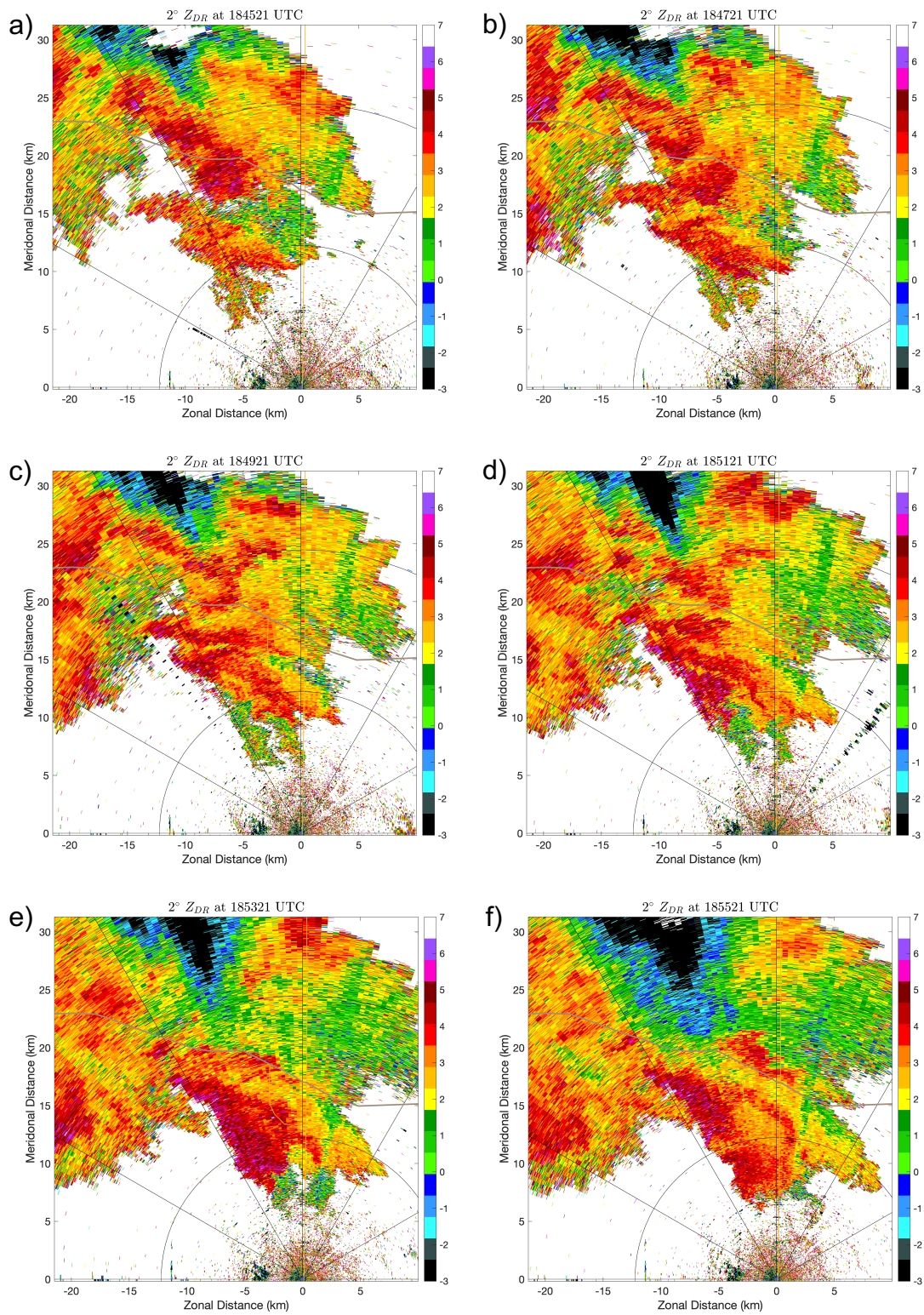
Figure 4.5: RaXPol PPIs of the 2° elevation angle for Z_{DR} on 15 June 2017 from 1845:21 – 1855:21 UTC.
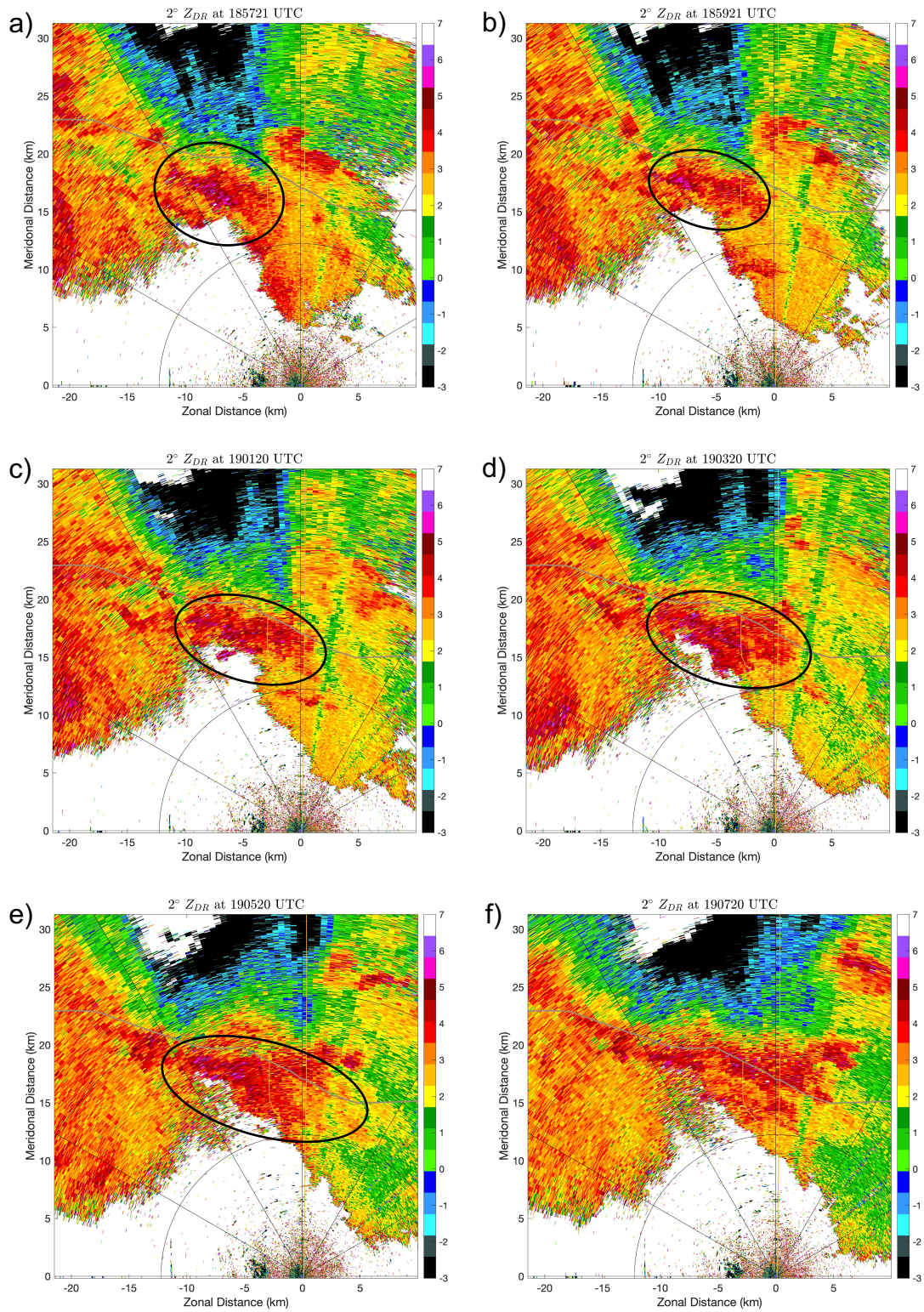
Figure 4.6: Same as Figure 4.5, but from 1857:21 – 1907:20 UTC. The black circles indicate the location of the Z_{DR} burst that created the Z_{DR} arc by 1905 UTC.
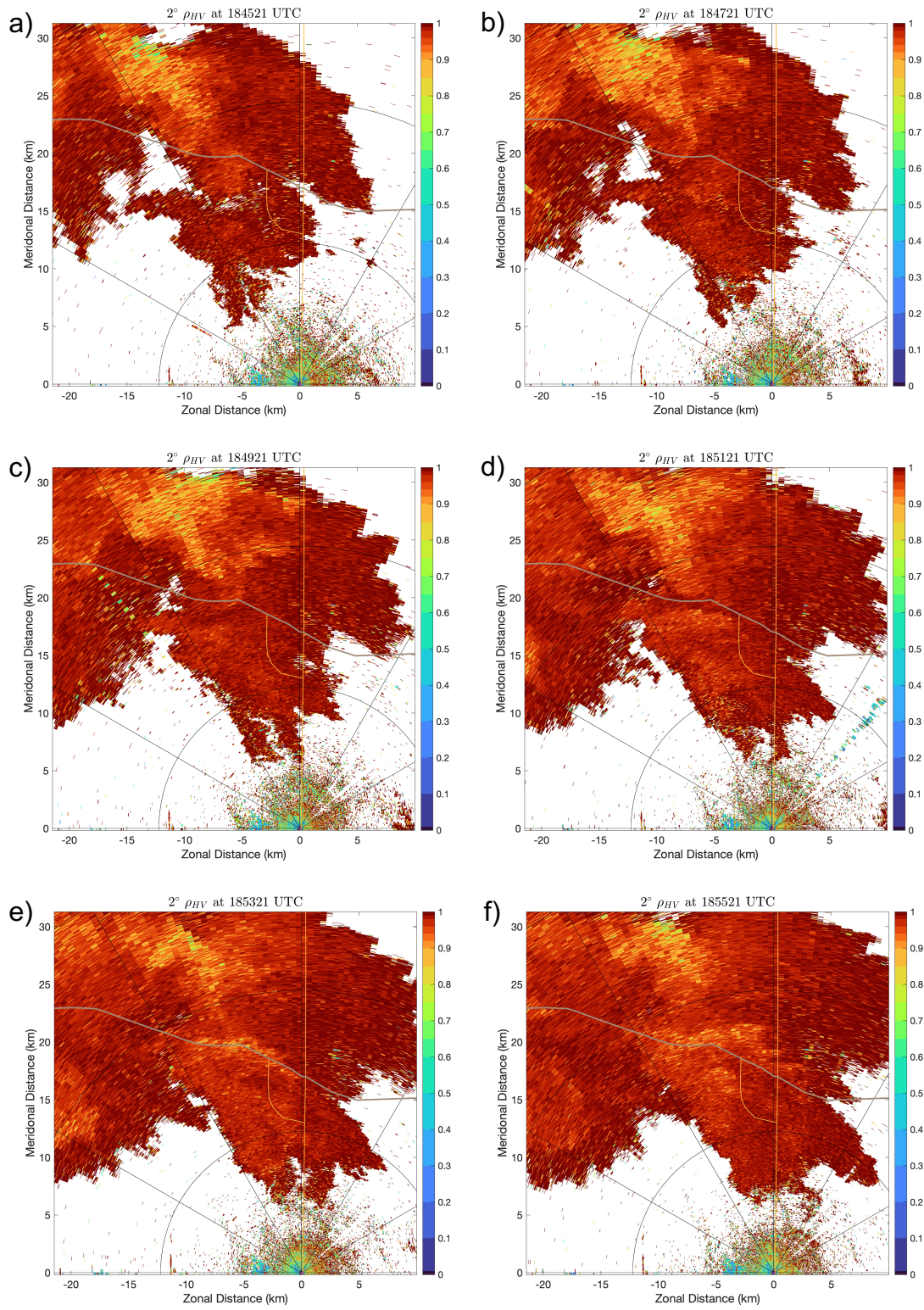
Figure 4.7: RaXPol PPIs of the 2° elevation angle for ρ_{hv} on 15 June 2017 from 1845:21 – 1855:21 UTC.

ρ_{hv} during the initial rapid intensification of the storm remained relatively constant. A gradual reduction of the low-level returns occurred after 1850 UTC, in the same location as a burst of Z_H returns (Figure 4.7). The most notable rapid reduction in the low-level ρ_{hv} leading up to the peak hailfall at 1910 UTC, starting at 1902 UTC. ρ_{hv} values dropped to around 0.7 – 0.8 at 1904:56 UTC and were located downstream of the Z_{DR} arc, matching the understanding of supercellular structure described in (Figure 4.7; Kumjian and Ryzhkov 2008). This arc of lower ρ_{hv} returns lingered until the hail fallout at 1910 UTC (Figure 4.8e–f).

RHIs along the 340° azimuth further reveal the evolution of the supercell prior to the hail fallout (Figures 4.9 – 4.10). Beginning at 1850 UTC, a Z_{DR} column developed between 14 – 18 km. The initial development of the Z_{DR} column occurred between 1850:03 – 1852:27 UTC, during which seemingly small perturbations resulted in an increase in Z_{DR} returns between 14 and 16 km at the mid-levels of the storm (Figure 4.9a–c). The column appeared to almost decay shortly thereafter, from 1853:15 – 1854:03 UTC. After 1854:03 UTC, this developing Z_{DR} column begins to re-intensify, as a result of a core of Z_{DR} returns >5–6 dB that began descending towards the surface at 1852:51 UTC. At 1853:39 UTC, this Z_{DR} core starts ascending into the updraft. This process agrees with the modeling study by Kumjian et al. (2014) which noted that descending hydrometeors with a positive Z_{DR} that got swept into the updraft resulted in the formation of a Z_{DR} column. The Z_{DR} column continued its growth and by 1857:39 UTC was located at the 16 and 18 km range and had a height of approximately 5 km, with peak Z_{DR} returns of 7 dB (Figure 4.10c). Between 1858:27 – 1859:39 UTC, the Z_{DR} column featured a dual-peak, which was brought on by a secondary core of large drops descending and being swept into the updraft, thereby giving the temporary appearance of two columns (Figure 4.10d–e). These two cores quickly merged together
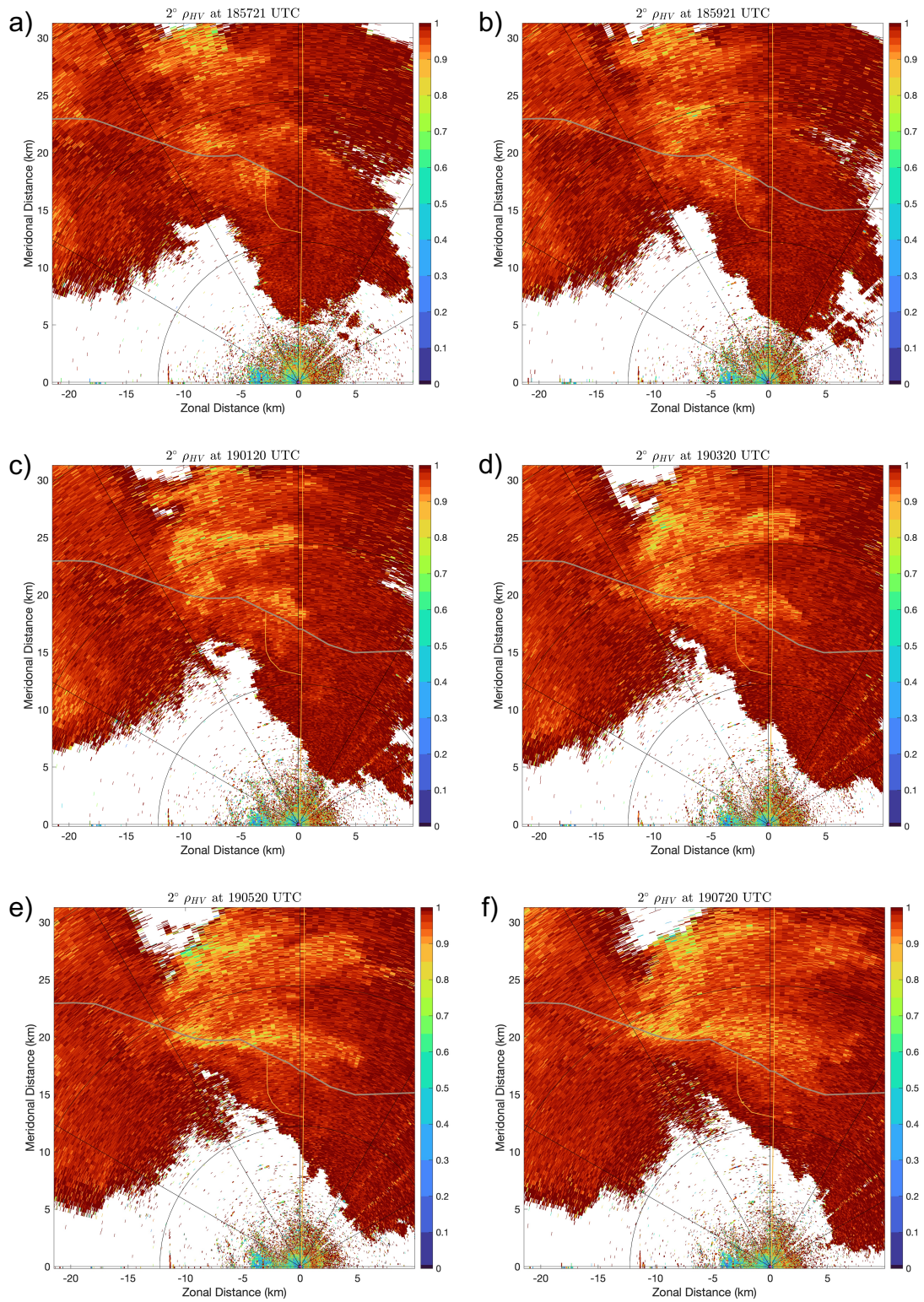
Figure 4.8: Same as Figure 4.7, but from 1857:21 − 1907:20 UTC.

and by 1900 UTC, the Z_{DR} column was a well developed singular column, located between 16 and 20 km with a column height approaching 6 km AGL, or roughly 2 km above the environmental freezing level (Figure 4.10f). From 1900 to 1910 UTC, the column remained in a relatively steady state, located at roughly the same location within the storm.

The Z_{DR} column served as one of the primary precursor signatures for a hail fallout signature that occurred between 1908 and 1911 UTC, along the same 340° azimuth angle. Kumjian et al. (2014) noted that the development of the Z_{DR} column has a lagged correlation with an increase in surface hailfall by approximately 14 min. In this case, the Z_{DR} column developed on roughly that time frame relative to the surface hail fall, with an offset of roughly 15 – 20 min between the initial growth of the Z_{DR} column and it reaching its mature stage. Additionally, the growth of Z_{DR} column and its subsequent small scale processes was able to be resolved in an observational sense, whereas Kumjian et al. (2014) was a modeling based study and a traditional WSR-88D cannot resolve features occurring on the order of <5 min and lacks the vertical data continuity to be able to see vertical structure like this.
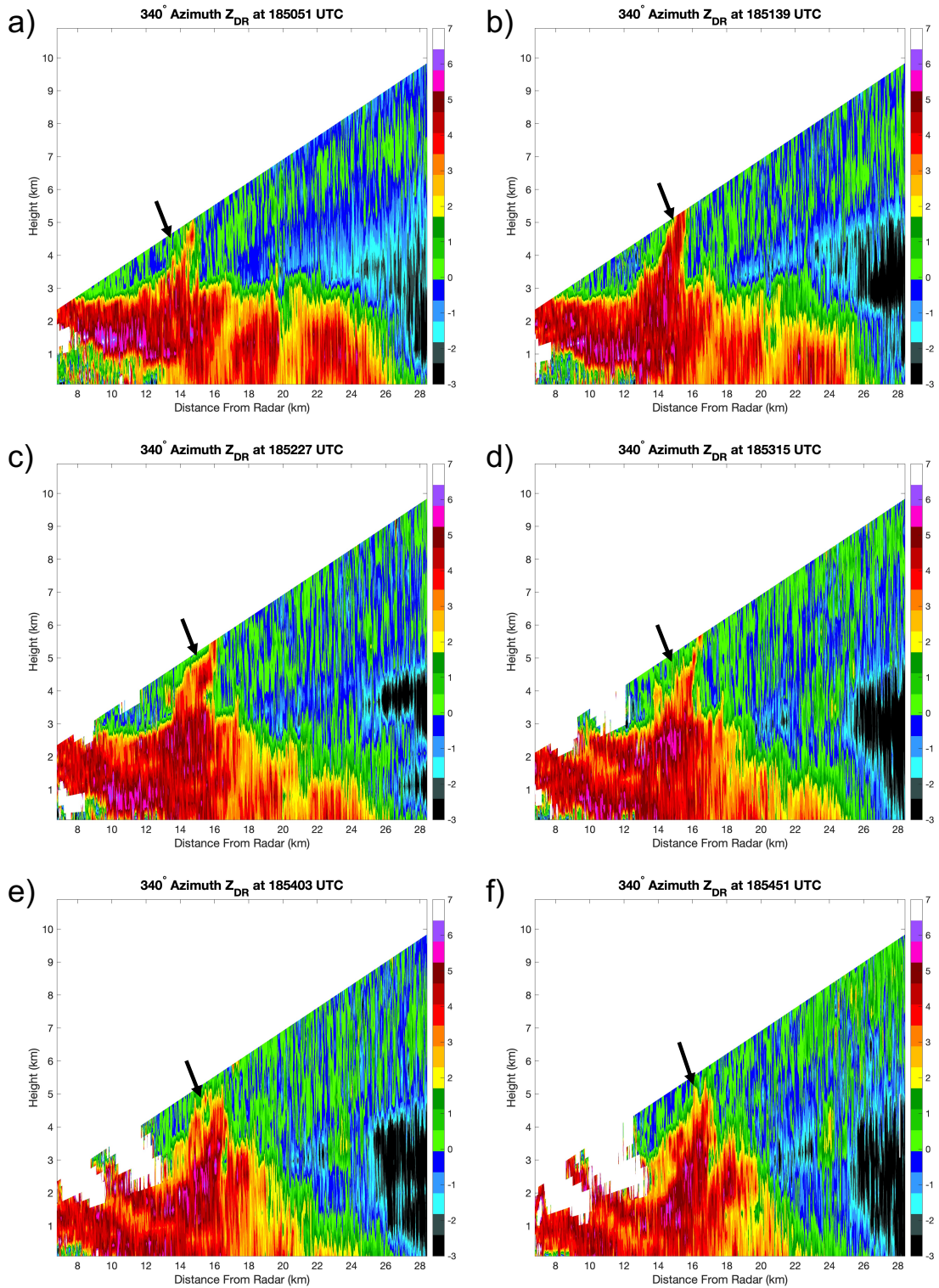
Figure 4.9: Evolution of Z_{DR} along the 340° azimuth from 1850:51 to 1845:51 UTC. The arrows indicate the location of the developing Z_{DR} column.
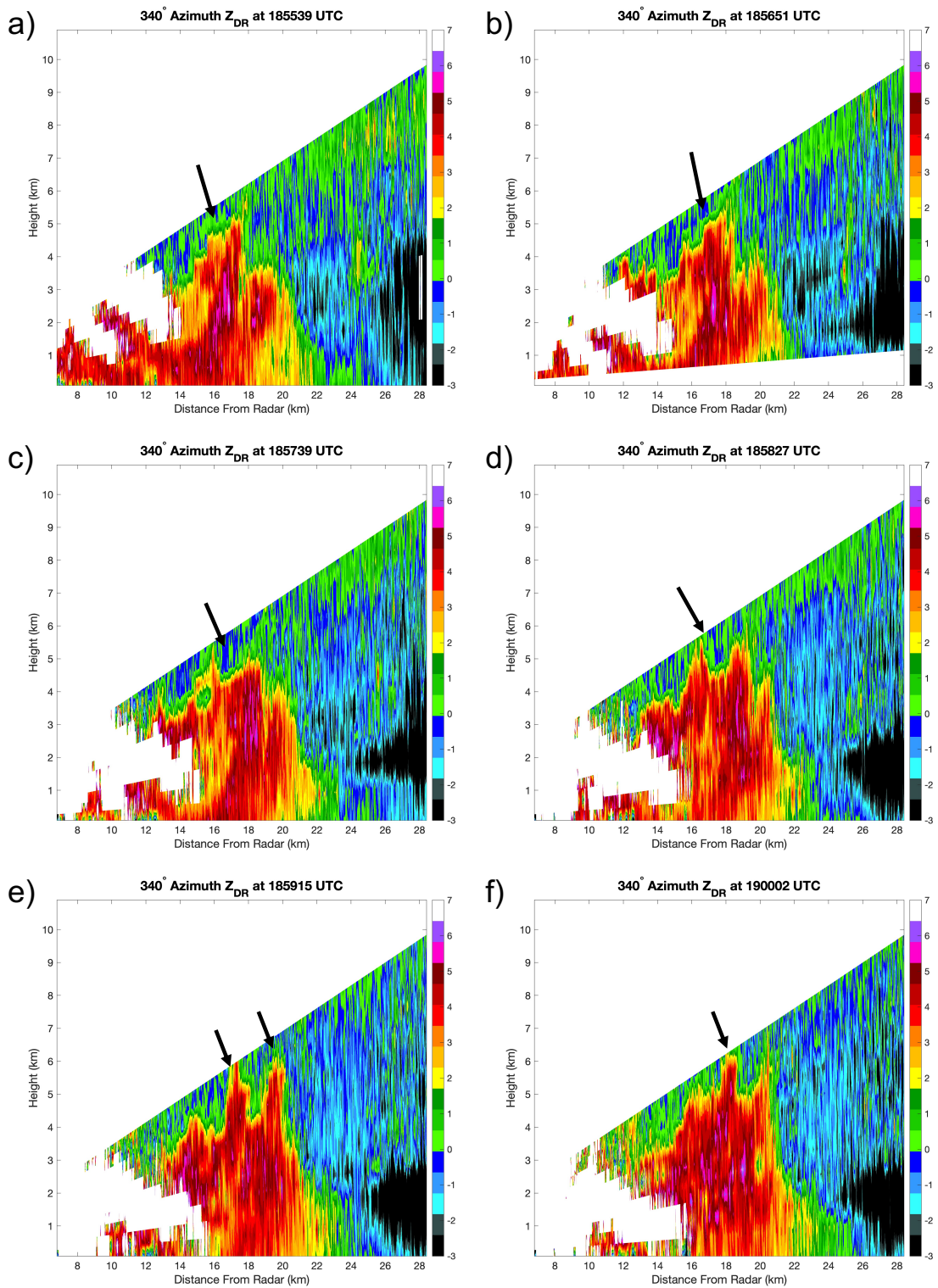
Figure 4.10: Same as Figure 4.9, but from 1855:39 to 1900:02 UTC. The arrows indicate the location of the developing Z_{DR} column.

4.3 Hail Fallout Signature

The growth of the Z_{DR} column for this storm served as a precursor signature for hail fallout in the Hays storm that occurred beginning around 1908:50 UTC. Since the storm motion was relatively stagnant between the development of the Z_{DR} column and this hail fallout time, the same 340° azimuth RHI is used, beginning at 1908:50 UTC. This hail fallout signature was located along the leading edge of the forward flank downdraft, between 10 – 15 km in range from RaXPol. This hail core descending into a relatively precipitation-free region. Presently, this feature has limited observations noted in scientific literature using rapid-scan radar observations, thus making this descending hail core of particular interest for this study.

The time evolution of this hail fallout is given in Figures 4.11 – 4.12. The signature became notable starting at 1908:50 UTC as a small enhancement of lower ρ_{hv} returns around 3 km in height. This area of reduced ρ_{hv} rapidly expanded and decreased in magnitude, with returns as low as 0.6 by 1909:38 UTC (Figure 4.11g). Within this time frame, the shape of the ρ_{hv} core developed into a u-shape, with the lowest ρ_{hv} values along the leading edge of the core. The first <1 min of this signature featured quasi-steady Z_{DR} returns of near 0–1 dB. By 1909:38 UTC, positive Z_{DR} returns around 3–4 dB began appearing along the upper portion of the reduced ρ_{hv} region, with the lower portion starting to also feature negative Z_{DR} returns (Figure 4.11i).

By 1910:02 UTC, the descending hail core featured a prominent reduced ρ_{hv} core with a blossoming of Z_{DR} returns of 4–5 dB occurring along the upper portion of the core (Figure 4.12a,c). The leading edge of the core at 1910:02 UTC had ρ_{hv} returns as low as 0.6 – 0.7 with Z_{DR} returns remaining negative, with some bins as low as -2 dB. The u-shape to the core that developed within the first minutes of this signature became
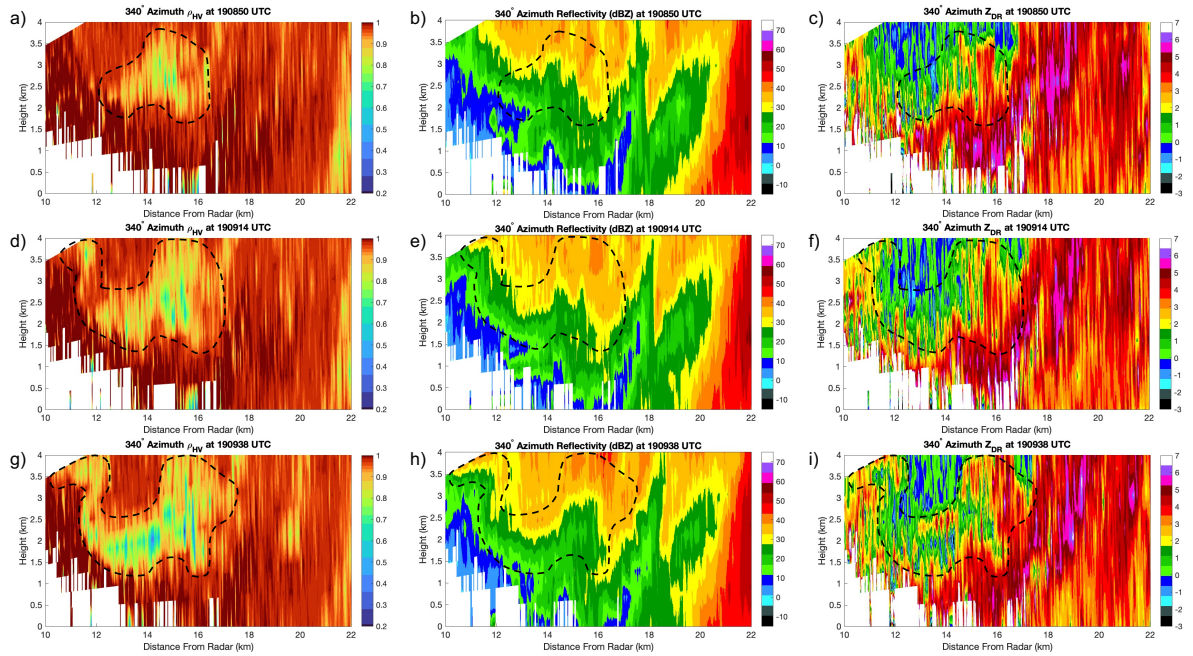
Figure 4.11: RHI plots along the 340° azimuth of left) ρ_{hv}, center) Z_H and right) Z_{DR} from 1908:50 – 1909:38 UTC. The dashed black line on each panel represents the outline of the hail fallout signature.
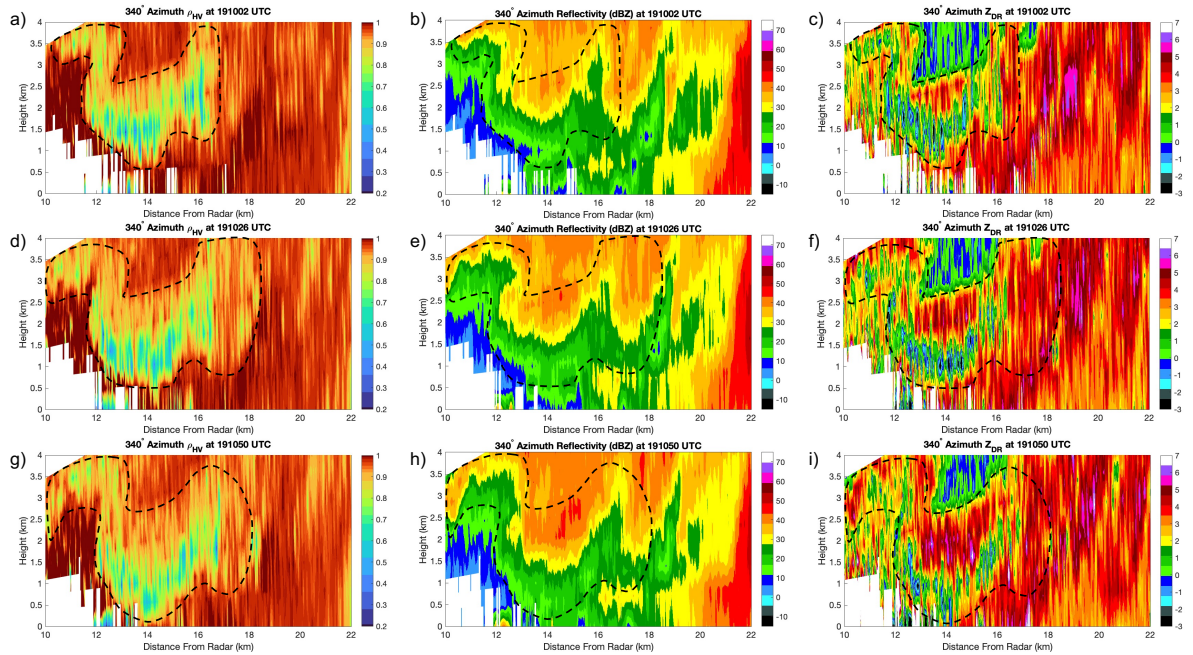
Figure 4.12: Same as Figure 4.11, but from 1910:02 – 1910:50 UTC. The dashed black line on each panel represents the outline of the hail fallout signature.

even more prominent by 1910:02 UTC and this shape became readily apparent on Z_{DR} as well. The descending hail core was best developed by 1910:26 UTC (Figure 4.12d–f). ρ_{hv} returns along the leading edge went slightly up in magnitude compared to 1910:02 UTC, but still were reduced with returns of 0.5 – 0.6. Along the upper portion (2 – 2.5 km AGL), ρ_{hv} was indicative of hail, with returns near 0.9, but was higher in magnitude than the leading edge of the hail core.The positive Z_{DR} along the upper portion of the core blossomed and nearly doubled in area. Z_{DR} returns within this core also increased, with some gates >6 dB. The descending core began to reach the surface by 1910:50 UTC, but still featured a prominent reduced ρ_{hv} core in a u-shape with a large separation of the Z_{DR} persisting. The magnitude of the positive Z_{DR} core increased even as the core reached the surface, with a small number of bins >7 dB, though these returns may be either noise or radar mis-calibrations.

The Z_H returns within this hail signature were less than what was expected for hail, though we still conclude that this signature was a hail fallout signature. Throughout much of the evolution of the fallout signature in Figures 4.11 – 4.12, the hail core was along the leading edge of a gradient in Z_H, but was within an area of Z_H <40 dBZ. However, most studies with Z_H >50 dBZ are observed with S-band radar systems. Snyder et al. (2013) noted that use of an X-band system, like RaXPol, can result in Z_H <50 dBZ. Some of this can also be due to Mie scattering effects, which will result in a Z_H that is lower in an X-band system compared to S-band (Snyder et al. 2010). As such, while the Z_H for this core was low throughout its entire lifetime, this does not discredit the appearance of it being a hail core, especially since ρ_{hv} and Z_{DR} were supportive of hail.

Additionally, this signature was confirmed to be a hail fallout signature and not just a radar artifact primarily through the use of 3D plots (not shown). The fallout signature encapsulated multiple azimuth angles with the bowing u-shape extending

across these azimuths, like that seen in Figures 4.11 – 4.12. Ground truth provided through SPC reports, as well as photos and videos from social media around the same time, further supported the notion that this signature was indeed a descending hail core.

In looking at the time evolution, one of the key features that stood out was the stratification of both Z_{DR} and ρ_{hv} with time. The dual-pol variables within this hail fallout signature are able to reveal the rapidly-evolving microphysics at play in this storm, and the ability to isolate these processes within a hail core descending into a precipitation-free region. The 340° RHI at 1910:26 UTC, provided in Figure 4.13, provides the best representation of the stratification of the dual-pol variables. Overlaying the 0.9 ρ_{hv} contour to represent the descending hail core (black line; Figure 4.13) allowed this hail fallout signature to be represented as three distinct layers. If using the 14-km range gate as a representation, these layers span from (1) 0.5 – 1.5 km, (2) 1.5 – 2.75 km, and (3) >2.75 km.

Layer 1 featured a region of $\rho_{hv} < 0.9$, with $Z_{DR} < 0$ dB, with some bins as low as -2 to -3 dB (Figure 4.13). Layer 2 in contrast, still featured $\rho_{hv} < 0.9$, but Z_{DR} is now > 0 dB, with returns as high as 5–6 dB. In this layer though, ρ_{hv} was higher than the ρ_{hv} in layer 1, but remained generally consistent throughout the layer. Z_H within layer 2, in contrast, gradually increased with height across the layer (see Figure 4.12e). Aloft from this, layer 3 features $\rho_{hv} > 0.9$ along with Z_{DR} generally near $0 - 1$ dB. Using this, physically the layers represent (1) sparse concentrations of large, dry hail, (2) smaller, melting hail and a region of drop shedding and (3) melted and frozen drops. Sparse concentrations of large hail in layer 1 is the result of the reduced Z_H, which can occur if there are fewer hydrometeors within a scattering volume. The melting hail stems from the study of Rasmussen and Heymsfield (1987), which found that drops develop a
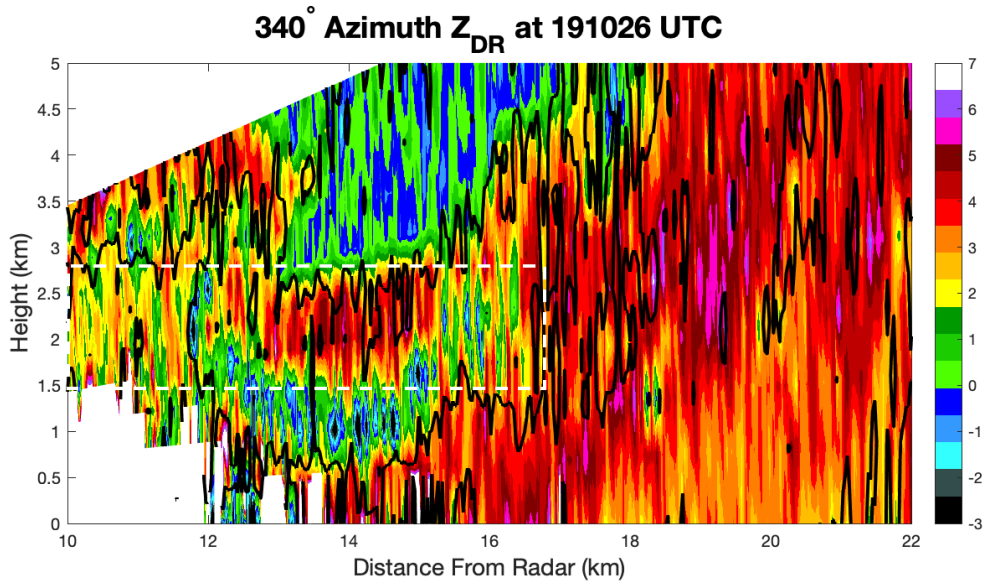
Figure 4.13: Z_{DR} (filled contours) with the 0.9 ρ_{hv} overlaid (black contour) at 1910:26 UTC on 15 June 2017 near Hays, KS. The horizontal white dashed lines indicate the separation between the hail layers, with layer 1 being below the 1.5 km line, layer 2 being inside the box and layer 3 being above the line at 2.75 km.

torus of water along its central axis as it melts. This then makes the hailstone appear more oblate in nature, thus giving a higher Z_{DR} while still featuring lower ρ_{hv} within the scattering volume as the shapes of the hydrometeors are not uniform. The lowest ρ_{hv} returns also occurring within this time frame further support active hail melt as the low ρ_{hv} can be indicative of the period of time with the most liquid water on the surface of the hailstone. The melted and frozen drops then follow behind, where some of these drops may have been shed off the surface of the hailstones in layer 2.

The leading edge of the hail core, which is assumed to be mostly large hail, features a fall speed of roughly $16 - 22$ m s^{-1} based on estimates tracking the leading edge of the hail fallout signature in Figure 4.11 – 4.12. Using Equation 2.3 yields a hail size of 1.82 – 3.07 cm (or 0.72 – 1.2 in). This difference in estimated hail size could be due to the physical properties of the hail itself, such as variations in the shape or density, or could be a result of the drag force impacting the hailstones, or could be that the hailstones

did not fall at this calculated terminal velocity. Additionally, the stratification into layers resulted due to size sorting occurring as the hydrometeors are descending. Large hailstones are going to fall faster due to their larger mass and fall speeds, which will get progressively lower with decreasing size. This then allows for the core to split into distinct layers with time, especially as hailstones melt and shed off more drops, thus reducing their fall speed.

4.4 Post-Hail Evolution

The hail fallout signature modified the low-level PPIs of the Hays storm in the few minutes following hail reaching the surface. In particular, the low-level Z_{DR} field had the demise of the Z_{DR} arc immediately preceding the hail fallout at low-levels (Figure 4.14). With the arrival of the surface hailfall, however, a burst of positive Z_{DR} values to the east of the fallout signature gave a momentary regeneration of the Z_{DR} arc (Figure 4.15). The Z_{DR} increase was coupled with a burst of Z_H values, which shortly thereafter became the dominant cell on this particular storm (Figure 4.16). The combination of these two bursts most likely was indicative of active size sorting associated with a new updraft pulse, similar to what was observed in the hail pre-cursor signatures. The cyclic feedback cycle persisted throughout the storms lifetime, some of which was captured by RaXPol, but for the sake of brevity and due to data quality issues, is not included within this study.

In a cross-sectional view, following the hail fallout signature, the Z_{DR} column along the 340° azimuth collapsed. This decay started after 1912:26 UTC and occurred within the the next 3 – 4 min (Figures 4.17 – 4.18). The most rapid decay of the Z_{DR} column occurred between 1913:38 and 1915:38 UTC, in which Z_{DR} values between 3 and 5 km
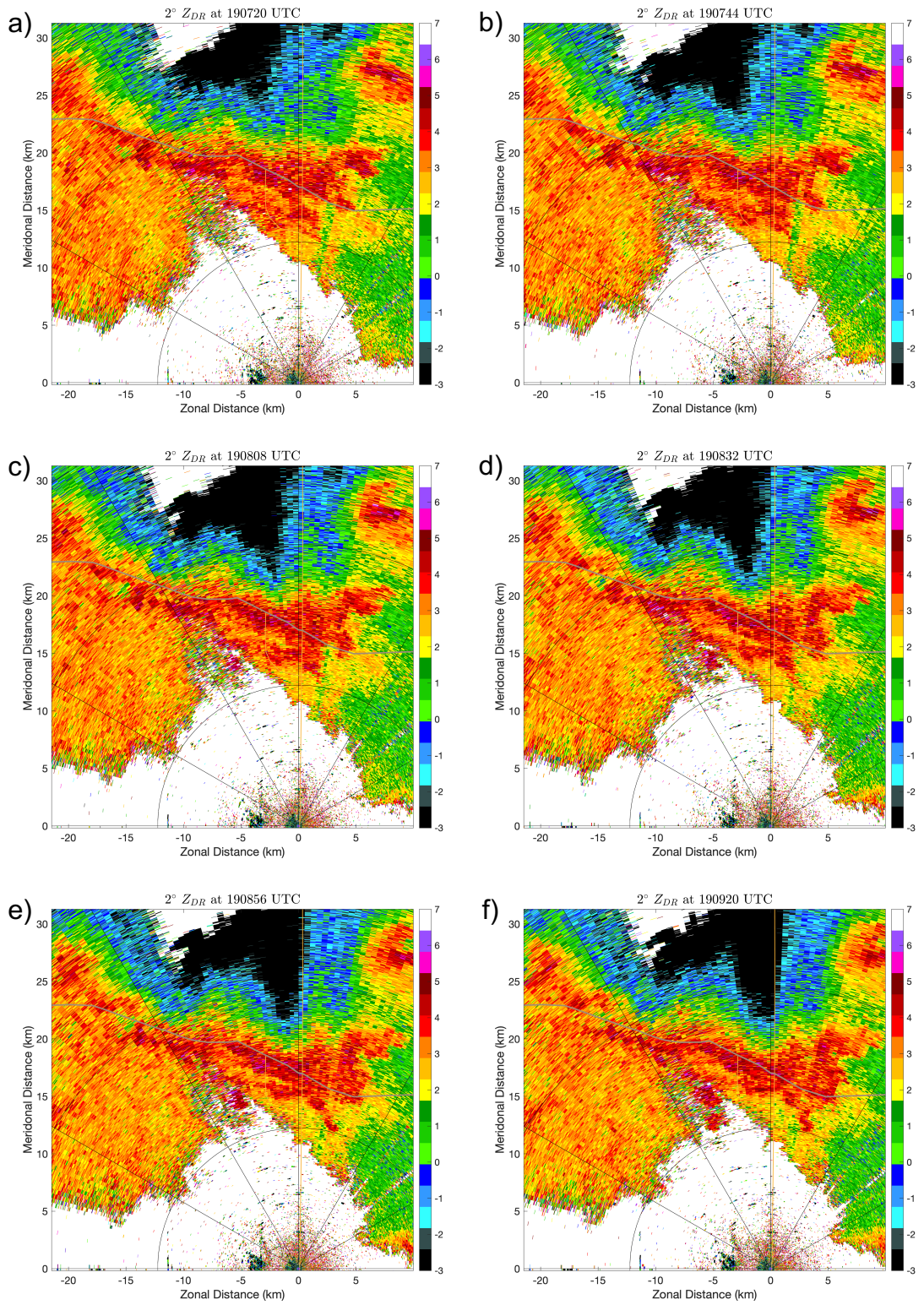
Figure 4.14: PPI plots of Z_{DR} at the 2° elevation angle from 1907:20 – 1909:20 UTC on 15 June 2017 near Hays, KS.
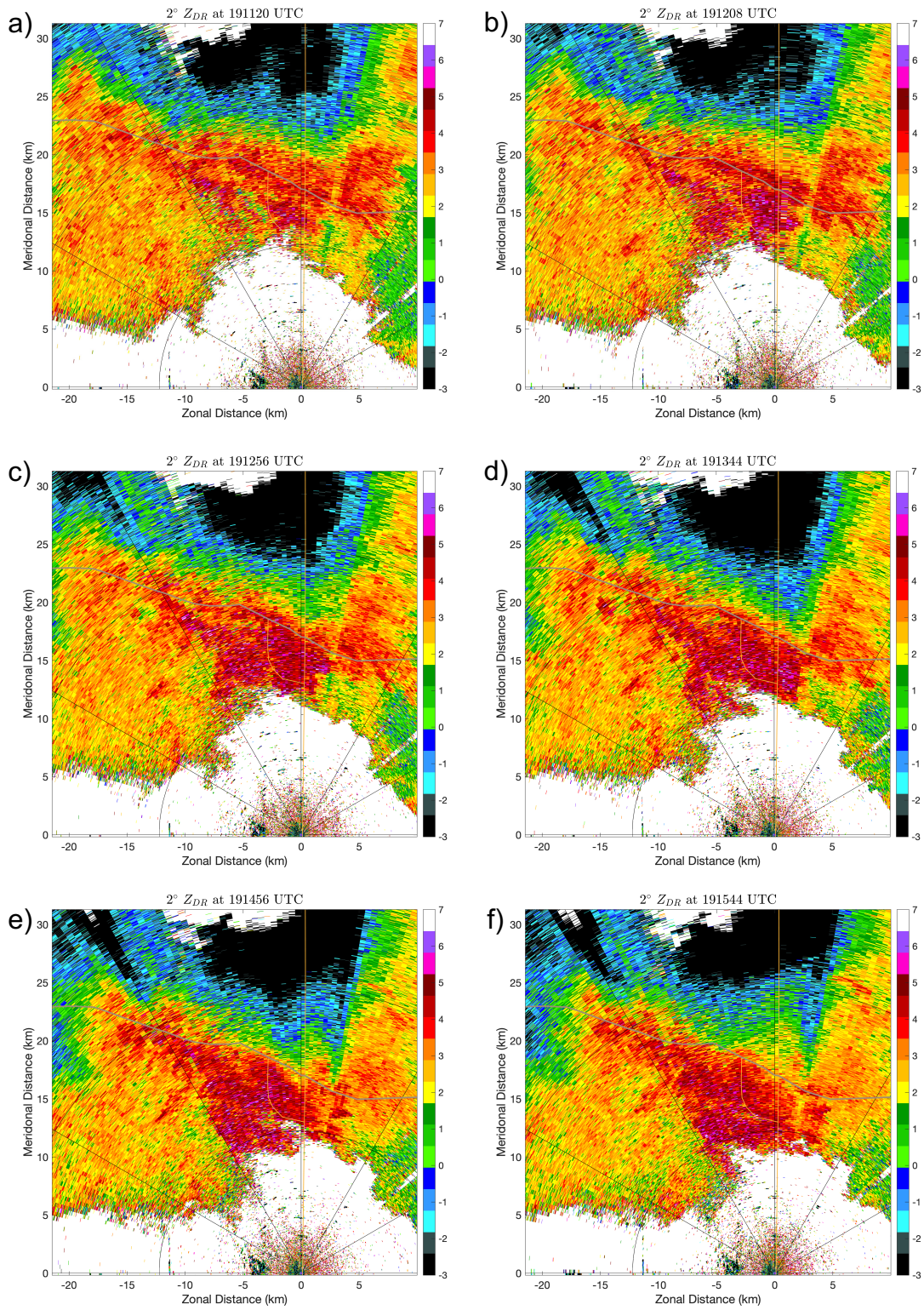
Figure 4.15: PPI plots of Z_{DR} at the 2° elevation angle from 1911:20 – 1915:44 UTC on 15 June 2017 near Hays, KS.

55
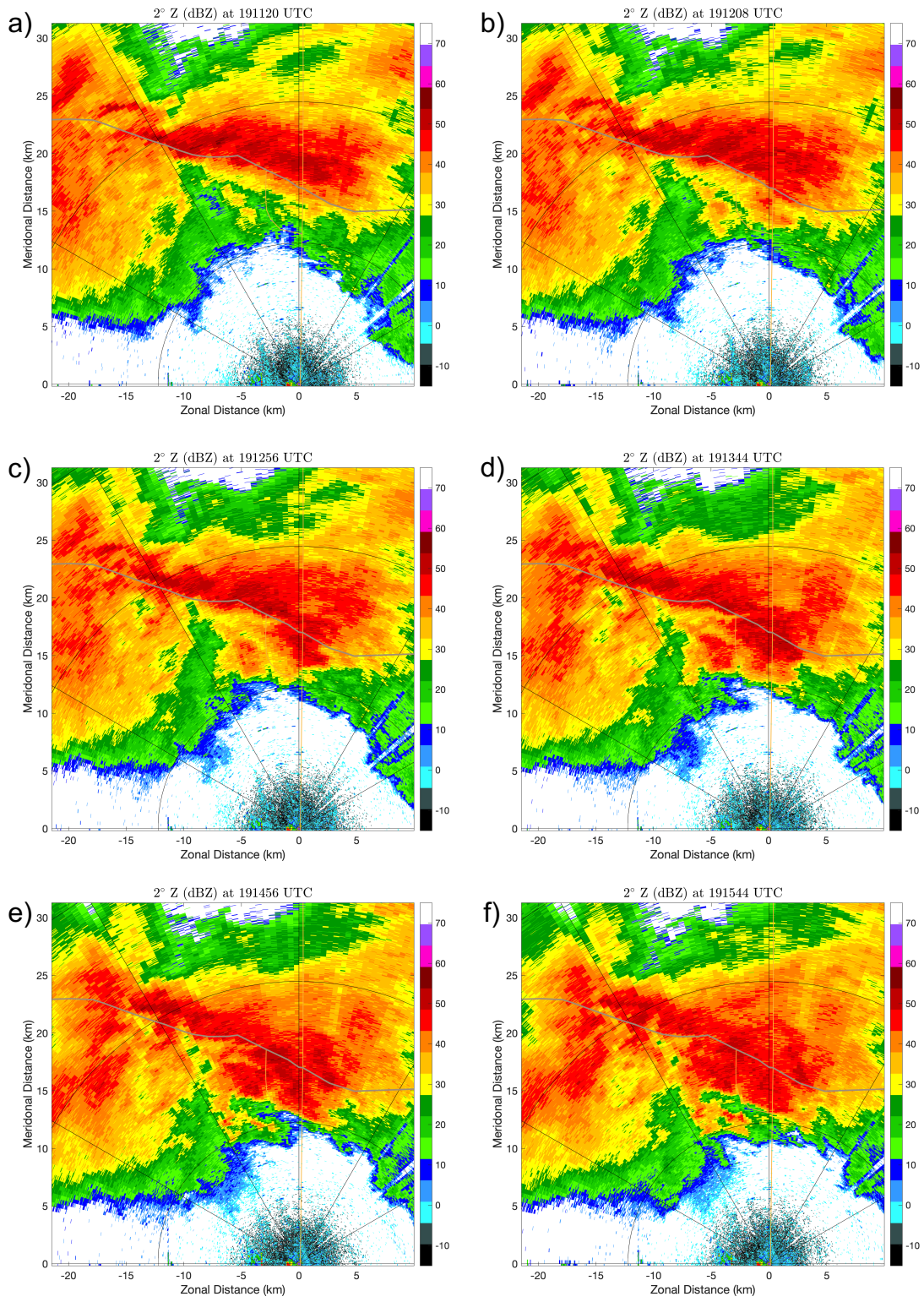
Figure 4.16: Same as Figure 4.15, but for Z_H.
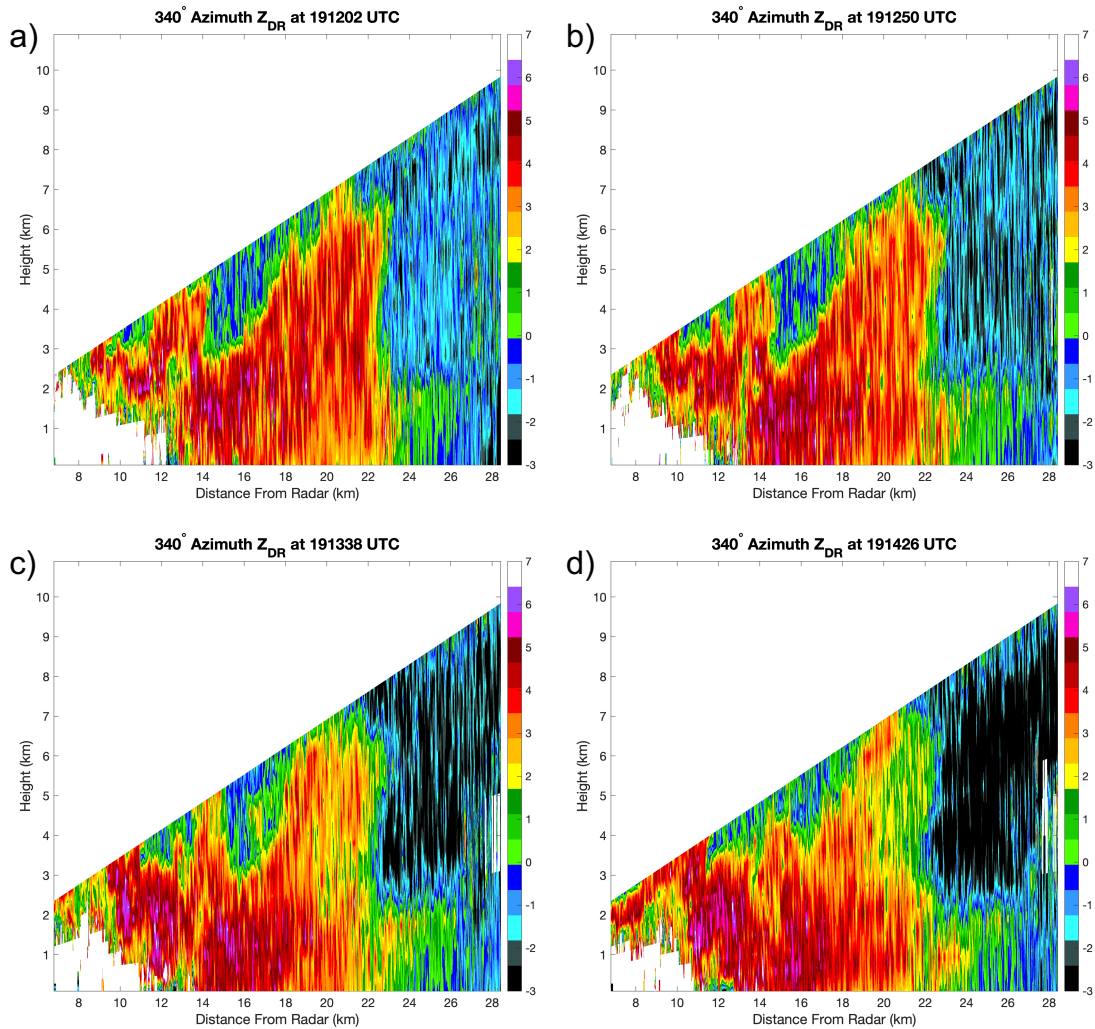
Figure 4.17: RHI plots of Z_{DR} along the 340° azimuth from 1912:02 – 1914:26 UTC.

AGL went from >4 dB to 0 – 2 dB. By 1916:02 UTC, any remnants of the Z_{DR} column between 18 – 22 km are limited. However, a new Z_{DR} column began developing at this time as well, between 12 and 15 km in range (Figure 4.18). This Z_{DR} column formed in a similar manner as the initial one, with a core of positive Z_{DR} returns beginning to descend towards the surface before being lofted into the updraft, causing the formation of the Z_{DR} column.

The development of the new Z_{DR} column allowed for the Hays supercell to be long-lived and eventually grow into an MCS that trekked across the state. This storm continued to produce hail according to the SPC storm reports and as it developed into a MCS, developed severe wind reports as well. RaXPol continued operations until 1940 UTC, but after about 1920 UTC began running into some data quality issues, thus limiting the ability to investigate other potential hail fallout signatures from this particular storm.

4.4.1 Summary and Discussion

This case study from 15 June 2017, near Hays, KS brought forth numerous signatures related to hail production using a rapid-scanning, mobile radar system. First, the birth and death of the Z_{DR} column preceded peak hailfall by 15 – 20 min, after taking roughly 5 min to develop, matching the modeling studies by Kumjian et al. (2014). The high spatial and temporal resolution of RaXPol also allowed for the large drops that contributed to the production of the Z_{DR} column to be observed immediately preceding its development, again matching past modeling studies of Z_{DR} column development. The use of an X-band system that can get in close proximity to a convective storm, like RaXPol, allowed for the microphysics of this storm to be resolved and observed. In particular, size sorting and hail melting were able to be resolved for the first time as stratified layers, which was in large part due to the <1 min update time. This stratification and associated processes, such as the torus of water that develops resulting in positive Z_{DR} matches both Heymsfield (1982) modeling study of hail melt and the associated radar observations of Kumjian and Ryzhkov (2010).The post hail fallout demise of both the Z_{DR} column and Z_{DR} arc match the studies of Kumjian et al. (2014) and Tanamachi and Heinselman (2016), respectively.

In particular, the study performed on the RaXPol dataset highlights the need for rapidly updating, vertically focused but horizontally scanning observations of convection. Volumetric update times on the order of 1 min or less will allow for processes such as size sorting to be resolved, thus allowing for our observational understanding of these processes to increase. As Dennis and Kumjian (2017) have noted, the properties of the updraft itself, including the width, are crucial for understanding hail growth and sizing, so gaining more vertical observations will also aid in gaining a deeper understanding of the evolution and properties of the updrafts associated with severe hailstorms.

One limitation from this this study, however, was the operational feasibility associated with it, as our current NEXRAD system utilized an S-Band system, not an X-Band like RaXPol. Attenuation, in particular, occurs for lower hydrometeor sizes than at S-Band, so while hail fallout was able to be resovled with this case, the repeatability in other storms may be lower, especially if the descending hail core is more embedded within the rain shaft. As such, Chapter 5 will focus on rapidly evolving features using an S-Band system, with update times on the order of 90 – 120 sec.
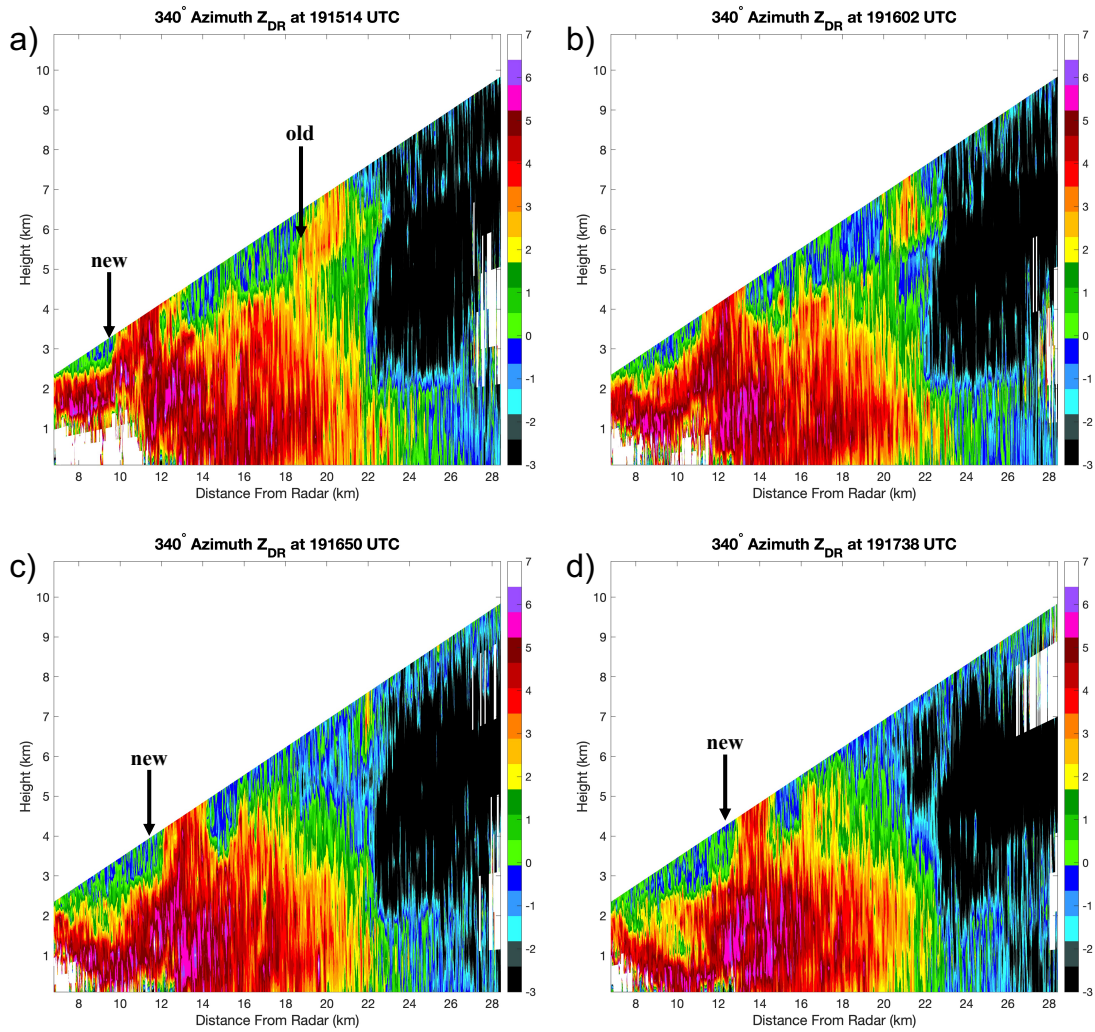
Figure 4.18: Same as Figure 4.17, but from 1915:14 – 1917:38 UTC. The arrows represent the area which featured a descending precipitation core that resulted in the development of a new Z_{DR} column.

Chapter 5

Rapid-Scan S-Band Observations of Hailstorms

5.1 2013 Edmond-Carney Supercell

5.1.1 Storm Background

A passing cold front along with a dryline prompted the risk for severe storms on 19 May 2013. The SPC issued a moderate (2/3) risk for severe storms spanning from central OK to southeastern KS, with a 45% chance for severe hail, including the possibility of significant severe hail (Figure 5.1). A 15% chance for significant tornadoes was also forecasted. Both of these hazards verified in the Edmond-Carney, OK area as an EF-3 tornadic supercell also produced >2" hail, with reports of 2.6" and 2.75" hailstones. KOUN data captured the hail fallout times and tornadogenesis of this supercell, but did not capture the onset of it.

For this case, emphasis will be on the 2120 UTC hail fallout time. This was the peak 95% MESH output for this storm and the storm's position put it in close proximity to a 1.5" and 2.6" hail report. The storm was also located in a position relative to KOUN such that middle and upper level features were able to be analyzed, allowing for an analysis of the storms' rapid evolution prior to this hail fallout time.
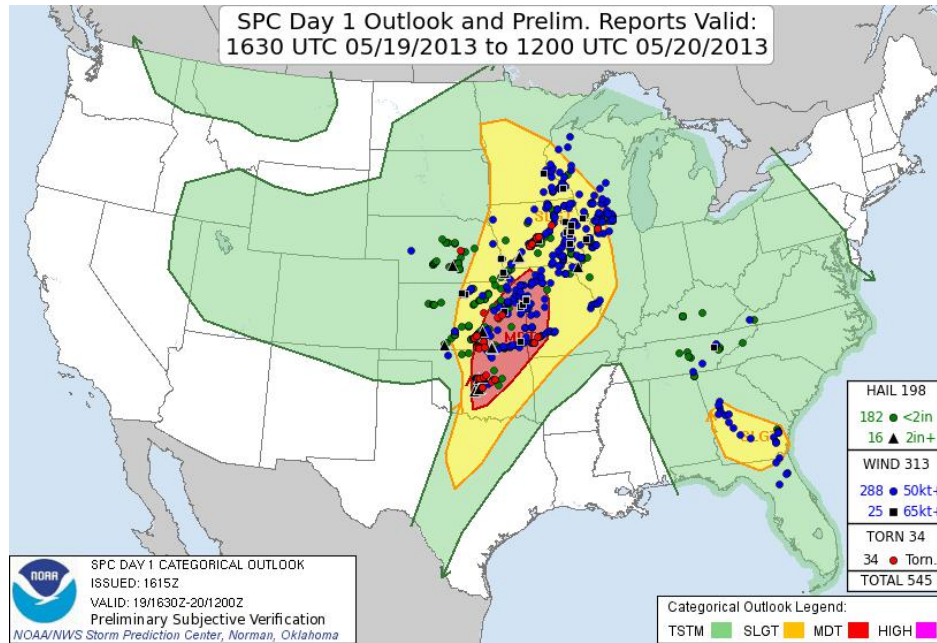
Figure 5.1: Storm Prediction Center Convective Outlook issued 1630 UTC on 19 May 2013 with the verified storm reports overlaid.

5.1.2 Pre-Hail Signatures

Numerous signatures related to convective storms and specifically, hail production, were observed in the roughly 20 min prior to peak hail fallout. One such feature at the mid-levels was the TBSS along with sidelobe spikes, which was seen across all radar variables, but most notable on ρ_{hv} and Z_{DR}. As such, figures of the TBSS will only be presented in ρ_{hv} and Z_{DR}. The TBSS was seen across a large majority of elevation angles, though at slightly varying times throughout, which is due to the descent of the hydrometeors that resulted in the TBSS. The TBSS was first observable on the 7.97° elevation angle, or at 7.2-km AGL, at 2106 UTC (Figure 5.2a). At 2108, the TBSS quickly extended down radial and was coupled with a clear sidelobe spike as well. At 5.95° (5.5-km AGL), the TBSS was first evident at 2108 UTC and extended downradial at 2111 UTC and persisted until 2118 UTC, 2 min prior to large hail fallout (not shown). The 4.05° elevation angle (4.1-km AGL) observed the TBSS beginning
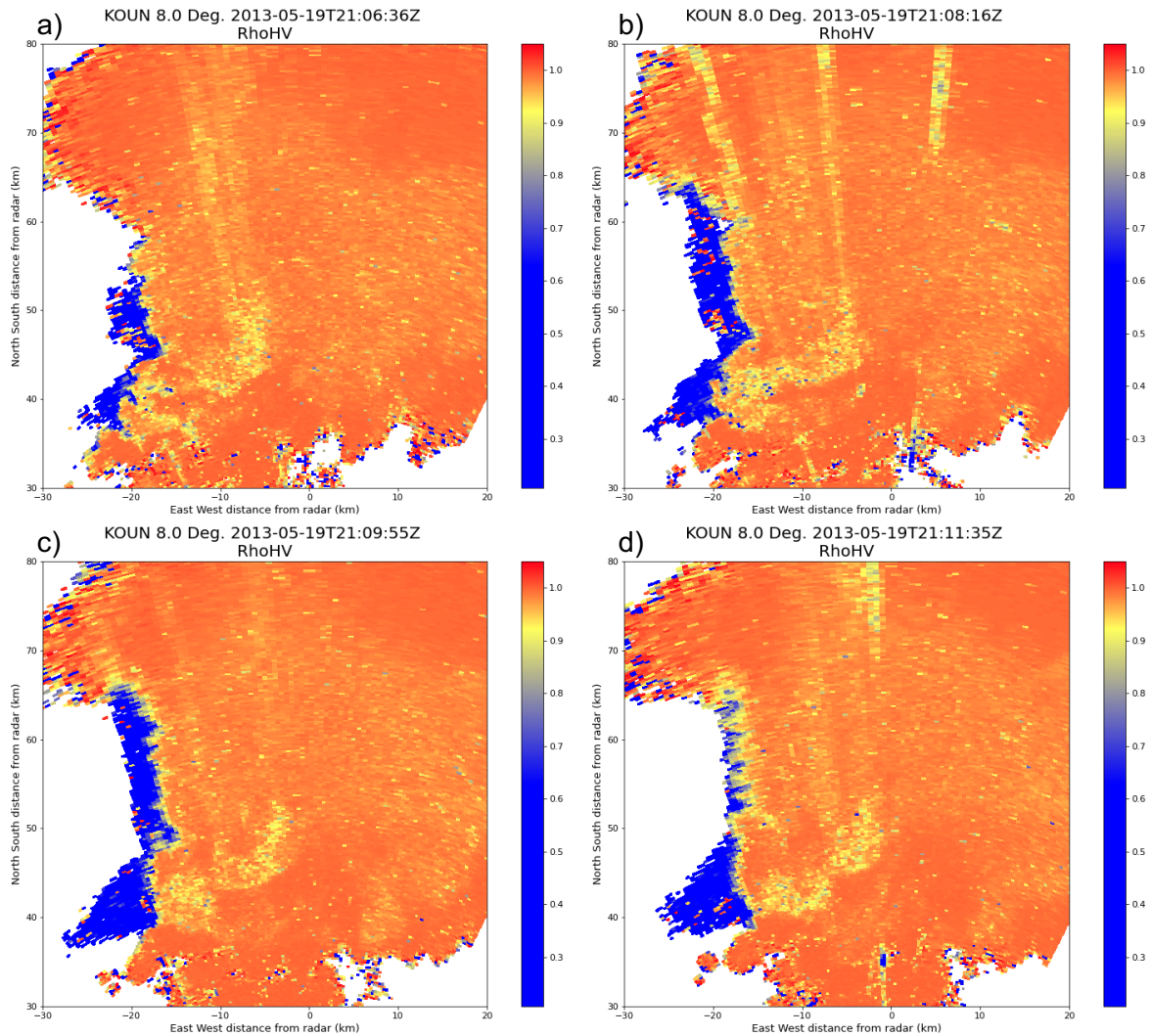
Figure 5.2: PPIs of ρ_{hv} at the 7.97° elevation angle on 19 May 2013 from 2106 – 2111 UTC near Edmond, OK.

at 2111 UTC (Figure 5.3a). This TBSS then increased in length at most notably at 2116 UTC, and was completely dissipated by 2121 UTC. The 3.05° (3.6-km AGL) TBSS appeared most clearly at 2116 UTC and dissipated by 2121 UTC. For elevation angles lower than 3.05°, the appearance of a TBSS occurred, though it quickly became embedded within the ρ_{hv} field and was not as discernible at it was at the midlevels. For many of these elevation angles though, the TBSS only lasted 10 min or less and the

extension down radial persisted for even a shorter time. Additionally, the mid-levels lost the TBSS often <5 min before the arrival of large hail at the surface.

The Edmond-Carney, OK supercell also featured a Z_{DR} column prior to hail fallout, in a similar pattern to the Hays, KS RaXPol case described in Chapter 4. In this case, the Z_{DR} column was already well developed by 2100 UTC, though it took on a visual appearance closer to a Z_{DR} half ring that extended a few kilometers past the freezing level. This structure is in agreement with the findings of Kumjian and Ryzhkov (2008). This feature lingered until 2106 UTC, at which point the Z_{DR} field started rapidly contracting and by 2111 UTC took on the PPI appearance of an isolated column (Figure 5.4a–e). Between 2111 and 2113 UTC, the orientation of the Z_{DR} column at 5.1° rotated slightly, with a peak Z_{DR} of 5 – 7 dB. The area of the Z_{DR} column began to contract most noticeably starting at 2115 UTC, though this area had been gradually decreasing after 2109 UTC. Specifically, a split in the area of the column occurred at 21:16 UTC based on the 5.1° elevation in Figure 5.5c. The Z_{DR} column started to rapidly decay by 2120 UTC, and was mostly decayed by 2123 – 2124 UTC. This decay was apparent as a reduction in the area of positive Z_{DR} in Figure 5.5.

At low-levels, a Z_{DR} arc was present throughout much of the 20 min preceding hail fallout (Figures 5.6 – 5.7). Similar to the Z_{DR} column, the Z_{DR} arc was present by 2100 UTC across the 1.5° (2-km AGL) and 0.97° (1.5-km AGL) elevation angles. A small burst of positive Z_{DR} returns occurred at 2103 UTC, which worked to reinforce the already present Z_{DR} arc by 2108 UTC. The arc briefly weakened at 2110 UTC, but another burst of positive Z_{DR} returns along the southern flank at 2112 UTC deepened the magnitude of the Z_{DR} arc by 2117 – 2119 UTC. This Z_{DR} arc was disrupted by the arrival of the hail core at 2120 UTC marked by a region of $\pm$ 1 dB returns. A large
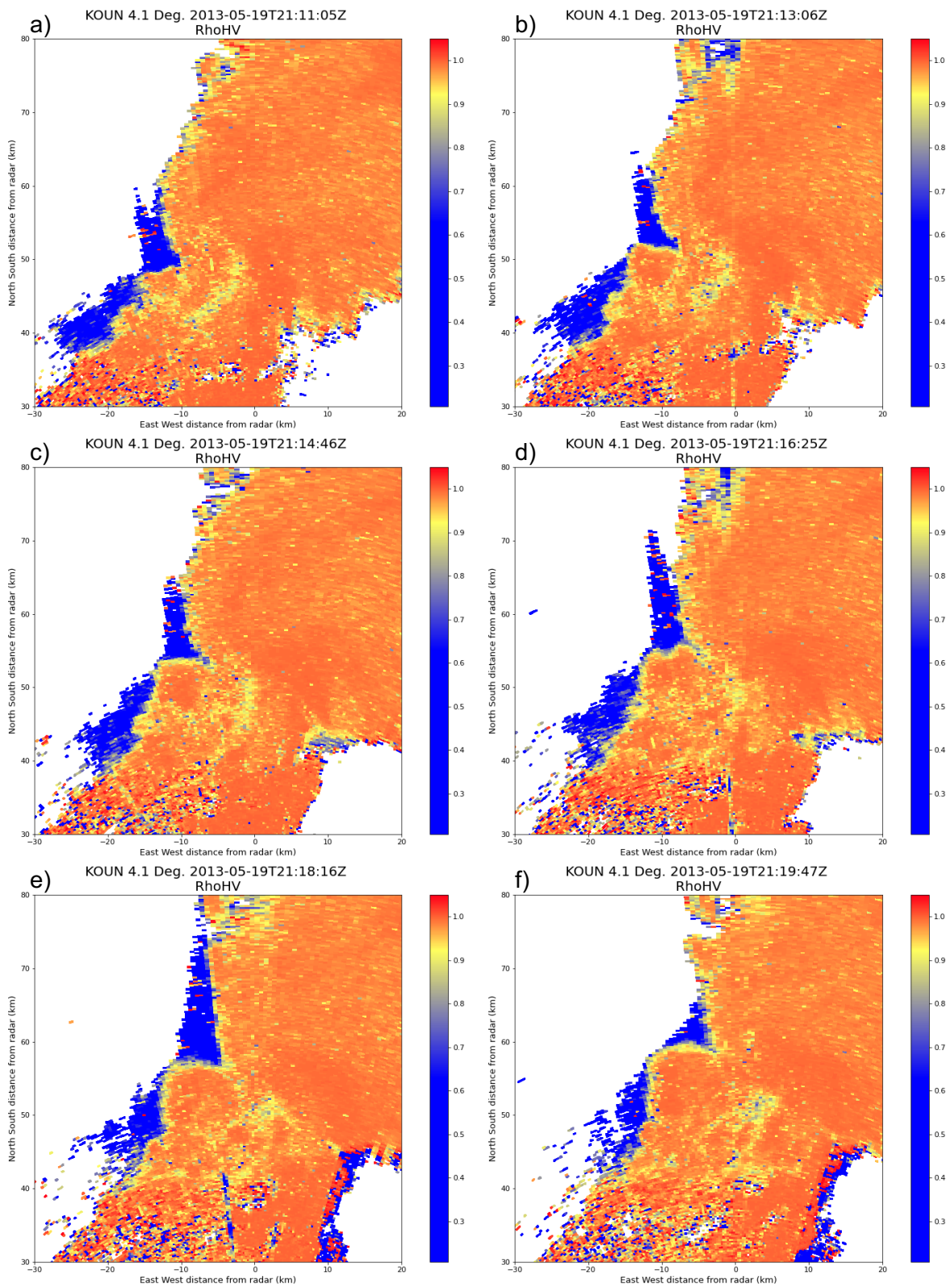
Figure 5.3: PPIs of ρ_{hv} at the 4.05° elevation angle on 19 May 2013 from 2111 – 2119 UTC near Edmond, OK.
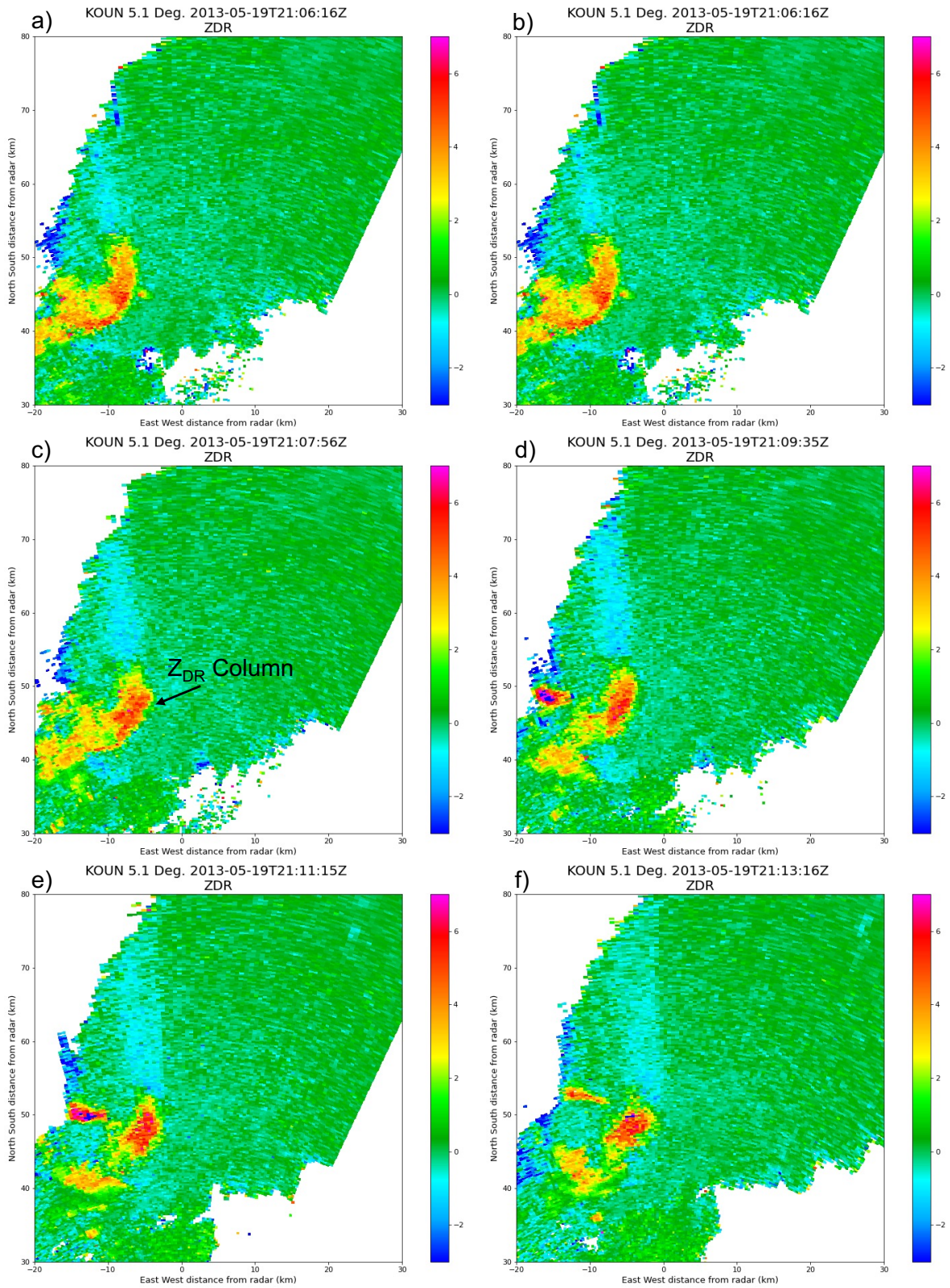
Figure 5.4: PPIs of the 5.1° elevation angle Z_{DR} on 19 May 2013 from 2103 – 2112 UTC near Edmond, OK.
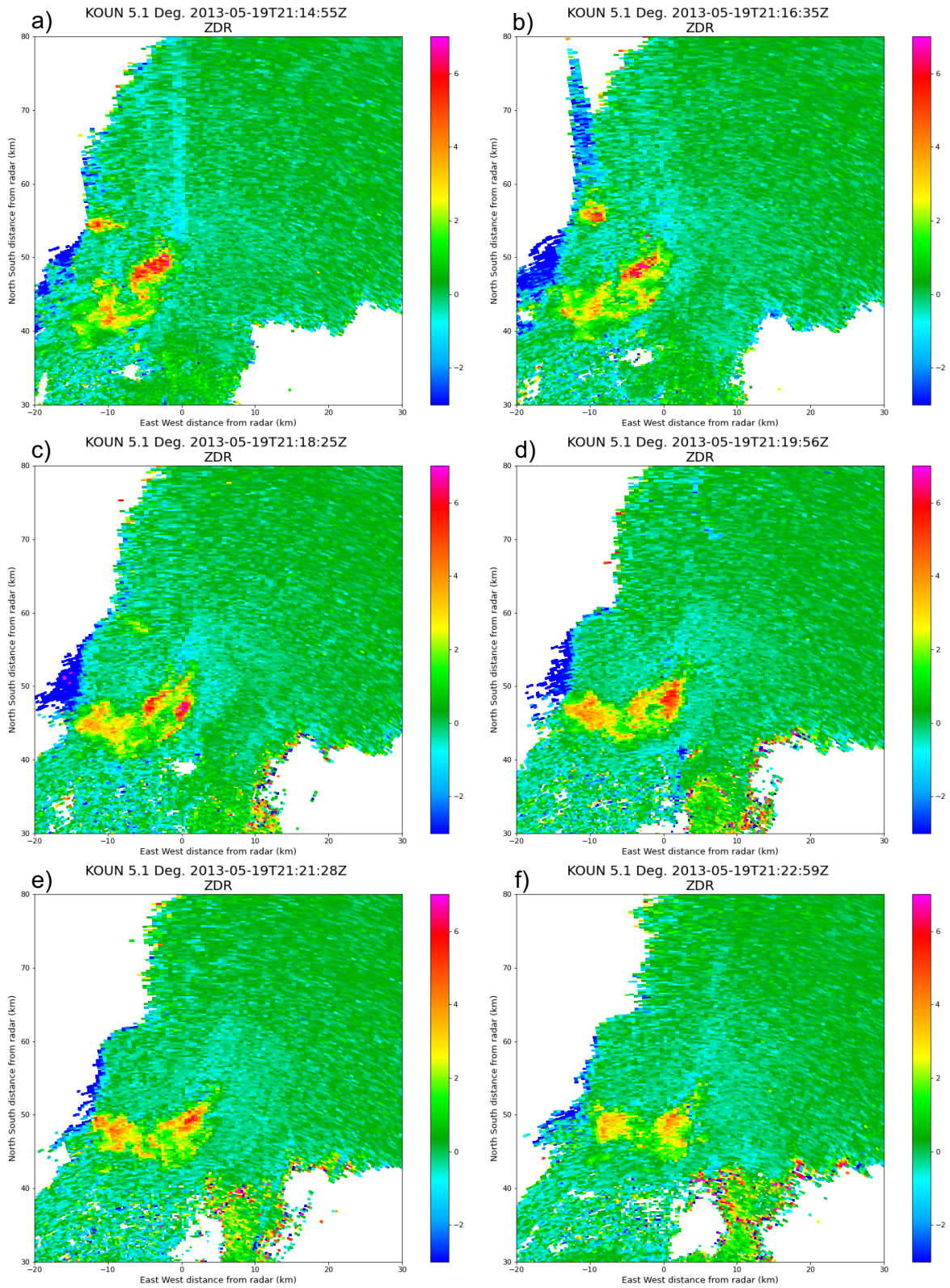
Figure 5.5: Same as Figure 5.4, but from 2114 – 2122 UTC.
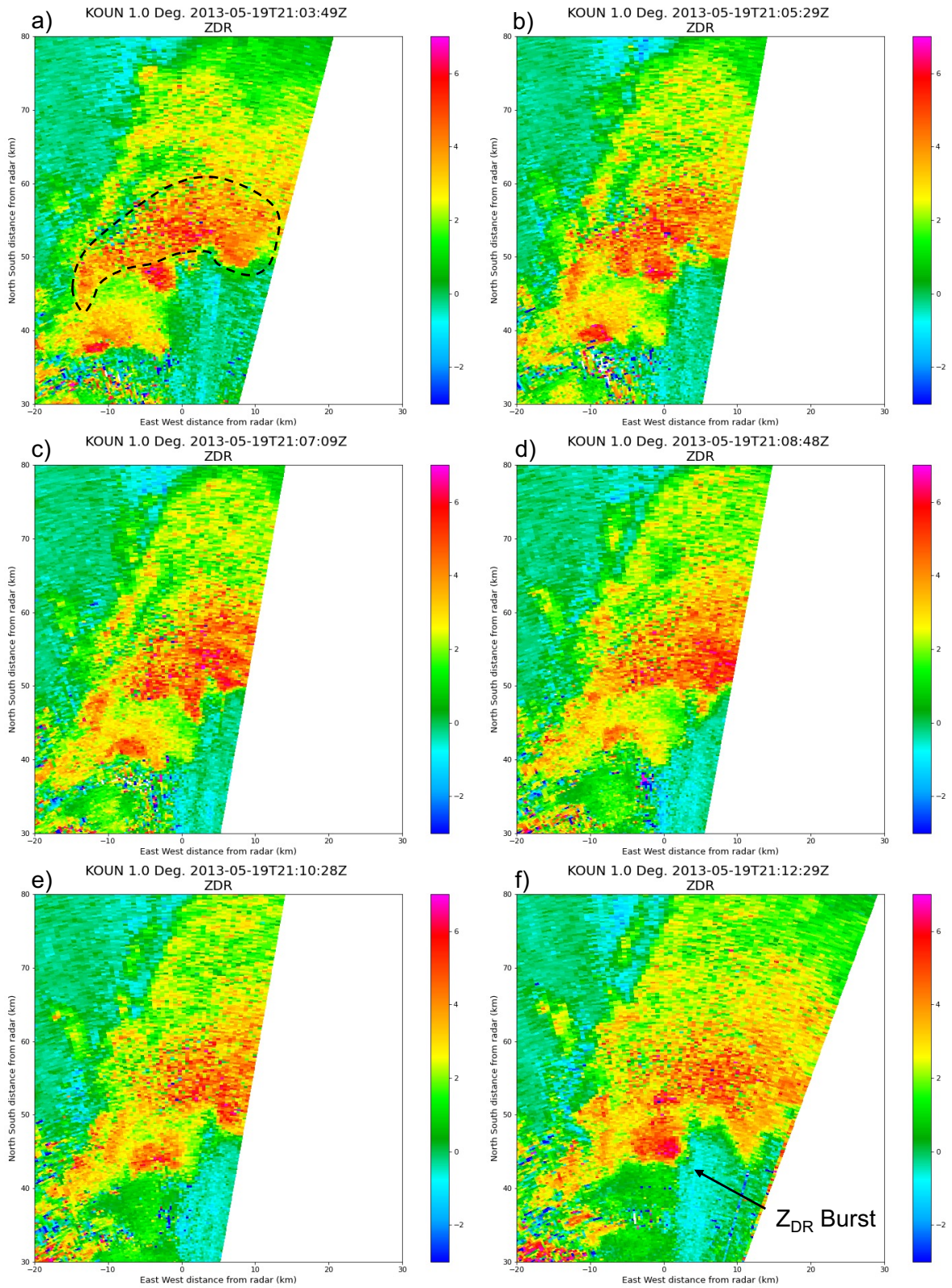
Figure 5.6: PPIs of the 1° elevation Z_{DR} on 19 May 2013 from 2103 – 2112 UTC near Edmond, OK. The dashed black line in panel a) gives the initial location of the Z_{DR} arc.

area of positive Z_{DR} returns lingered past this hail fallout disruption. Since the Z_{DR} arc was at low-levels, it may not serve as a strong pre-cursor signature to the hail fallout. However, as seen in studies such as Dawson et al. (2014), these modulations of the Z_{DR} arc, such as the Z_{DR} bursts that spread out with time can indicate size sorting and potentially an indication of a local period of enhanced hail melting. The temporary disruption of the Z_{DR} arc at 2120 UTC also matches Tanamachi and Heinselman (2016) as a signal of active hailfall at the surface, which based on MESH returns and storm reports is what occurred at this time.

Derived parameters also signaled upcoming hail fallout for this storm. The time evolution of the 50 and 60 dBZ echo tops compared to MESH are given in Figures 5.8 – 5.9, respectively. A local maximum in the 50-dBZ echo top of 8.92 km was present at 2107 UTC, with a local minimum of 8.27 km at 2114 UTC. In contrast, the local minimum in the 60 dBZ echo top of 6.89 km occurred at 2107 UTC, while the local maximum of 7.81 km occurred at 2115 UTC. The 50 dBZ echo top maxima and minima lagged behind the maxima and minima in MESH, whereas the 60 dBZ echo top minima lagged ahead of the minima in MESH, but stayed relatively consistent around the peak MESH time. In this case, however, echo tops do not appear to be a strong pre-cursor signature to hail fallout as the fluctuations in the echo tops are small comparatively to the fluctuations in MESH. This is likely because KOUN for this case did not top out the storms, leading to miscalculations in the echo tops. In fact, at the highest elevation angle (9.9°, >8.5 km AGL) the supercell still had Z_H >60 dBZ, thus making the echo tops for this case a null example of a pre-cursor signature. But, the general increase in echo tops with time as the storm intensified after 2140 UTC still can serve as a significant signal to storm intensity, but less so hail production.
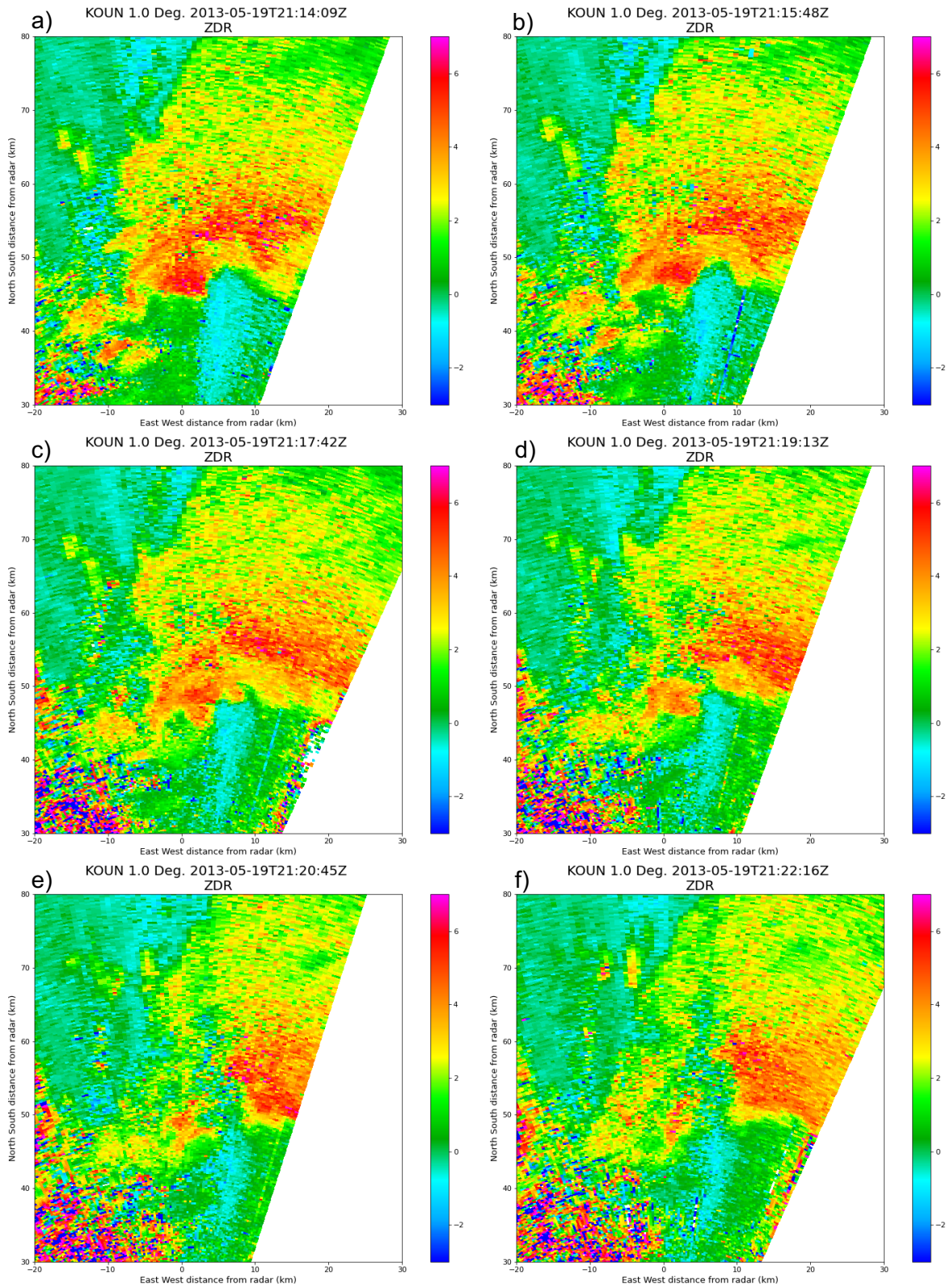
Figure 5.7: Same as Figure 5.6, but from 2114 – 2122 UTC.
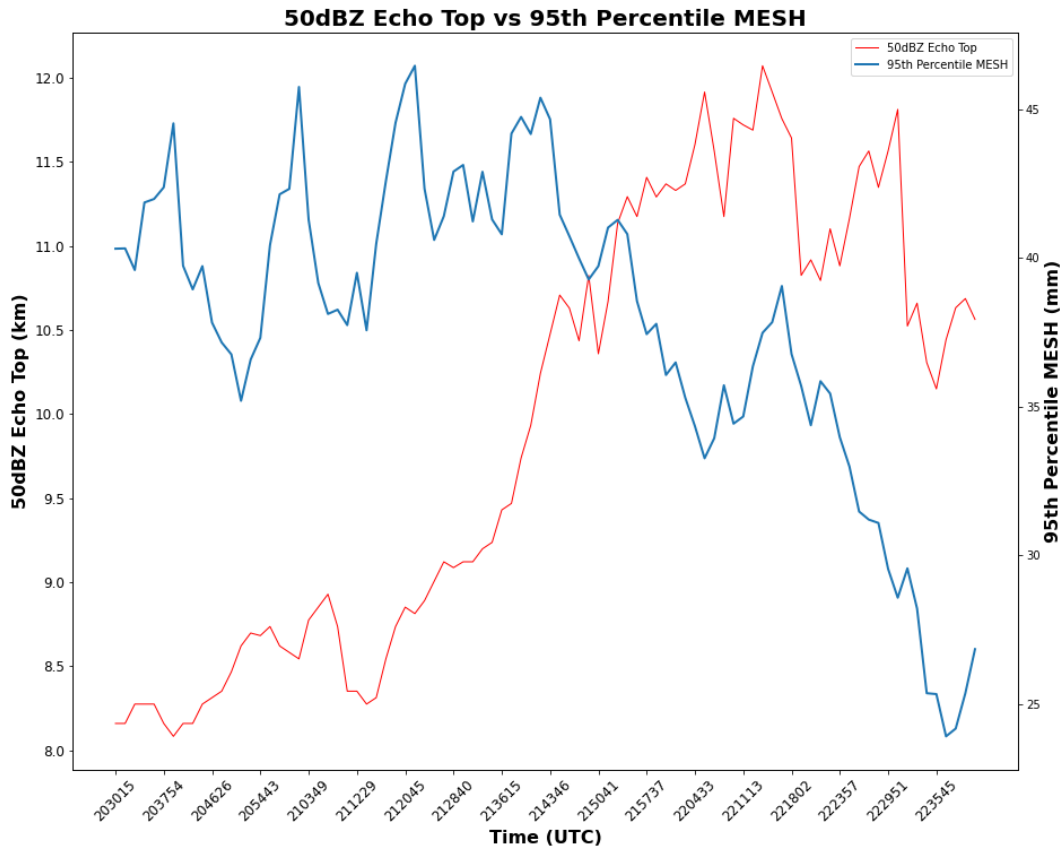
Figure 5.8: Time series of the 50 dBZ Echo Tops (red) vs the 95th percentile MESH (blue) for the Edmond-Carney supercell on 19 May 2013.

The time evolution of the hail core area using hail only and graupel and hail classes from the HCA are provided in Figures 5.10 – 5.11 respectively. Using hail only to determine the area gave a local maxima in the mid-levels from 2105 – 2112 UTC with a peak in the low - mid levels starting after 2112 UTC and continuing through the hail fallout time. Of note is that the mid-level peak in area occurred while MESH was declining, whereas the lower level area peak was coincident with the beginning of the increase in MESH returns. Utilizing the graupel classification with hail reveals the increase in area beginning at the end of the prior peak, at 2101 UTC. This peak in area continued through the hail fallout time, with a local maxima in the area descending towards the surface beginning at 2117 UTC. For the rest of this chapter, figures of

71

the hail core area prior to hail fallout will be used with both the hail and graupel classifications, as graupel at the mid-levels is assumed to contribute to hail production. This will result in a stark contrast in the magnitude of the hail core area below the environmental freezing level, but since we are looking at the HGZ region, will not be as impactful in analysis.
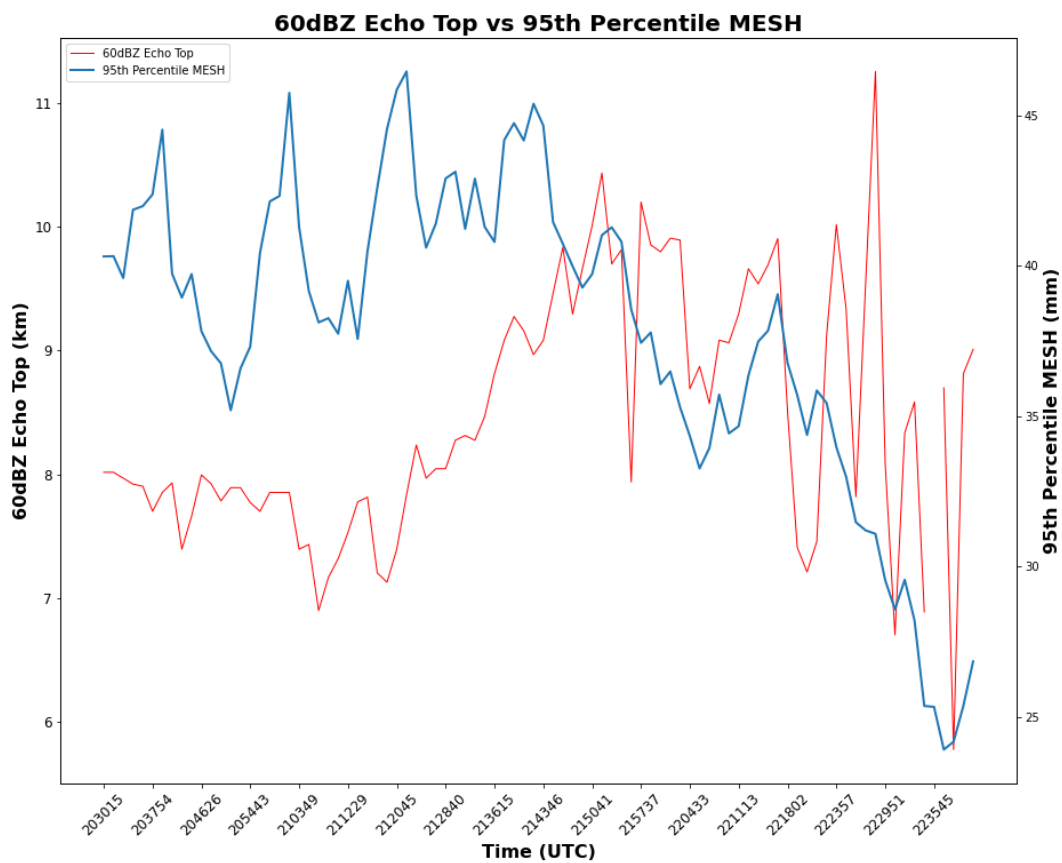
Figure 5.9: Time series of the 60 dBZ Echo Tops (red) vs the 95th percentile MESH (blue) for the Edmond-Carney supercell on 19 May 2013.
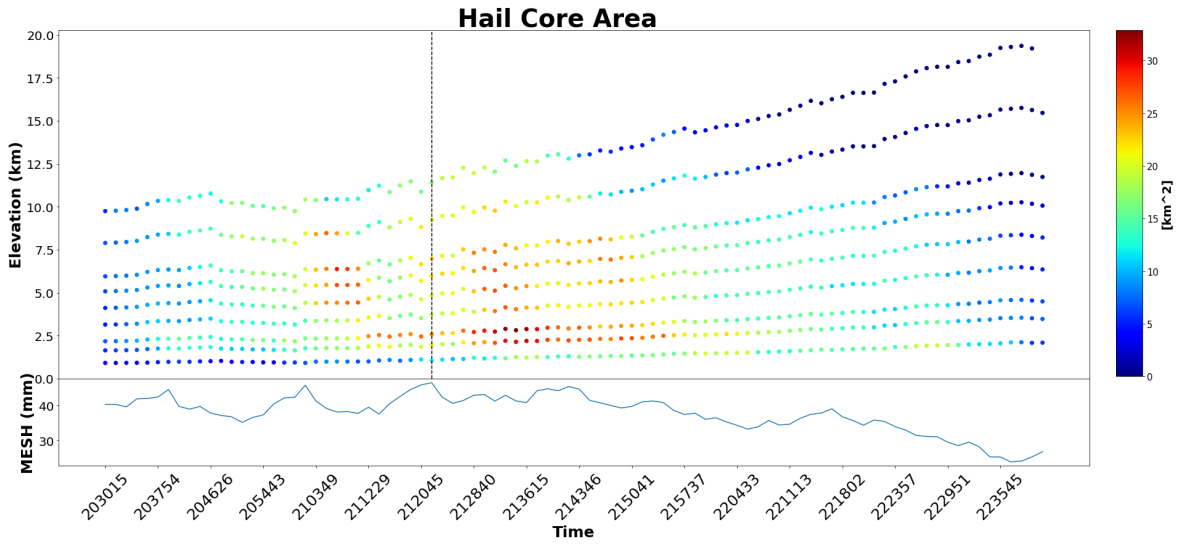
Figure 5.10: Time-height plot of the 95th percentile hail core area for hail only (top) and the time evolution of the 95th percentile MESH for the 19 May 2013 Edmond, OK supercell.
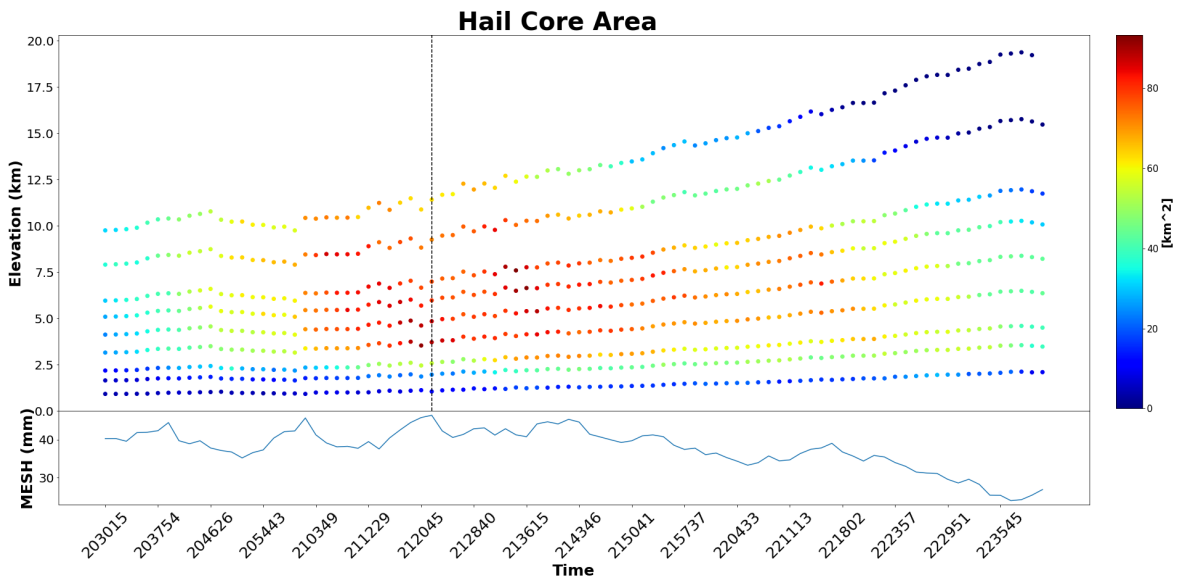
Figure 5.11: Time-height plot of the 95th percentile hail core area for the hail and graupel HCA classes (top) and the time evolution of the 95th percentile MESH for the 19 May 2013 Edmond, OK supercell.
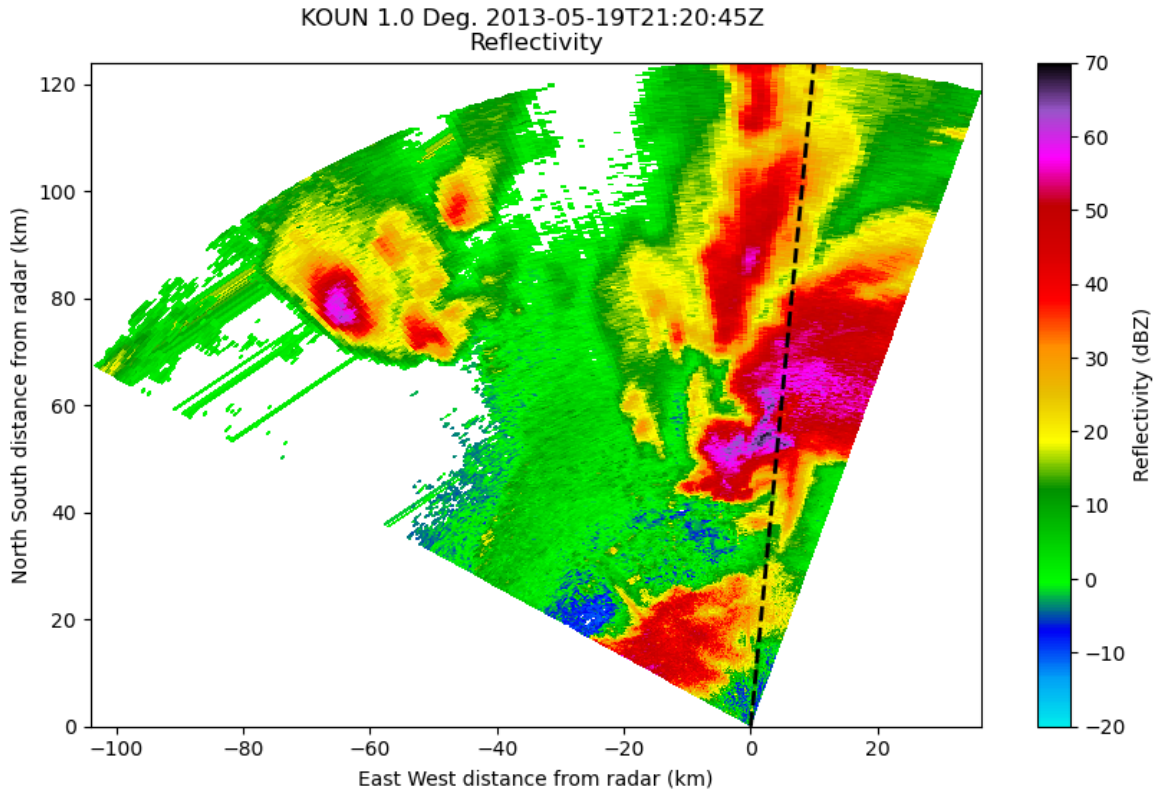
Figure 5.12: 1° PPI of Z_H at 2120 UTC on 19 May 2013 near Edmond, OK. The dashed black line indicates the location of the RHIs produced in Figures 5.13 – 5.14.

5.1.3 Hail Fallout

In a similar manner to the Hays, KS case observed by RaXPol, reconstructed RHIs provided observations of a hail fallout signature occurring with this storm, which is in line with the peak MESH time, as well as surface hail observations and reports. This time however, the hail fallout signature is best seen on the Z_H RHIs as a descending core of $Z_H > 60$ dBZ (Figure 5.13 – 5.14). This hail core descended at a rate of approximately 20 – 22 m s^{-1} (i.e., roughly 1" hail) and moved from a range of 45 km to 60 km during its roughly 5 min descent. The Z_H core remained relatively uniform, throughout its descent, with little change in the shape of the core. Z_H values increased to > 70 dBZ across a large swath of the core by 2120 UTC, at which point this core

was very near the surface. RHIs were produced along the 3.5° azimuth angle, indicated in Figure 5.12. Cross sections of this fallout signature are provided in Figures 5.13 – 5.14. Note that this fallout did traverse some across other azimuth angles, but plotting other azimuths (not shown) showed a similar trend as those presented in Figures 5.13 – 5.14.

Less microphysical processes, such as drop shedding, were able to be resolved with KOUN compared to RaXPol, but the dual-pol cross sections still provided some insight into the microphysics within this descending hail core. The ρ_{hv} field remained steady through 2117 UTC as the hail core began to descend. Z_{DR} within the hail core initially spanned from -1 – 0 dB and held relatively constant in magnitude at 2117 UTC. A surge of lower ρ_{hv} returns occurred at 2119 UTC, though this signature was located at a range of 50 km, while the hail core was centered at 55 – 60 km. This ρ_{hv} core was associated with a mixture of -1 – 0 dB returns, consistent with the Z_{DR} returns within the hail core. The ρ_{hv} core decreased in magnitude at 2120 UTC, with ρ_{hv} returns < 0.9, and remained offset from the descending hail core. Z_{DR} within the ρ_{hv} core began featuring positive Z_{DR} returns at this time, with a continued mixture of -1 – 0 dB returns within the descending Z_H core. The ρ_{hv} core decayed following the arrival of the Z_H core to the surface. Positive Z_{DR} persisted following the arrival of the Z_H core to the surface and followed a similar pattern to the ρ_{hv} core. In a similar manner to RaXPol, this feature could be associated with melting hailstones, as it was still located in a relatively high Z_H field and the separation from the strongest Z_H returns could be brought on by horizontal size sorting. Based on studies such as Dawson et al. (2014), this size sorting would place the largest hail sizes along the left size of the hail core in Figure 5.13, in which these larger hailstones could be impacting the reduction of ρ_{hv} and increase in Z_{DR} with time as well through active hail melt and drop shedding.
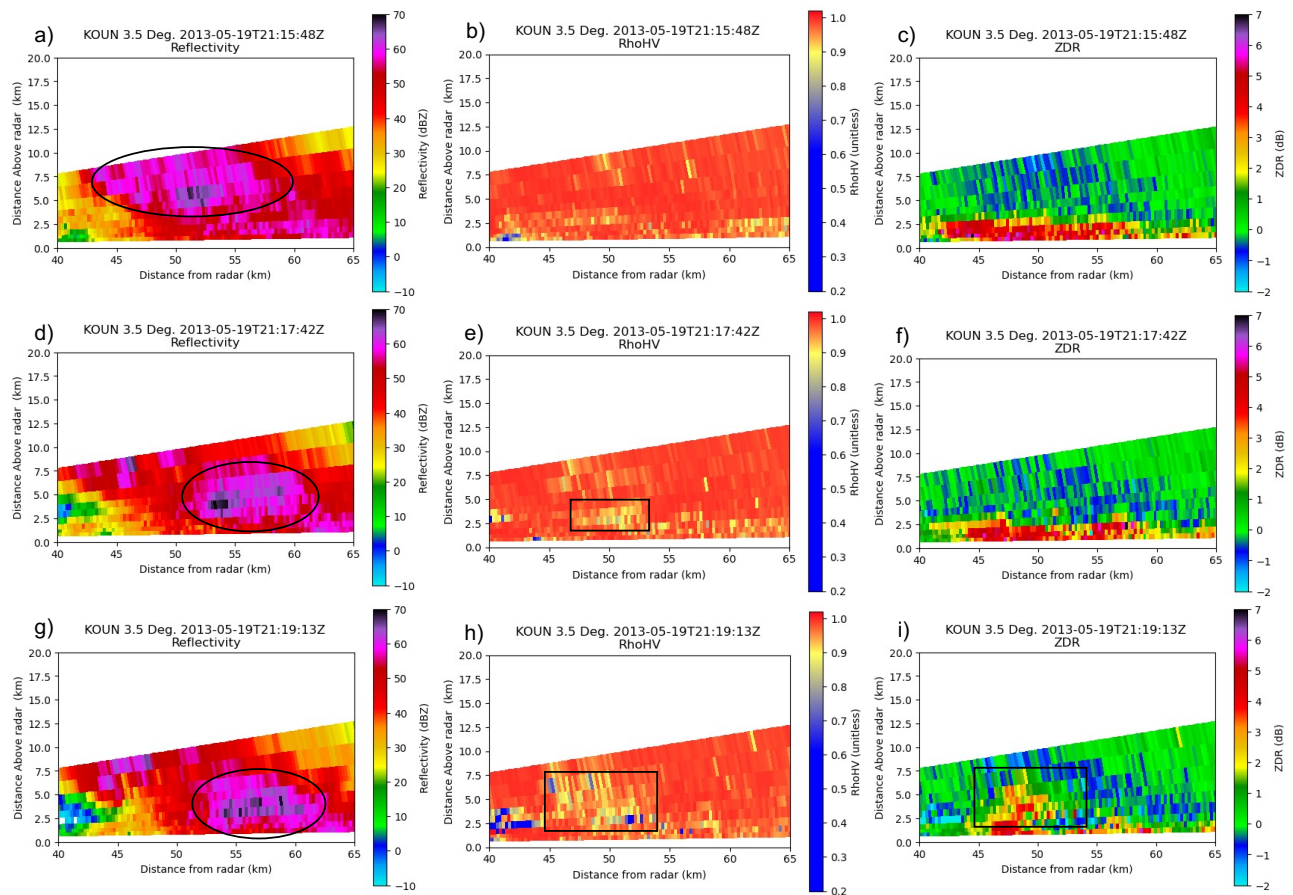
Figure 5.13: RHIs along the 3.5° azimuth angle from 19 May 2013 from 2115 – 2119 UTC for left) Z_H, middle) ρ_{hv}, and right) Z_{DR}. The black contour in the Z_H plots indicate the hail core and the black rectangles in ρ_{hv} and Z_{DR} indicate the location of the their respective cores, which are spatially offset from the largest Z_H returns.

This does match the observations as a 2.5" hail report was located at a lower range than this descending hail core was located at.

5.1.4 Cyclic Hail Production

The evolution of MESH from the Edmond-Carney supercell is provided in Figure 5.15. For this particular storm, the evolution of MESH featured a cyclic nature, in which there were semi-frequent peaks in the magnitude of MESH with time. In this case, these peaks occurred on the order of approximately 20 min, which matches prior
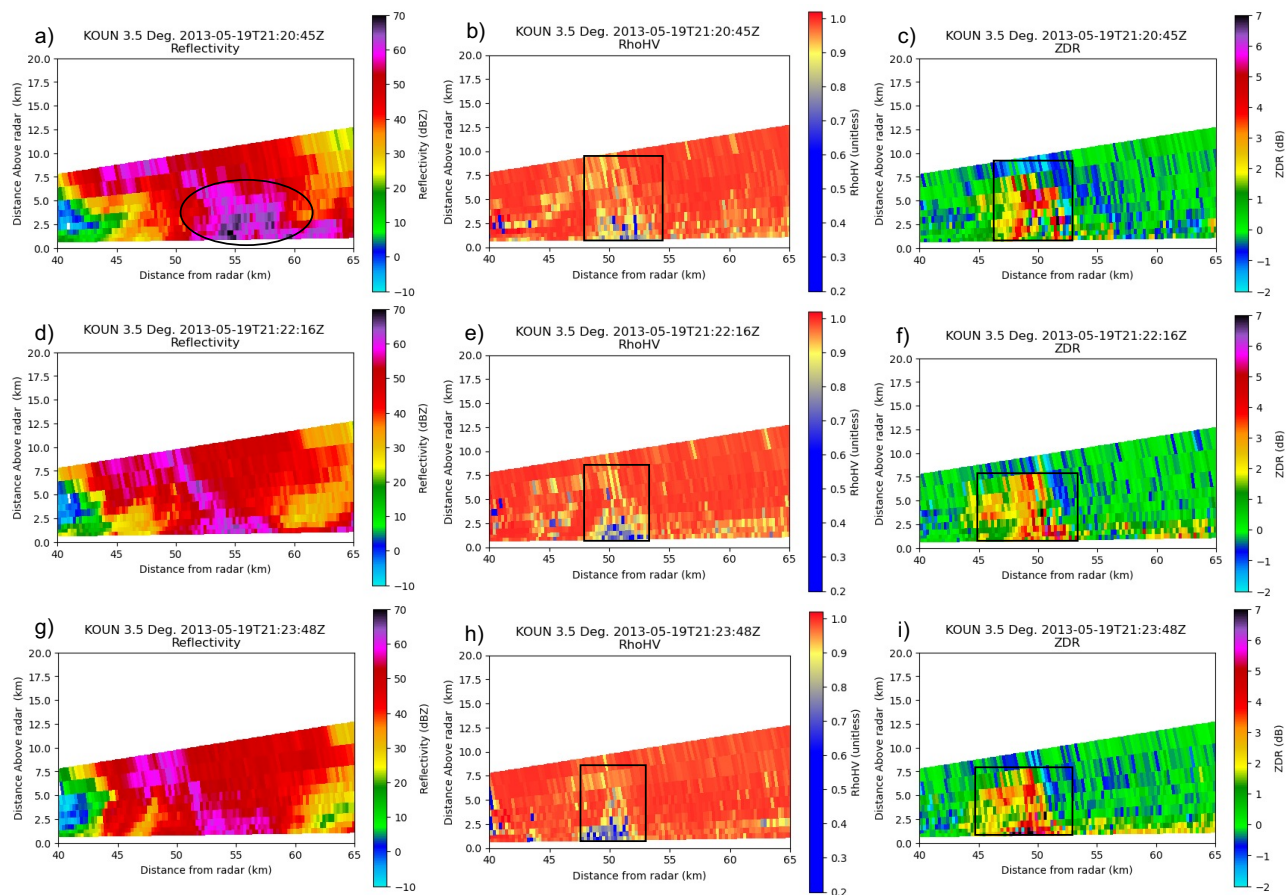
Figure 5.14: Same as Figure 5.13, but from 2120 – 2123 UTC. The black contour in panel a) represents the hail core as it reaches the surface and the rectangles in ρ_{hv} and Z_{DR} indicate the location of their respective cores.

studies such as Kumjian et al. (2021). Small scale oscillations in MESH values occurred between these peaks, and the peaks in MESH themselves were short lived, on the order of only a few minutes per peak.

For this storm, one key feature in the evolution of MESH stood out. Utilizing storm surveys and reports from the NWS and SPC yielded a connection between the MESH evolution in Figure 5.15 and tornado production, specifically the differences between tornadic and non-tornadic phases. The storm mode can be broken into three parts, which are defined in Table 5.1. The first time frame, or the non-tornadic period,
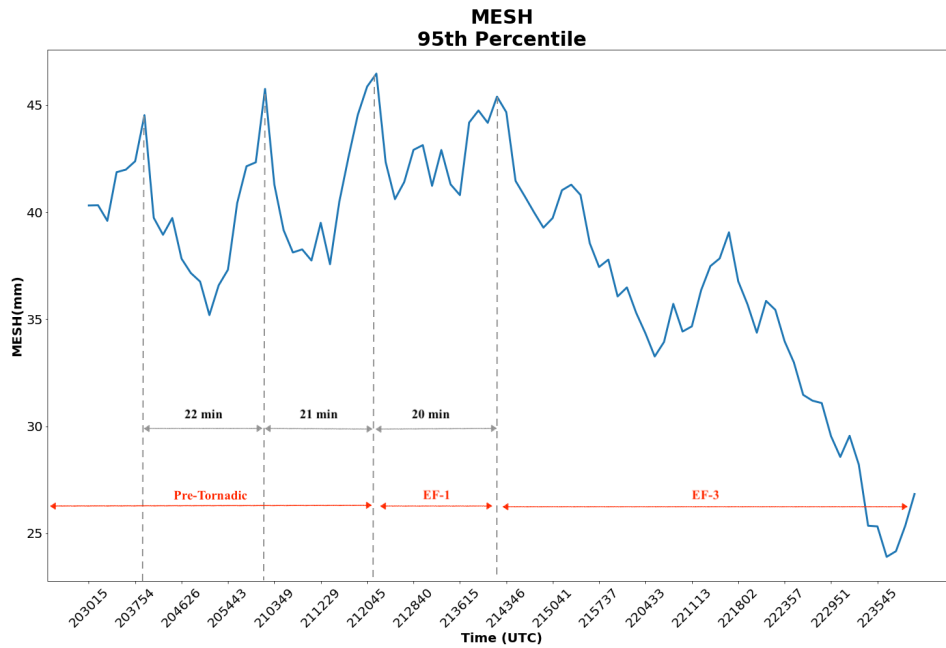
Figure 5.15: Time series of the 95th percentile MESH for the Edmond-Carney Supercell on 19 May 2013. The time between peaks is given in the black and the storms phase is given in red.

featured prominent cyclic hail production. MESH peaks were spread out roughly 20 min apart, with noticeable dips in the MESH values in between the peaks. The supercell phase changed at 1922 UTC, as it became tornadic, which was later rated as an EF-1. During the EF-1 phase, another hail cycle occurred, but compared to the non-tornadic period, the dip in MESH was less pronounced, as MESH values went from a peak near 45 mm to 42 mm, compared to a dip closer to 37 mm. 1941 UTC marked the transition into the third period, which featured the formation of an EF-3 tornadic supercell. This period brought the most stark contrast compared to the first two periods. Little to no cyclic hail production occurred during this time based on the MESH evolution. In fact, the MESH continually dropped following the formation of the EF-3 tornado,

Table 5.1: Breakdown of the storm phase and times associated with Figure 5.15 for the Edmond-Carney supercell.

#	Time (UTC)	Type
1	2030 − 2122	Non-Tornadic
2	2122 − 2141	EF-1 Tornadic
3	2141 − 2224	EF-3 Tornadic

going from 45 mm at the time of intensification to near 25 mm by the end of the time evolution.

This cyclic hail production has been noted before, such as in Kumjian et al. (2021), but an understanding of the causes of this cycling related to storm mode remains limited. It is possible that it the cyclic nature is tied to the structure and strength of the mesocyclone within the HGZ, but poor vertical resolution has been cited as a limiting factor in an observational understanding (Kumjian et al. 2010). It is possible then that a stronger tornado will increase the mesocyclone strength and can eject more growing hydrometeors, which can limit the appearance of the cyclic nature and result in the gradual reduction of MESH over time. But, it is also possible that this evolution is tied to the calculations of MESH and contamination from tornadic debris could bias the MESH values down with time. As such, more work needs to be done on this topic, especially in comparing environmental thermodynamics and kinematics with radar observations.

5.2   2017 Hail-Producing Storms

5.2.1   Storm Backgrounds

A compact shortwave trough and dryline promoted the risk for severe thunderstorms across central OK on 26 March 2017. The environmental setup was most favorable for

significant severe hail, which prompted a moderate (4/5) risk across central OK to be issued by the SPC at 13 UTC that persisted through the rest of the day (Figure 5.16). This moderate risk was associated with a 45% significant severe hail risk. Numerous >2" hailstones were produced this day as supercells, some tornadic, were produced across the region.

For this study, focus will be on the peak 95% MESH times of two supercells. The first was a supercell located near Seminole, OK that remained non-tornadic throughout the duration of its lifetime. The supercell split several times and at the peak 95% MESH time of 2238 UTC had split again, though the left-moving supercell rapidly decayed. This storm verified with 1" hail reported near Seminole. Analysis for this supercell will begin at 2322 UTC. The second was a supercell located near Wynnewood, OK that produced 2.25" hail. This storm was a long-track supercell that was predominately non-tornadic, but it produced a weak EF-0 tornado near Ada, OK at 0018 UTC. The 95% peak MESH time occurred at 0018 UTC, however, for this storm we will focus on the hail fallout that occurred at 2310 UTC due more notable hail signatures at this time. As such, focus on hail signatures will begin at 2250 UTC.

5.2.2   Seminole Supercell

One of the most notable pre-hail signatures for the Seminole supercell was a surge in the magnitude and area of Z_H across most elevation angles. Most notably, the early times of the analysis period featured an intensification of Z_H across all levels, coincident with the intensification of the storm as a whole. It was observed first at the mid to upper levels at 2316 UTC and was notable at the 0.9° elevation angle beginning at 2320 UTC (Figure 5.17). The storm then reached a quasi-steady state in Z_H, before
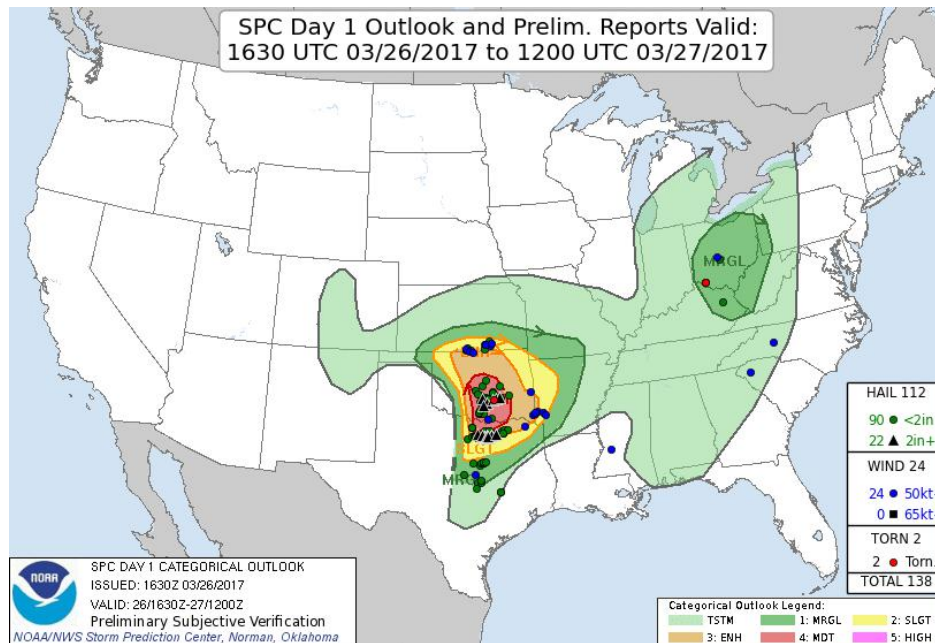
Figure 5.16: Storm Prediction Center Convective Outlook issued 1630 UTC on 26 March 2017 with the verified storm reports overlaid.

featuring another intensification in Z_H beginning at 2330 UTC across the mid-levels. This Z_H intensification then descended, approaching the 2.4° elevation angle at 2335 UTC and the 0.9° elevation angle starting at 2337 UTC (Figure 5.18 – 5.19). This surge in Z_H at the 0.9° elevation angle marked the arrival of the largest hail to the surface for this storm, based on the time evolution of MESH.

Changes in the structure of the mesocyclone also preceded the peak hailfall. For this case, focus will be on the 2.4° elevation angle as this provided the best PPI view of the mesocyclone. The mesocyclone started off broad and weak, but as the storm intensified in Z_H, the strength of the mesocyclone intensified as well. Beginning at 2328 UTC, however, the structure of the mesocyclone based on v_r changed as the mesocyclone began to contract in area (Figure 5.20). Following this contraction, the mesocyclone began to weaken, beginning at 2333 UTC, or 5 min before the peak hail fallout. This
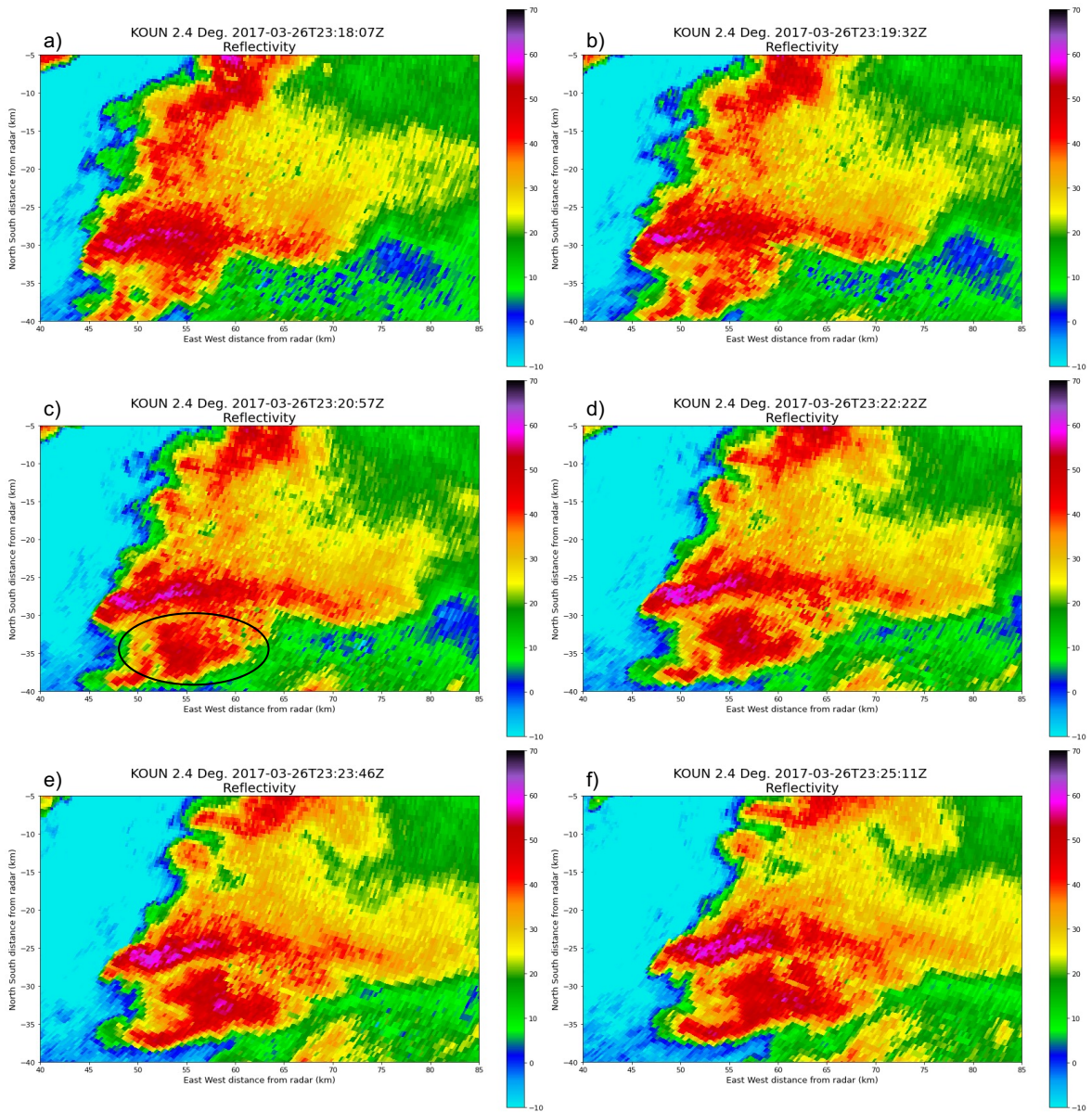
Figure 5.17: PPIs of Z_H along the 2.4° elevation angle on 26 March 2017 from 2318 – 2325 UTC near Seminole, OK. The black circle in panel c) indicates the location of the Z_H burst at the mid-levels.

gradual weakening persisted post-hailfall, which also led to a general weakening of the storm as a whole.

This storm also featured some other small scale changes prior to hail fallout, but for the sake of focusing on only the most notable, will only be discussed briefly here
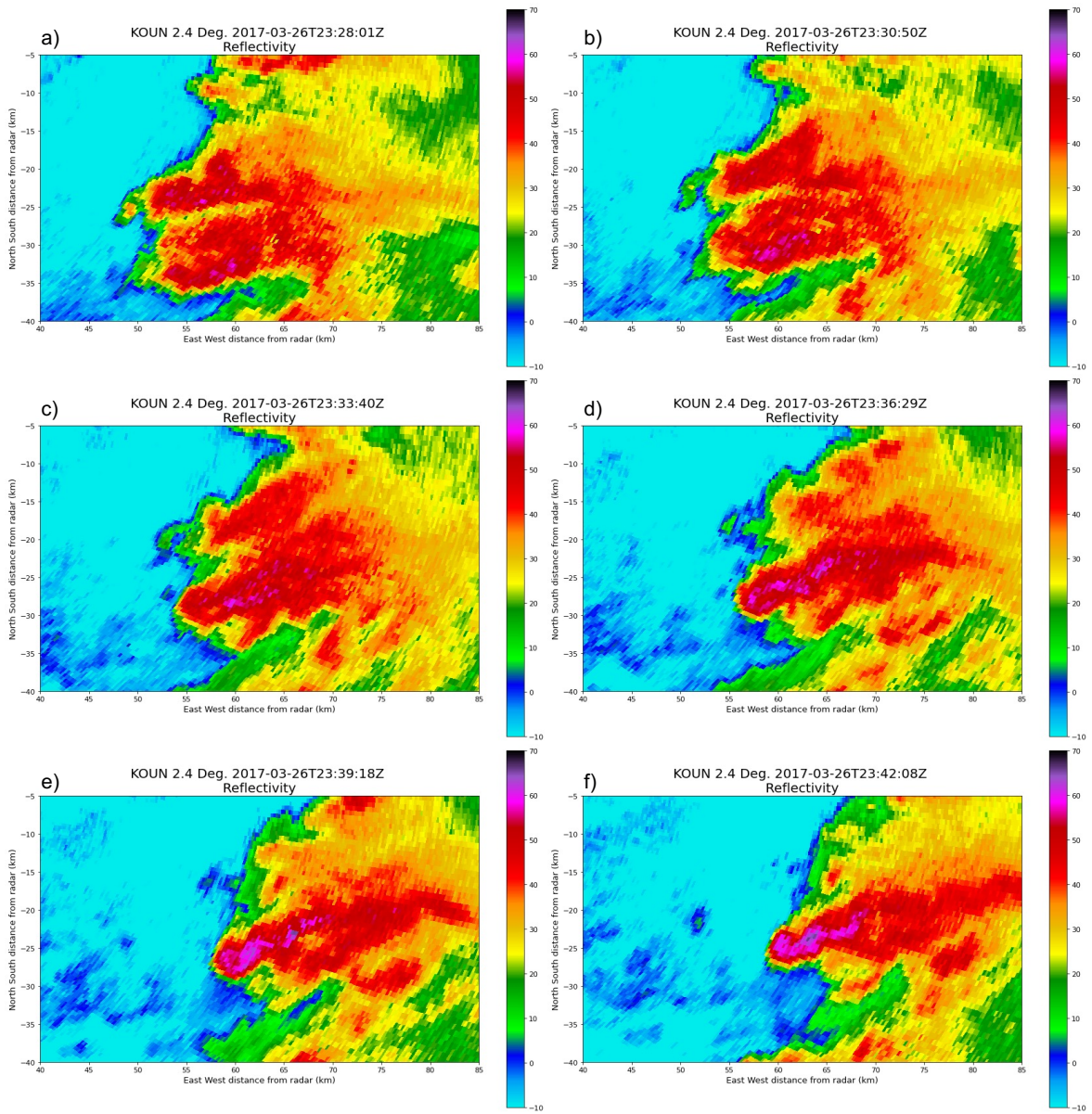
Figure 5.18: Same as Figure 5.17, but from 2328 – 2342 UTC.

and are not shown. One such example was a burst of Z_{DR} returns >0 dB that occurred at 2332 UTC on the 1.4° elevation angle, which was also observed at the 2.4° elevation angle at 2331 UTC. Additionally, similar to what was observed in the Edmond-Carney supercell, the mid-level development of sidelobe spikes occurred starting at 2331 UTC
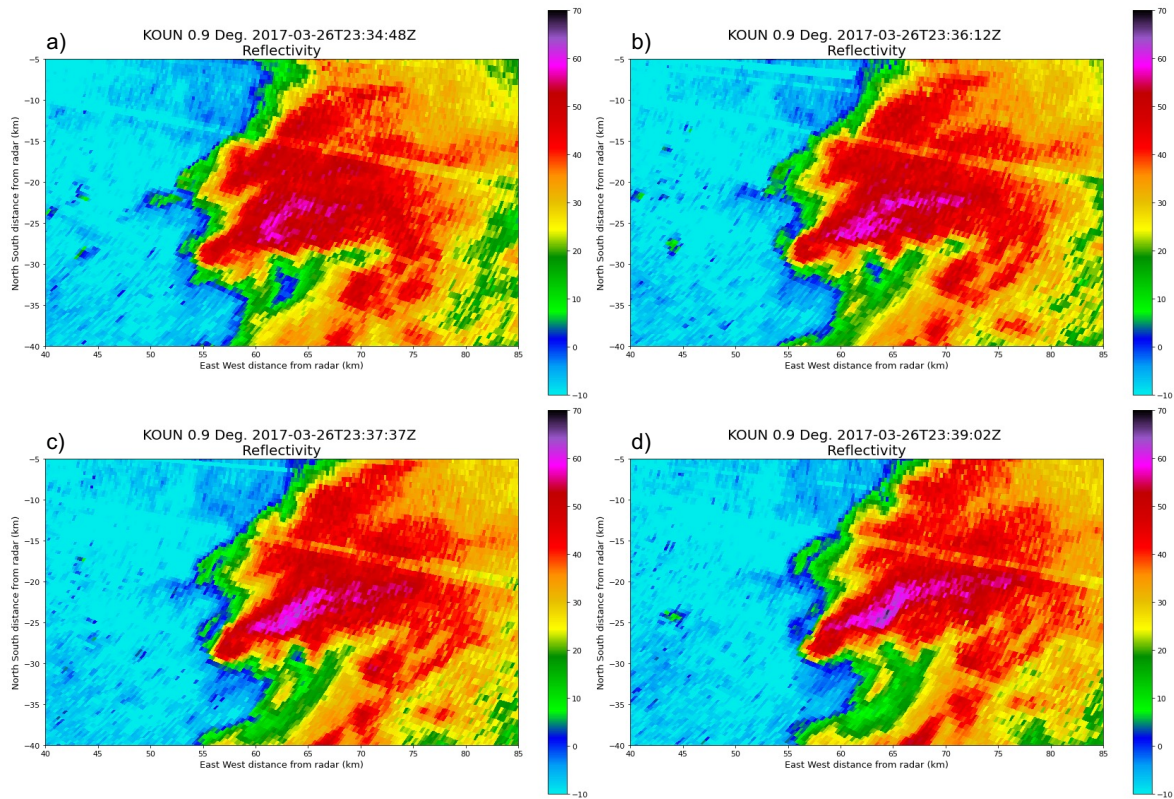
Figure 5.19: PPIs of Z_H along the 0.9° elevation angle on 26 March 2017 from 2334 – 2339 UTC near Seminole, OK.

along the 5.7° elevation angle and carried across all elevation angles, appearing on the 0.9° elevation angle at 2333 UTC.

The time evolution of the 50 and 60 dBZ echo tops compared with the time evolution of MESH are provided in Figure 5.21 – 5.22, respectively. The 50 dBZ echo top prior to the largest hail fallout had a local minima of 3.42 km at 2323 UTC, which was also associated with a local minima in MESH at 2330 UTC. A local maxima of 9.47 km in the 50 dBZ echo top occurred at 2334 UTC, 4 min before the peak MESH time at 2338 UTC. The 60 dBZ echo top had some lapses in magnitude during the storm's lifetime partly due to the shallow nature of the storm and its closer proximity to KOUN. But, the time evolution provided in Figure 5.22 still reveals a local minima of 5.58 km at
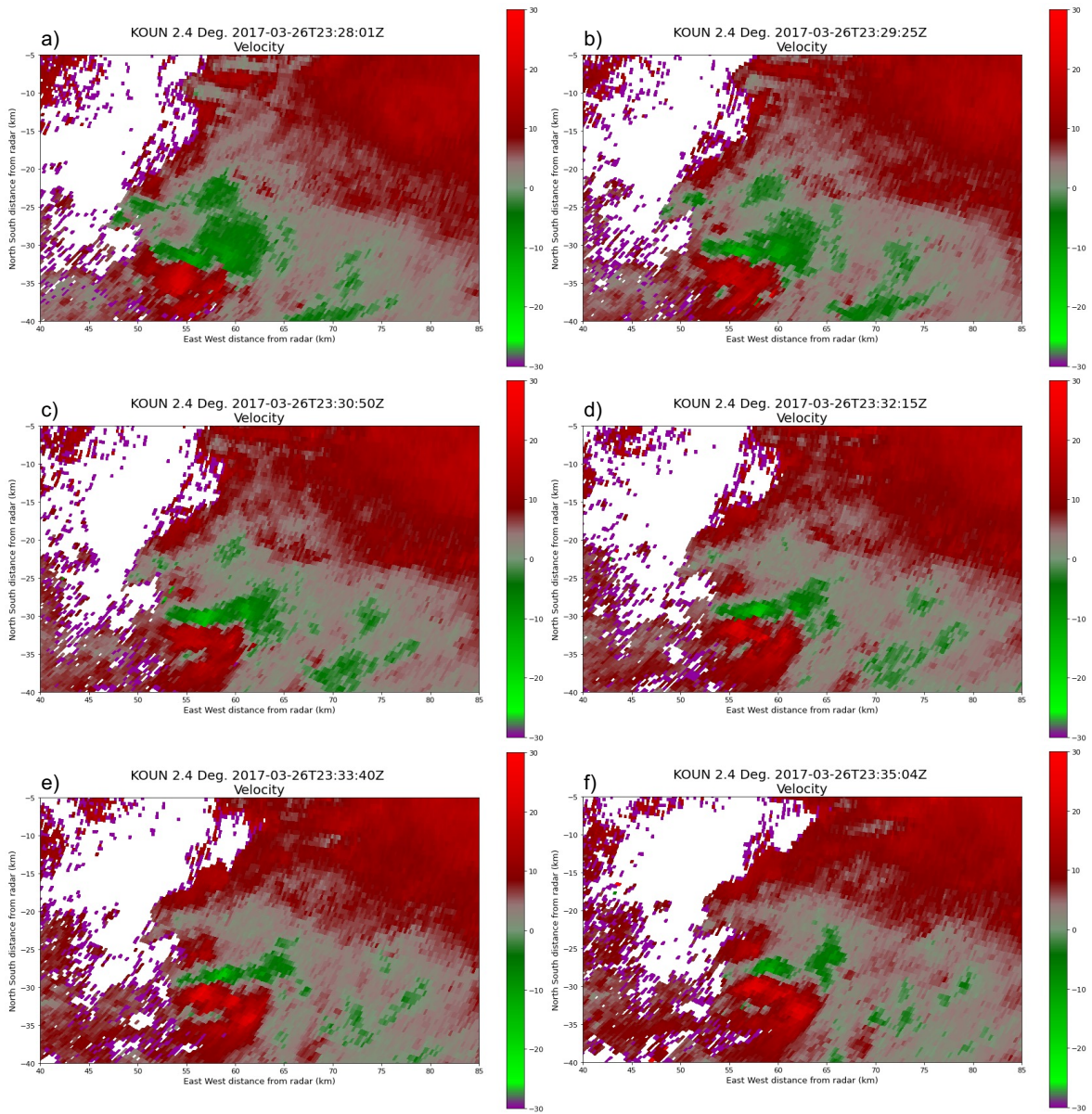
Figure 5.20: PPIs of v_r along the 2.4° elevation angle on 26 March 2016 from 2328 – 2335 UTC near Seminole, OK.

2330 UTC and a local maxima of 8.39 km at 2340 UTC. However, in a similar manner to the Edmond-Carney supercell, the relationship between the echo tops and MESH do not appear to have a robust relationship, but in this case KOUN did top out the storm but a 3 km height gap in data between elevation angles may have again, led to a miscalculation. In addition, prior to hail fallout for the Seminole supercell, a peak
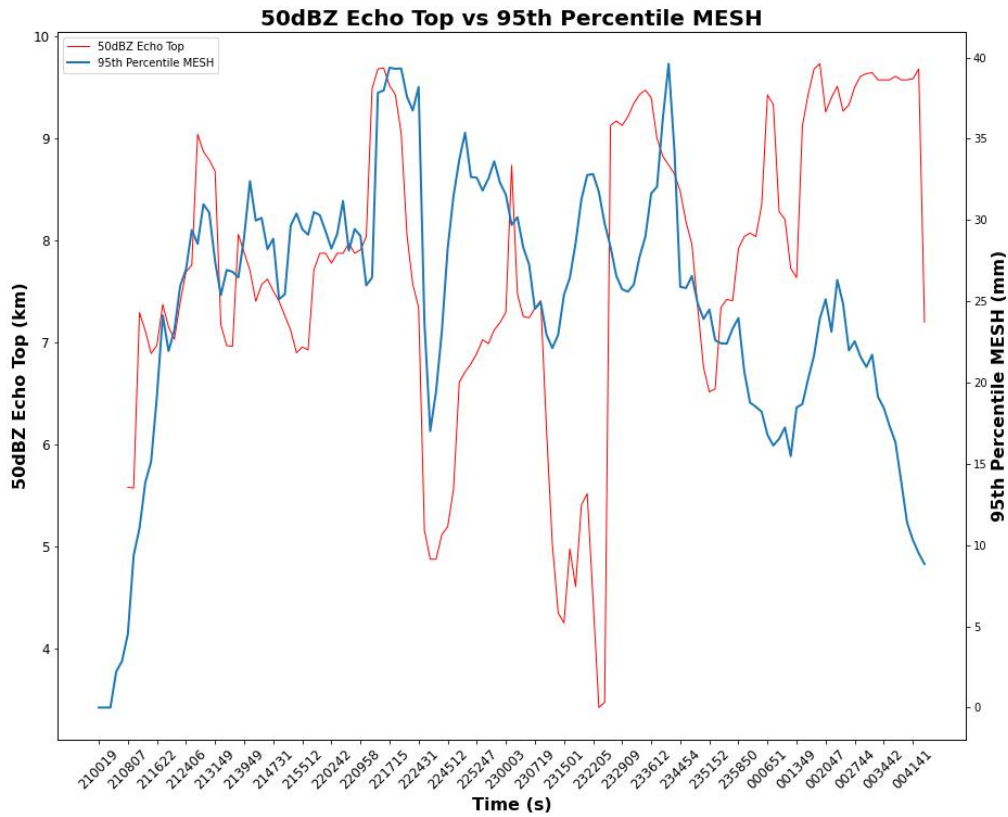
Figure 5.21: Time series of the 50 dBZ echo tops (red) and the 95th percentile MESH (blue) for the Seminole, OK supercell on 26 March 2017.

in the hail core area using the graupel and hail classifications was observed beginning at the mid-levels (Figure 5.23). This area started to increase approximately 10 min prior to the largest hail fallout and began after a local minima in the area at the prior MESH peak. This area also appears to have a descending nature to it, as the peak values move downward in height with increasing time (i.e., the slope is negative), with this descent approaching the low-levels about 5 min prior to the peak hailfall.

The time evolution of the 95th percentile MESH for the Seminole supercell is provided in Figure 5.24. Of note is first that there no available data across all elevation
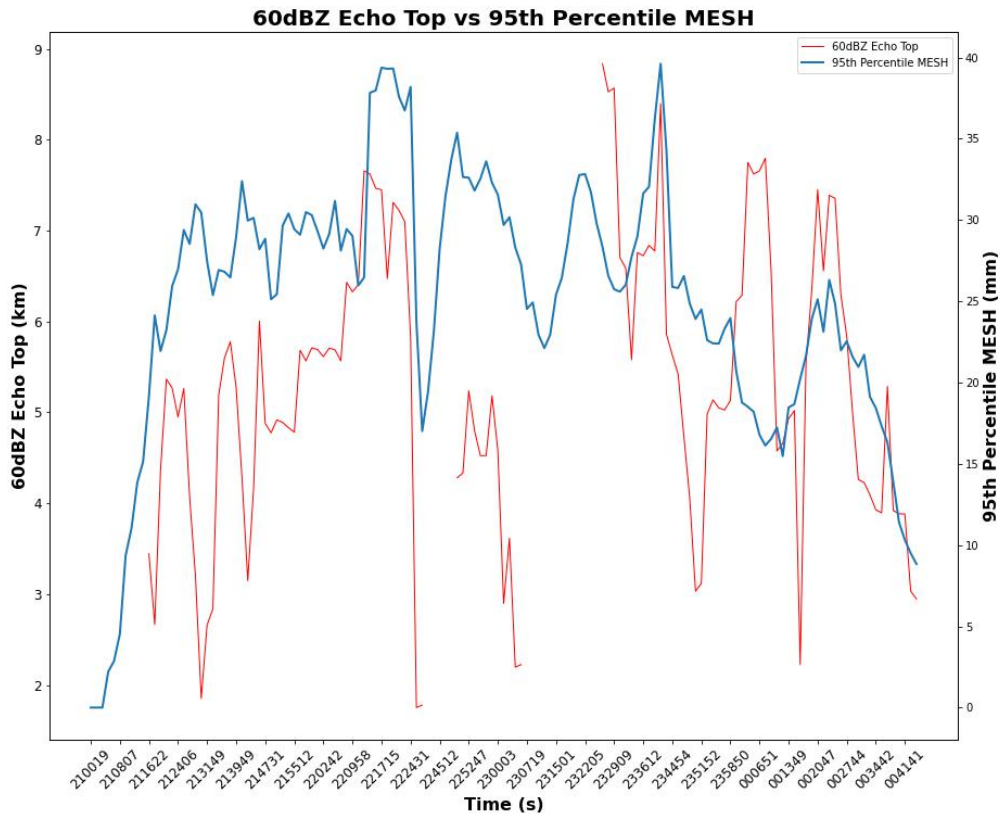
Figure 5.22: Time series of the 60 dBZ echo tops (red) and the 95th percentile MESH (blue) for the Seminole, OK supercell on 26 March 2017.

angles from 2226 – 2244 UTC, causing a sizeable drop in MESH as a result. Why the lapse in data exists is presently unknown. Second, the large increase in MESH at the beginning of the time series is a result of the initial formation of the storm as KOUN was able to capture the CI and early stages of this supercell. The storm in the later stages displayed a cyclic nature, primarily beginning after the data gap at 2244 UTC. In this case, the timing between peaks was on the order of 20 min, though the last peak was separated by closer to 40 min. This cyclic nature at the storms peak maturity is
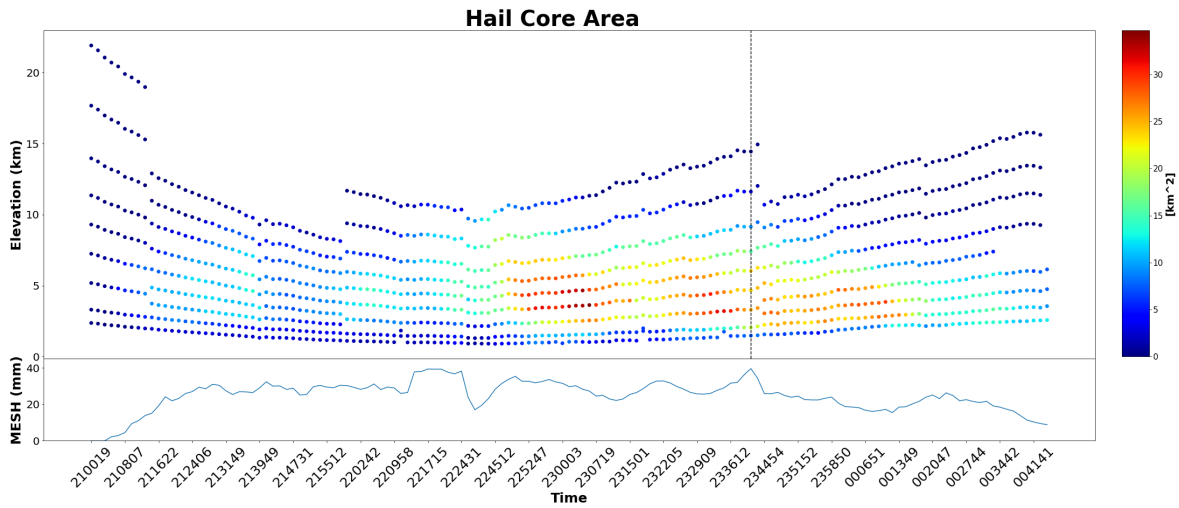
Figure 5.23: Time-Height plot of the hail core area (top) compared to the 95th percentile MESH (bottom) for the 26 March 2017 Seminole, OK supercell. The black line in the time-height plot indicates the peak MESH time.
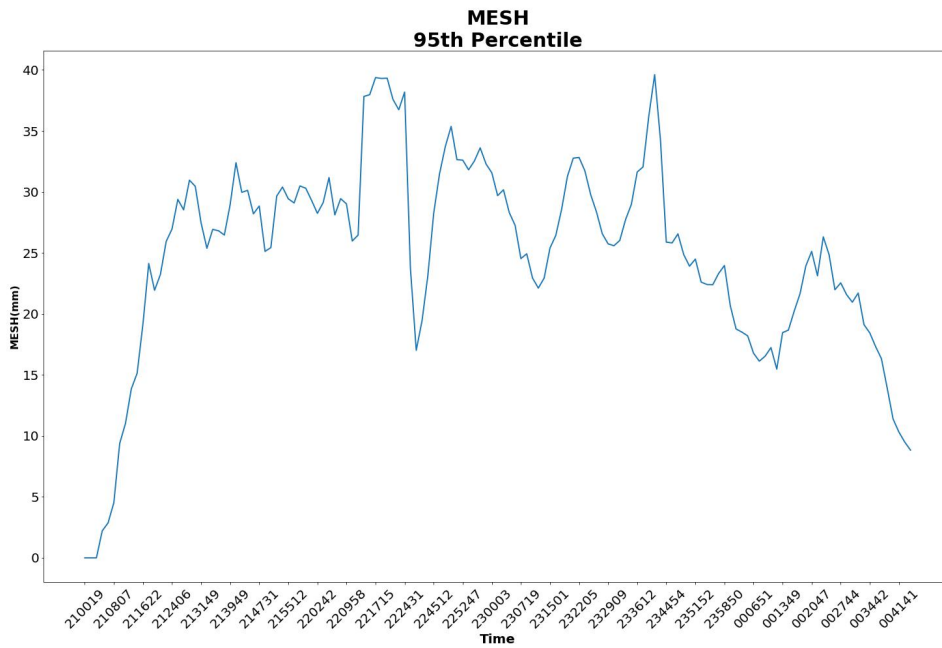
Figure 5.24: Time evolution of the 95th percentile MESH for the Seminole hail-producing supercell on 26 March 2017.

also evident in Figure 5.23 as there is a local minima between the increase in area for

this hail fallout time and another peak hail fallout that occurred near 2305 UTC.

5.2.3   Wynnewood Supercell

One of the most notable rapidly-evolving features from this supercell was the TBSS that occurred at the hail fallout time. This TBSS was first observed at 2300 UTC at the 4.6° elevation angle and with time was seen at progressively lower elevation angles (Table 5.2). What stood out most from the time evolution of this TBSS, however, was the emergence and evolution of a dual-TBSS followed by a single TBSS at the following update time. This single TBSS was positioned between the dual-TBSS as well. This dual-TBSS was best seen at the lower elevation angles, in particular 2.4°, 1.4° and 0.9°. Like the TBSS that developed aloft at 4.6°, the dual-TBSS that was evident at the lower-levels was able to be observed descending towards the surface, which is best shown when comparing PPIs of the 2.4° and 0.9° elevation angle, shown in Figures 5.25 and 5.27. A small secondary TBSS appeared at 2.4° elevation at 2304 UTC and appeared at the 0.9° elevation angle by 2305 UTC. The singular TBSS then appeared at 2.4° by 2306 UTC and again at 0.9° at 2307 UTC. The evolution of the 1.4° TBSS roughly paralleled the 0.9° elevation angle which could be due to their close proximity with height (Figure 5.26). But, using the comparisions of 2.4° and 0.9° supports the notion that this TBSS descended with time, which concurrently undergoing microphysical changes.

The descent of the TBSS served as a precursor to hail at the surface and the TBSS at 0.9° served as the hail fallout at the peak MESH time at 2310 UTC. This is because the evolution of the TBSS across all elevation angles reveals a descending nature to it, especially when looking at the evolution of the dual-TBSS and the single, elongated TBSS that occurred after the dual-TBSS. These two features highlight a change in the hail core, from two distinct cores to a single core that was centered between the two
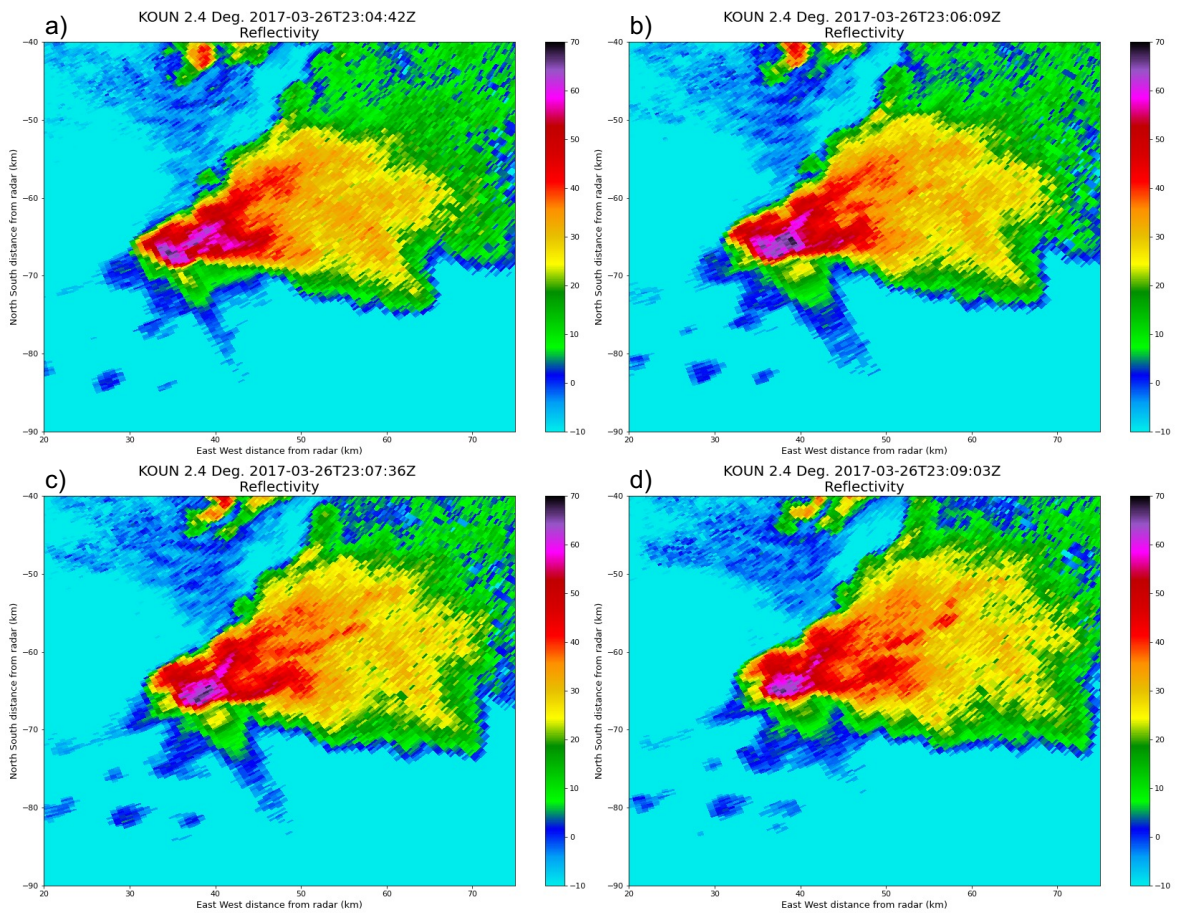
Figure 5.25: PPIs of Z_H along the 2.4° elevation angle on 26 March 2017 from 2304 – 2308 UTC near Wynnewood, OK.

separate cores. While a conventional NEXRAD radar may capture the appearance of the TBSS due to its longer lived nature, these changes such as the merging of hail cores may only be captured as a result of the rapid-scanning capabilities of KOUN. Additionally, the descent and eventual collapse of the TBSS occurred within a time frame less than 5–7 min, thus making this hail fallout another rapidly evolving signature relevant to hail observations.

The time evolution of MESH for the Wynnewood supercell is given in Figure 5.28, which includes the time of tornadogenesis at 0018 UTC. This supercell displayed pre-tornadic cyclic hail production, similar to the Edmond supercell outlined in Chapter
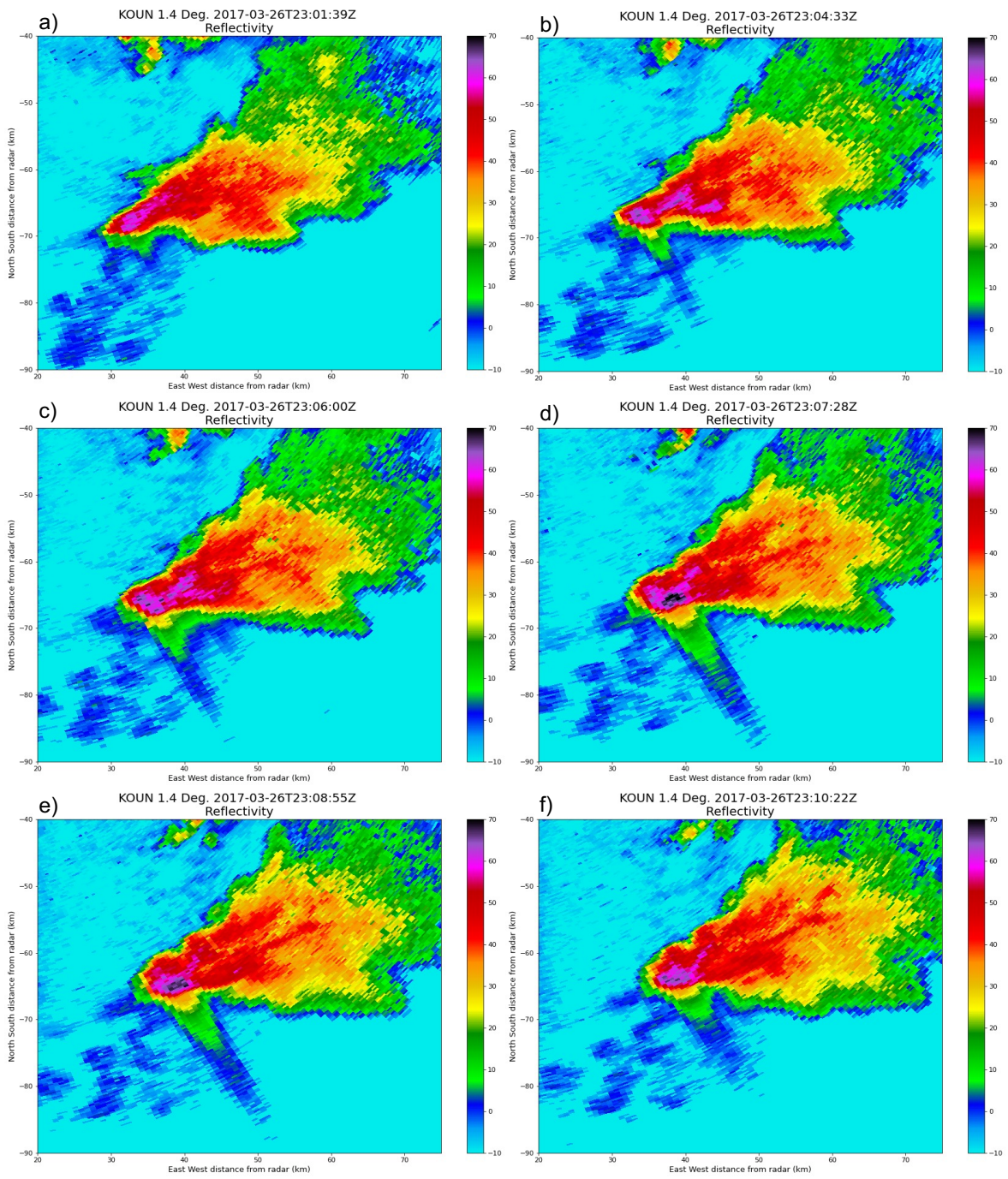
Figure 5.26: PPIs of Z_H along the 1.4° elevation angle on 26 March 2017 from 2301 – 2310 UTC near Wynnewood, OK.
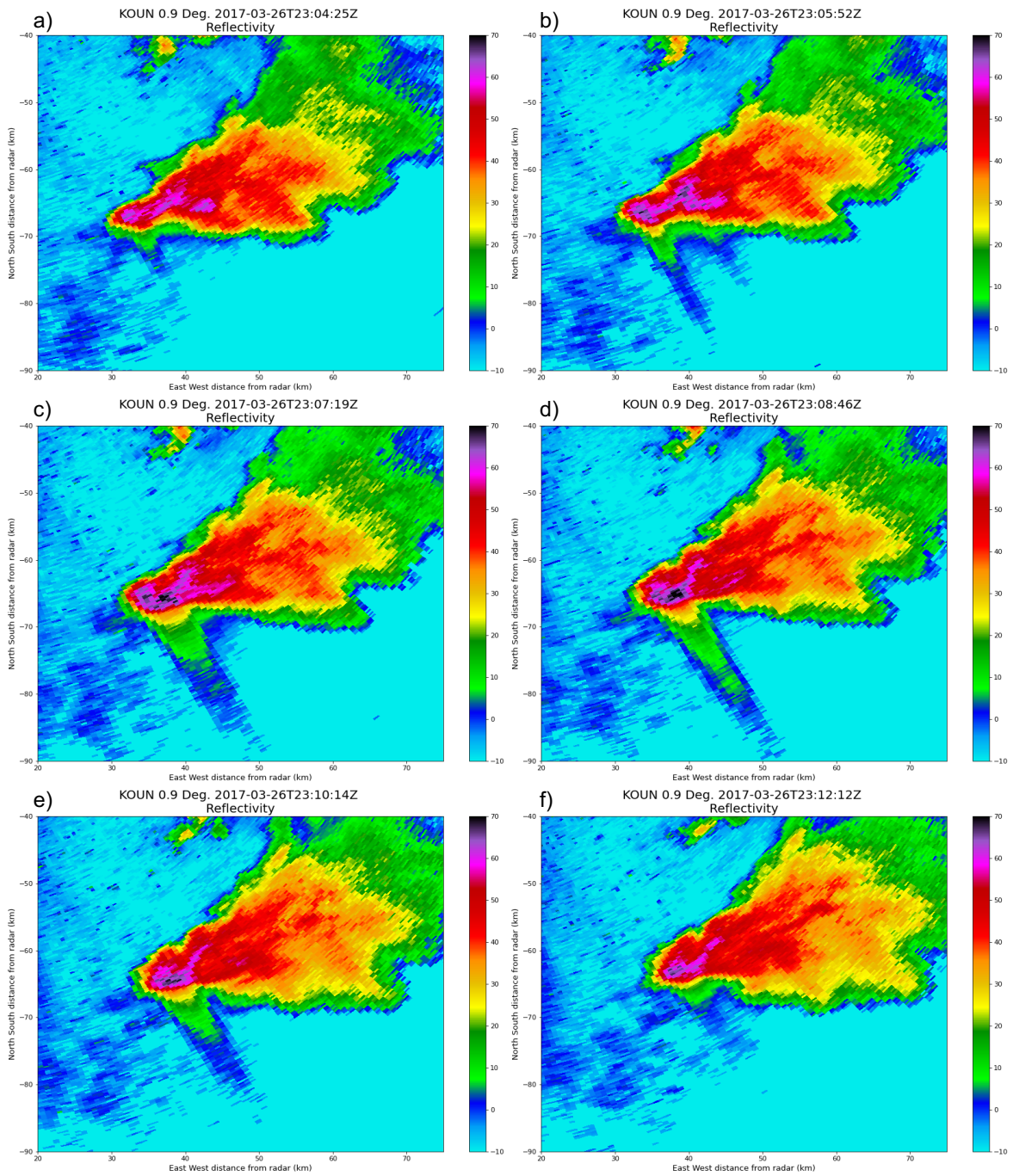
Figure 5.27: PPIs of Z_H along the 0.9° elevation angle on 26 March 2017 from 2304 – 2312 UTC near Wynnewood, OK.

Table 5.2: Summary of the Wynnewood, OK TBSS on 26 March 2017 across elevation angles.

Elevation Angle	Height (AGL)	Start Time (UTC)	End Time (UTC)
4.5°	7.5-km	2300	2308
3.5°	5.8-km	2301	2308
2.4°	4.0-km	2303	2309
1.4°	2.6-km	2301	2315
0.9°	1.9-km	2301	2315

5.1.4. In this case, however, the time between peaks was on the order of 30 – 45 min and the highest peaks featured a local, weaker, secondary peak immediately preceding the peak MESH time, on the order of ∼10 min. This secondary peak not only occurred for the peak MESH time, but for the peak MESH time observed at 2310 UTC, which was the time that featured the descending TBSS. After tornadogenesis at 0018 UTC, MESH continually dropped in magnitude, without displaying much cyclic nature to it, though this tornado was weak and short-lived (∼10 min), so it is unclear if this was simply part of the broad cyclic hail production of the storm.
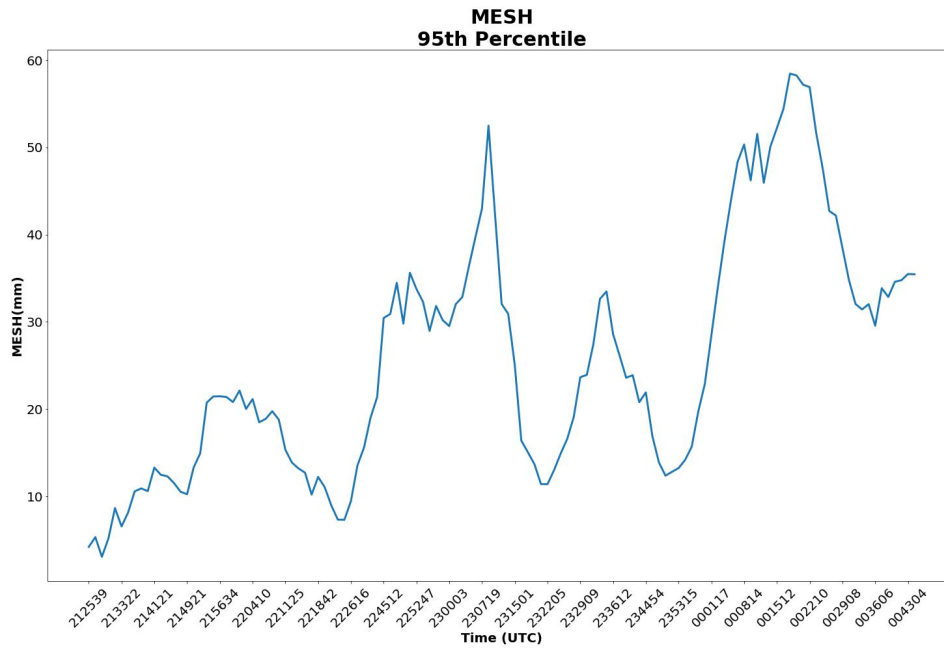
Figure 5.28: Time evolution of the 95$^{\text{th}}$ percentile MESH for the Wynnewood hail-producing supercell on 26 March 2017.

5.3 2016 Katie, OK Supercell

5.3.1 Storm Background

A shortwave trough along with a dryline resulted in the chance for severe thunderstorms on 9 May 2016. An enhanced (3/5) risk for severe storms was issued across central and eastern OK by the SPC at 1630 UTC (Figure 5.29). The primary threats included a 30% chance for significant severe hail along with a 10% for signficant tornadoes. Numerous supercells, along with multiple tornadoes, were produced across the region, primarily in central OK.

One supercell in particular was a strong long-lived storm that produced the EF-4 tornado in Katie, OK. National Weather Service storm reports noted that this tornadic supercell cycled down momentarily multiple times during its lifetime. One such cycle
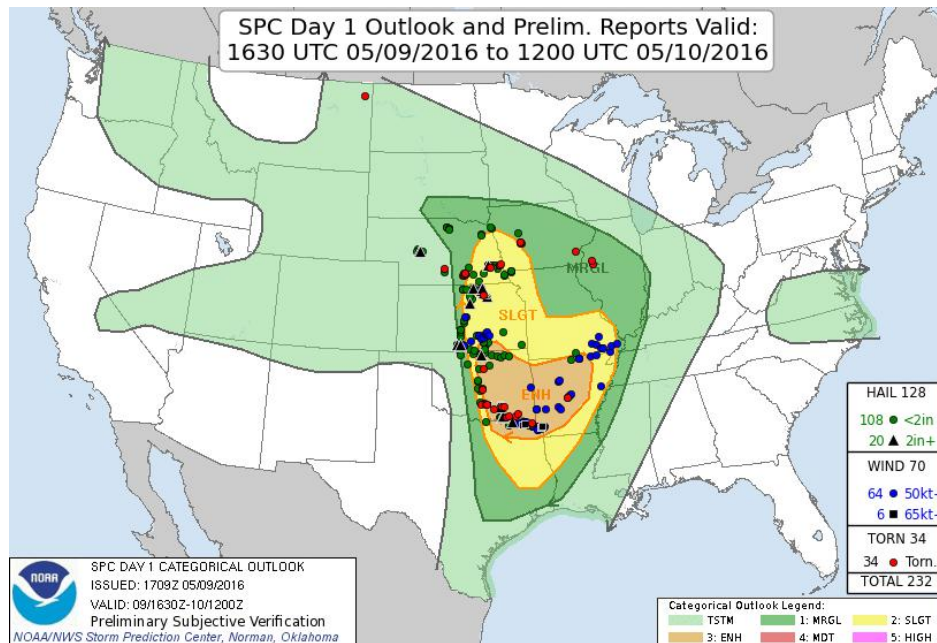
Figure 5.29: Storm Prediction Center Convective Outlook issued 1630 UTC on 9 May 2016 with the verified storm reports overlaid.

resulted in a 1.75" hail report at 2135. The peak 95th percentile MESH reflected this as the peak hail time occurred from 2139 – 2145 UTC. As such, focus for this storm analysis will begin around 2120 UTC.

5.3.2 Pre-Hail Signatures

Like has been observed with other supercells, one of the pre hailfall signatures present at the mid-levels includes the TBSS and sidelobe spikes. The sidelobe spikes were observed beginning at 2124 UTC in the upper levels of the storm, at the 9.1° and 7.1° elevation angles and traversed other elevation angles throughout much of the pre- and post-hail time period. The TBSS was evident at these same upper-levels, but was best observed in the mid-levels of the supercell. If using the 3.5° elevation angle as a proxy for the mid-levels, the sidelobes appeared beginning at 2128 UTC, with the development of the TBSS 11 min later, at 2139 UTC, or only 5 min before the

peak hail fallout (Figure 5.30 – 5.31). This TBSS extended radially outward at 2142 UTC before starting to decay at 2143 UTC, and was gone by 2149 UTC at 3.5°. This TBSS, indicative of a hail core was able to be tracked descending towards the surface in the few minutes preceding the largest MESH at the surface, as the TBSS appeared at the 2.4° elevation angle at 2141 UTC and extended down radial at 2144 UTC before beginning to dissipate. It was also observable on the 1.4° elevation angle starting at 2141 UTC, but was not as evident at the 0.9° elevation angle.

The mid-levels of the Katie supercell also had a prominent BWER in the 20 min preceding hailfall, along with associated Z_{DR} and ρ_{hv} rings. These features were best observed at the 3.5° elevation angle, so observations will be focused at this elevation. The BWER first appears briefly at 2122 UTC, before dissipating at 2123 UTC. At 2128 UTC, it begins to reform, starting off as an open region that is filled in as a clear BWER by 2131 UTC (Figure 5.32 – 5.33). A small increase in Z_H resulted in a well defined BWER at 2133 UTC. Coupled with the development of the BWER was the development of the ρ_{hv} ring with a weak Z_{DR} ring, centered around the mesocyclone (Figure 5.30 – 5.31). The BWER then remains in a quasi-steady state for 5 min as a closed circulation centered about the mesocyclone. By 2138 UTC, the BWER at 3.5° begins to open back up again and an increase in Z_H at 2139 UTC resulted in the demise of the BWER. The ρ_{hv} field of reduced values persists after the BWER collapses, but the structure of a half ring dissipates with the collapse of the BWER. The BWER briefly reappeared at 2146 UTC, before dissipating again post-hailfall.

In the low-levels (0.5°), Z_{DR} gave one of the best precursor signals to upcoming hailfall through the growth and decay of a Z_{DR} arc. This arc seemed to have develop and be most notable initially at 2125 UTC, closer to the left side of the forward
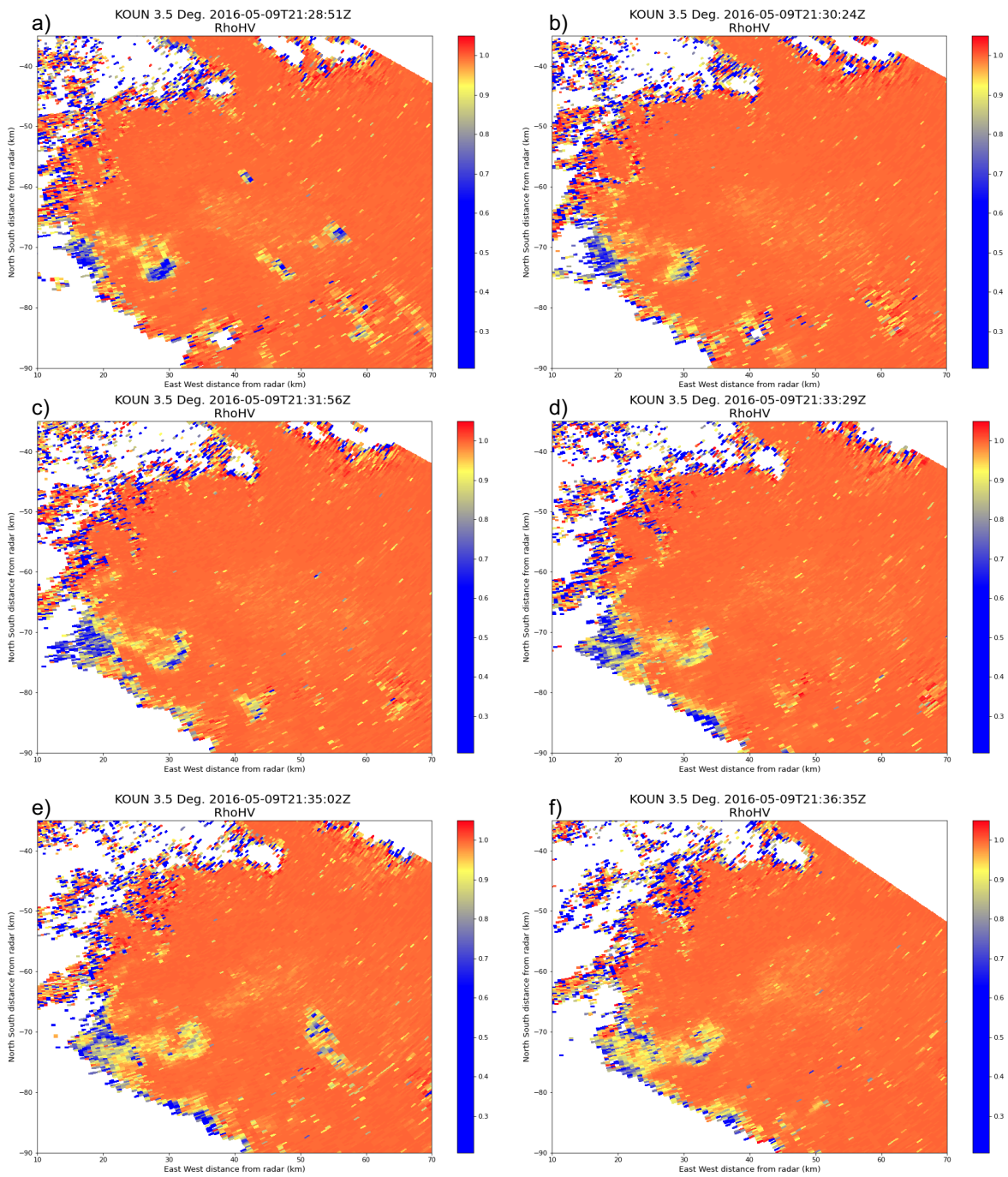
Figure 5.30: PPIs of ρ_{hv} along the 3.5° elevation angle for the 9 May 2016 Katie, OK supercell from 2128 – 2136 UTC.
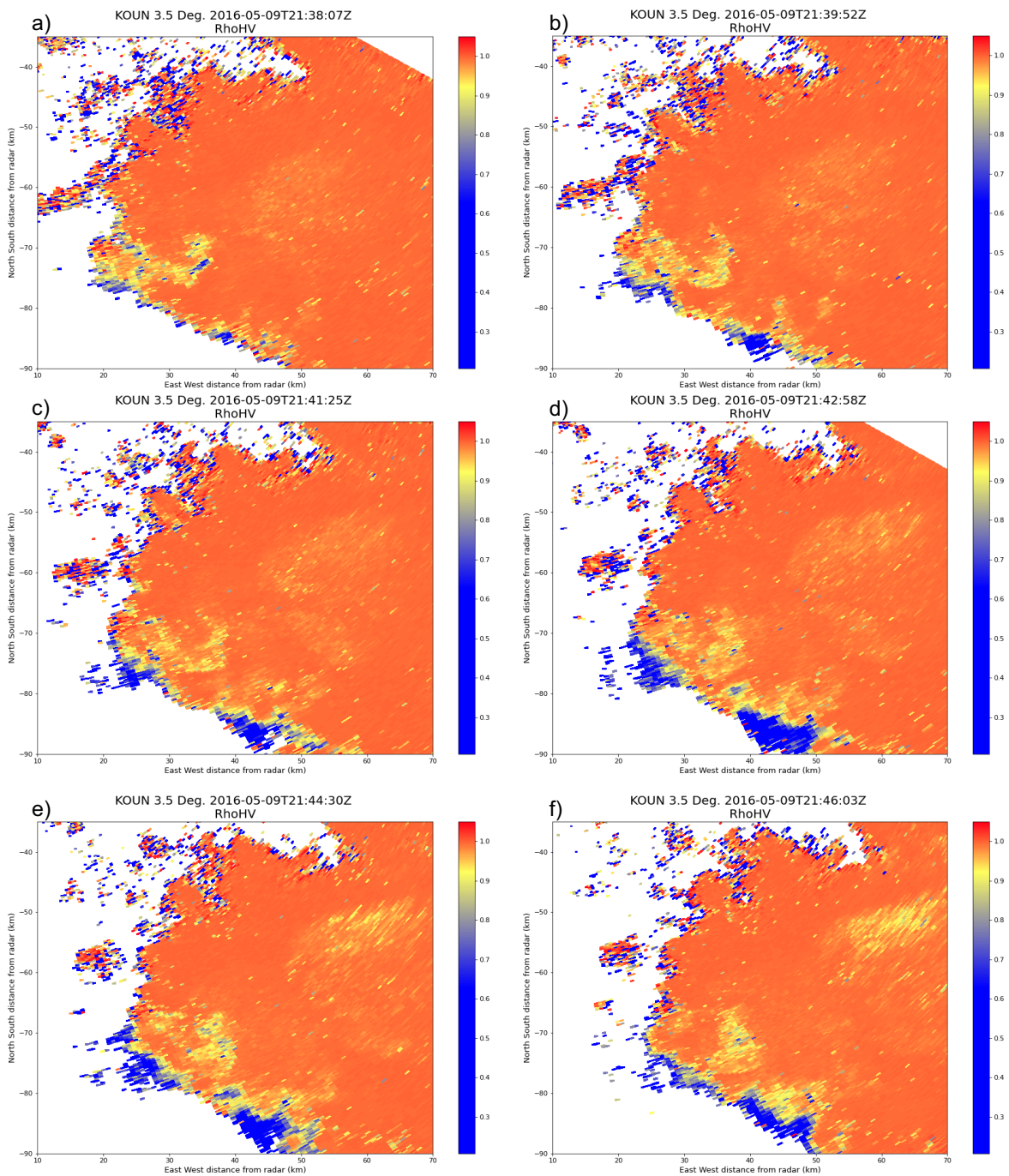
Figure 5.31: Same as Figure 5.30, but from 2138 – 2146 UTC.
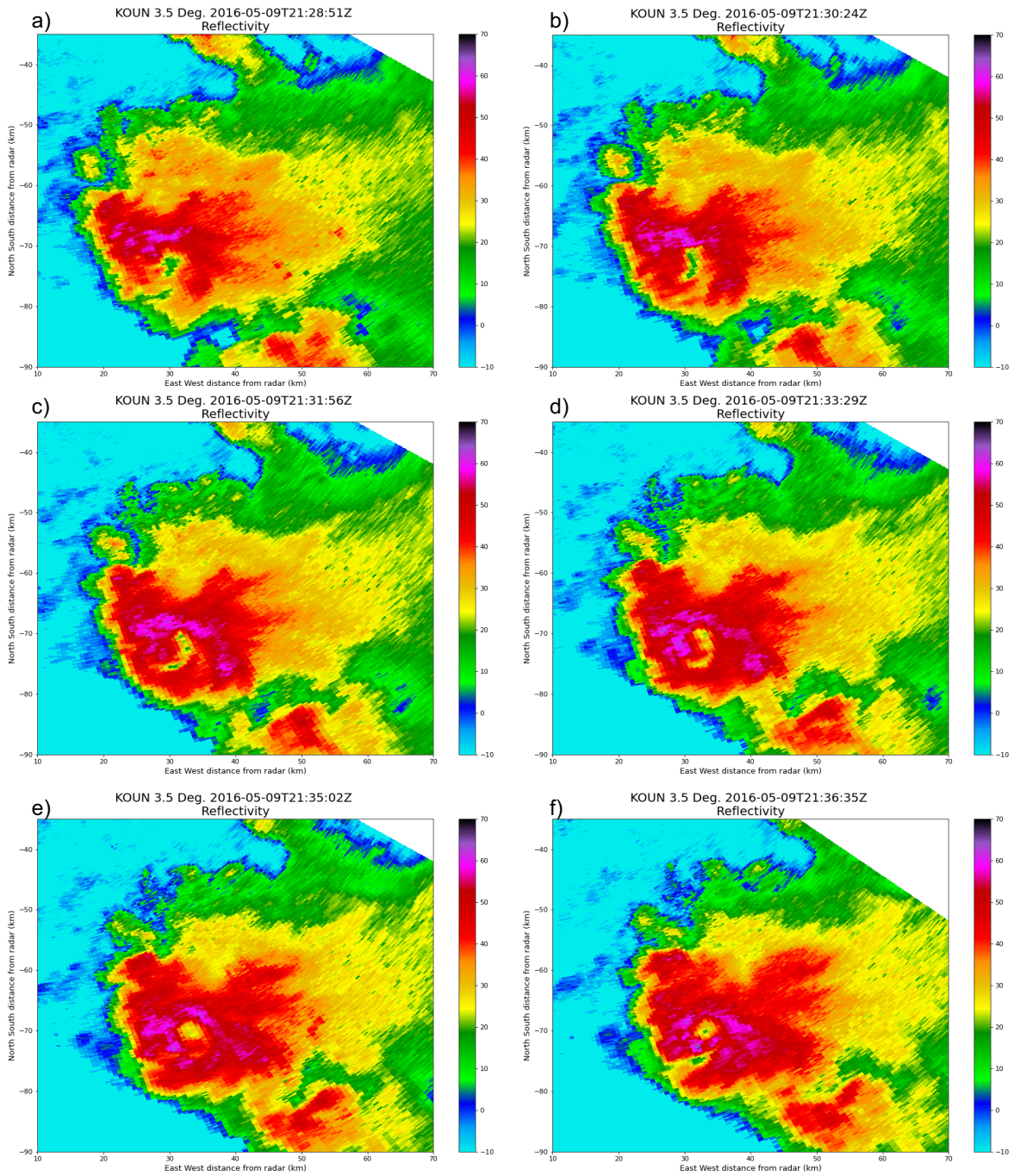
Figure 5.32: PPIs of Z_H along the 3.5° elevation angle for the 9 May 2016 Katie, OK supercell from 2128 – 2136 UTC.
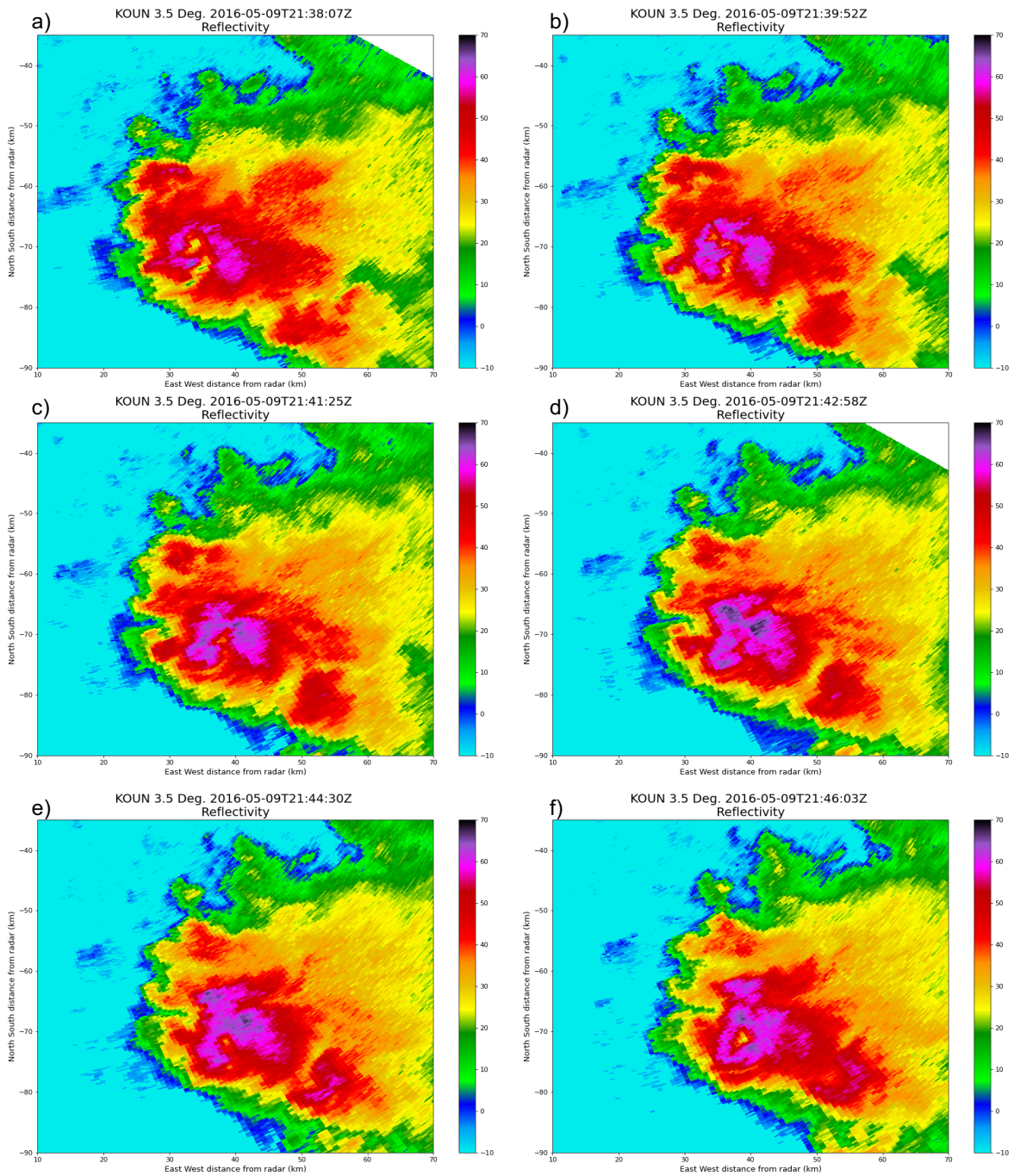
Figure 5.33: Same as Figure 5.32, but from 2138 – 2146 UTC.
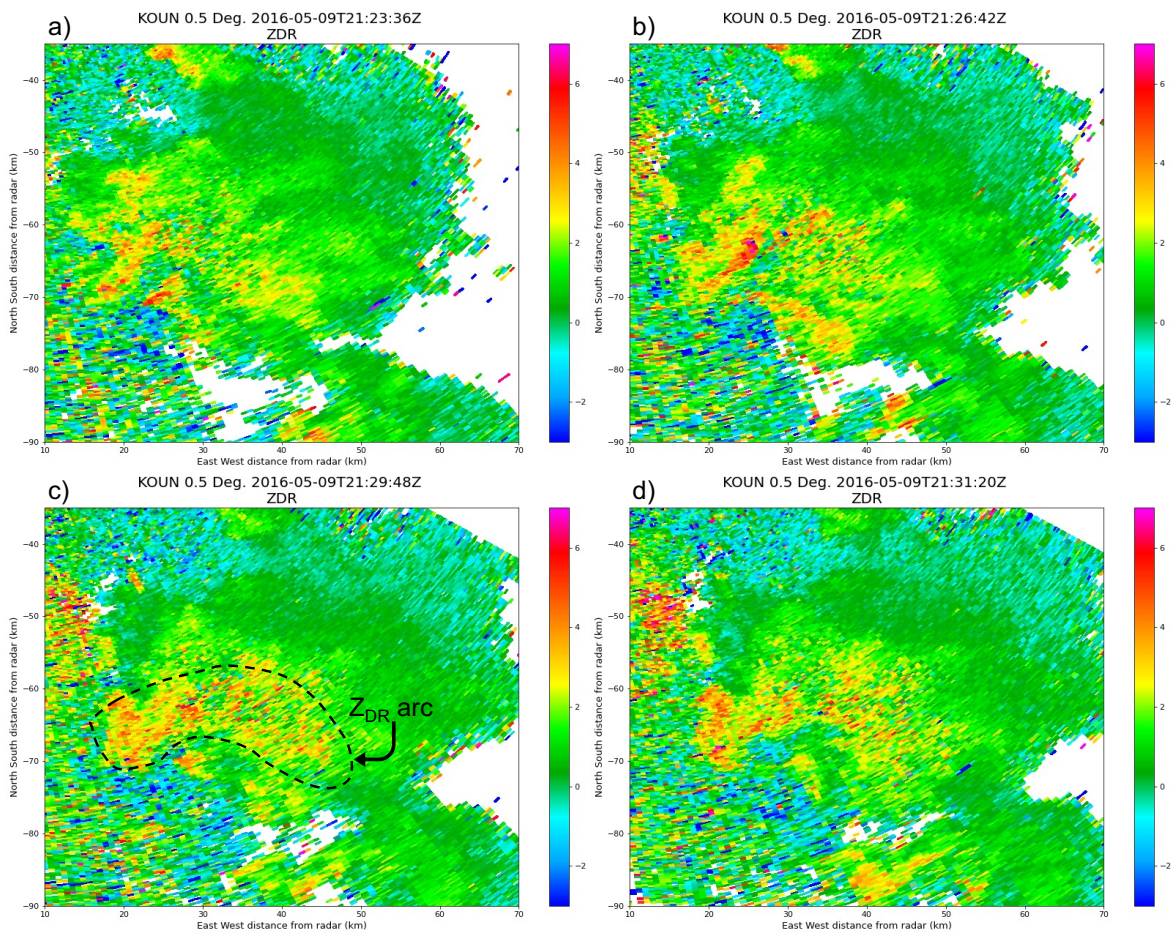
Figure 5.34: PPIs of Z_{DR} at the 0.5° elevation angle on 9 May 2016 from 2125 – 2129 UTC.

flank (Figure 5.34b). This arc continues developing and expanding so that by 2128 UTC, positive Z_{DR} returns within the forward flank span the entirety, with the best concentration along the left side (Figure 5.34c). Negative Z_{DR} returns were also present within this region, which may be lingering tornadic debris. This feature remains in a quasi-steady state until 2137 UTC, at which point the hook echo of the supercell is present even on Z_{DR} (Figure 5.35). By the start of the hail fallout time at 2139 UTC, a prominent ribbon of Z_{DR} <0 dB is present along the forward flank, which is co-located
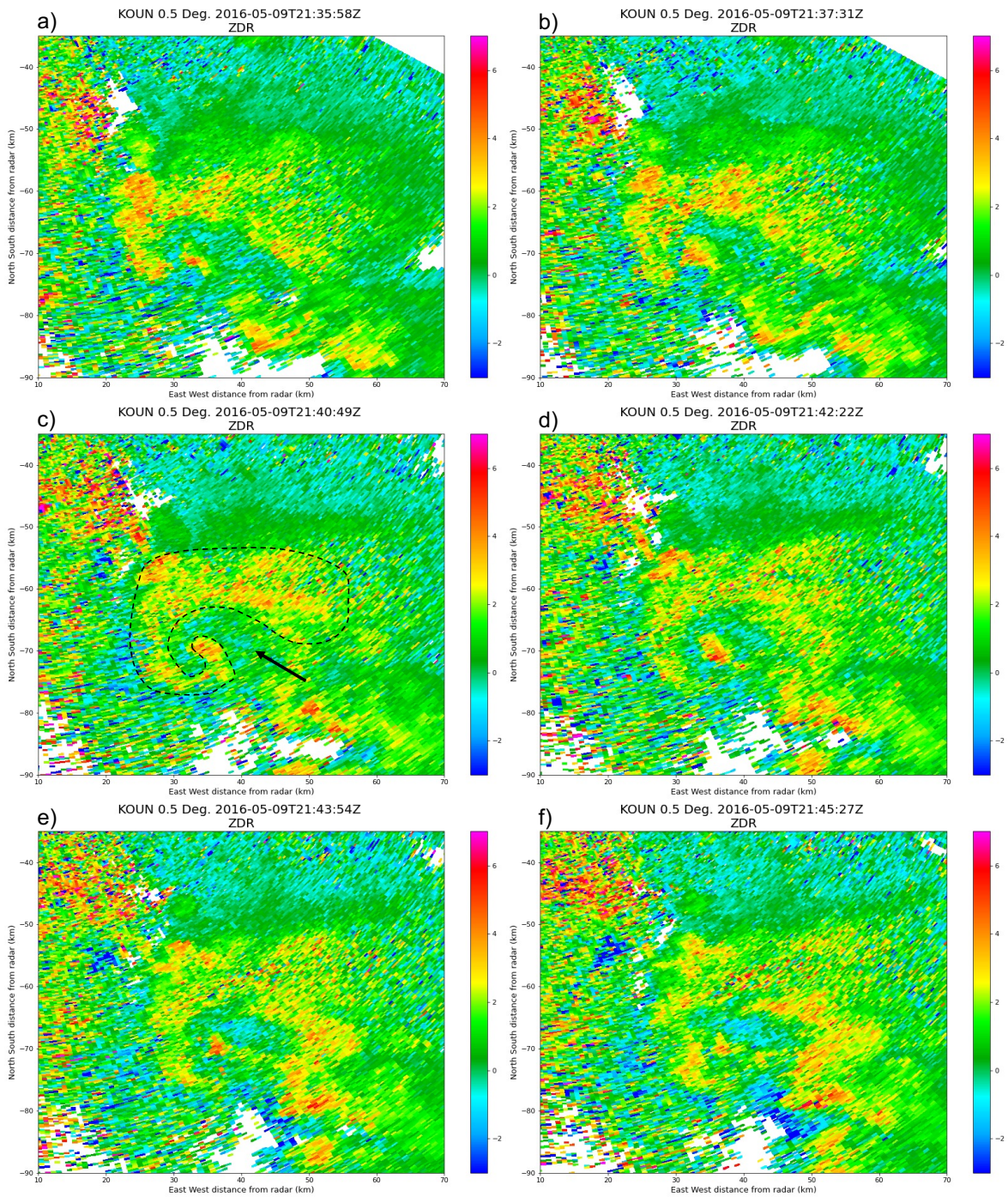
Figure 5.35: Same as Figure 5.34, but from 2136 – 2144 UTC. The dashed black line in panel c) indicates the region of $Z_{DR} > 0$ dB and the arrow indicates the region with $Z_{DR} < 0$ dB.

with the highest Z_H, thus indicating a hail core of potentially large hydrometeors (Figure 5.35c).

The time evolution of the 50 and 60 dBZ echo tops compared to the time evolution of MESH are given in Figures 5.36 and 5.37, respectively. The 50 dBZ echo tops featured a local minima of 5.29 km at 2120 UTC, with the minima in MESH occurring at 2122 UTC. 2 local maxima in the 50 dBZ echo top, one at 2129 UTC and the other at 2139 UTC preceded the peak hailfall of MESH by approximately 15 and 5 min respectively. The 60 dBZ echo tops displayed a similar pattern as the 50 dBZ echo tops, with a local minima occurring before the local minima in MESH, at 2120 and 2122 UTC, respectively. The local maxima in 60 dBZ echo tops occurred beginning at 2136 UTC, or 8 min before the peak in MESH. Of all the cases presented within this study, the echo top - MESH relationship here appears to have the most correlation and potential utility in serving as a pre-cursor signature for hailfall. Additionally, using the graupel and hail classification reveals an increase in the calculated hail core area preceding the peak hail fallout. Interestingly, the descent of this hail core is observable in Figure 5.38 as the largest magnitude of the area gradually slopes in the +time direction, which is indicative of the feature descending. In this case as well, the peak in area continued following the peak hail fallout, but the signals of a developing, descending, hail core were evident approximately 10 min before.

5.3.3 Hail Signatures

Low-level Z_{DR} during the hail fallout time provides a clear visual of the low-level microphysical processes occurring within the supercell. Starting at the peak hailfall time period at 2139 UTC, a clear separation of the $Z_{DR} <0$ dB and the $Z_{DR} >0$ dB
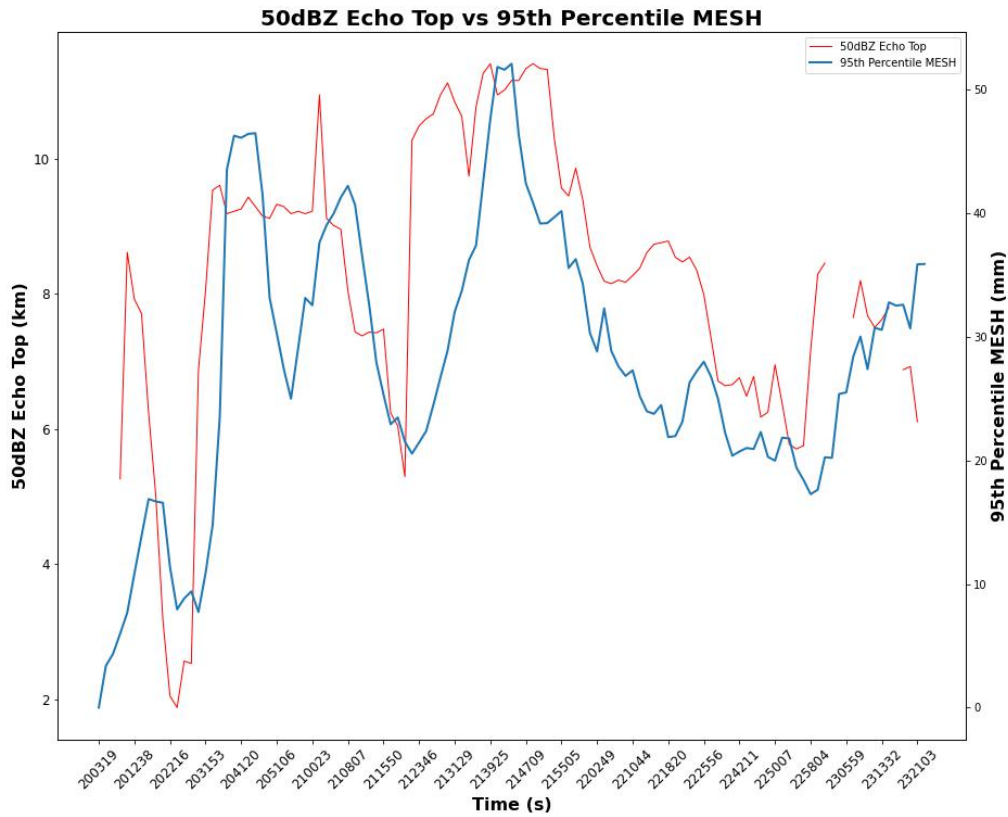
Figure 5.36: Time series of the 50 dBZ echo tops (red) and the 95th percentile MESH (blue) for the 9 May 2016 Katie, OK supercell.

existed along the forward flank of the supercell (Figure 5.35c). The Z_{DR} <0 dB is assumed to be the result of large hailstones reaching the surface, whereas the Z_{DR} >0 dB is the result of large drops and/or tornadic debris. Within the next 5 min, both of these features are advected gradually into the rear flank of the supercell, which is most prominent for the Z_{DR} >0 dB returns, as this region gradually weakens as it spreads out across the rear flank. Additionally, in a process similar to that described in Tanamachi and Heinselman (2016), this hail fallout time period caused the Z_{DR} arc to dissipate within this 5 min time frame (Figure 5.35f).
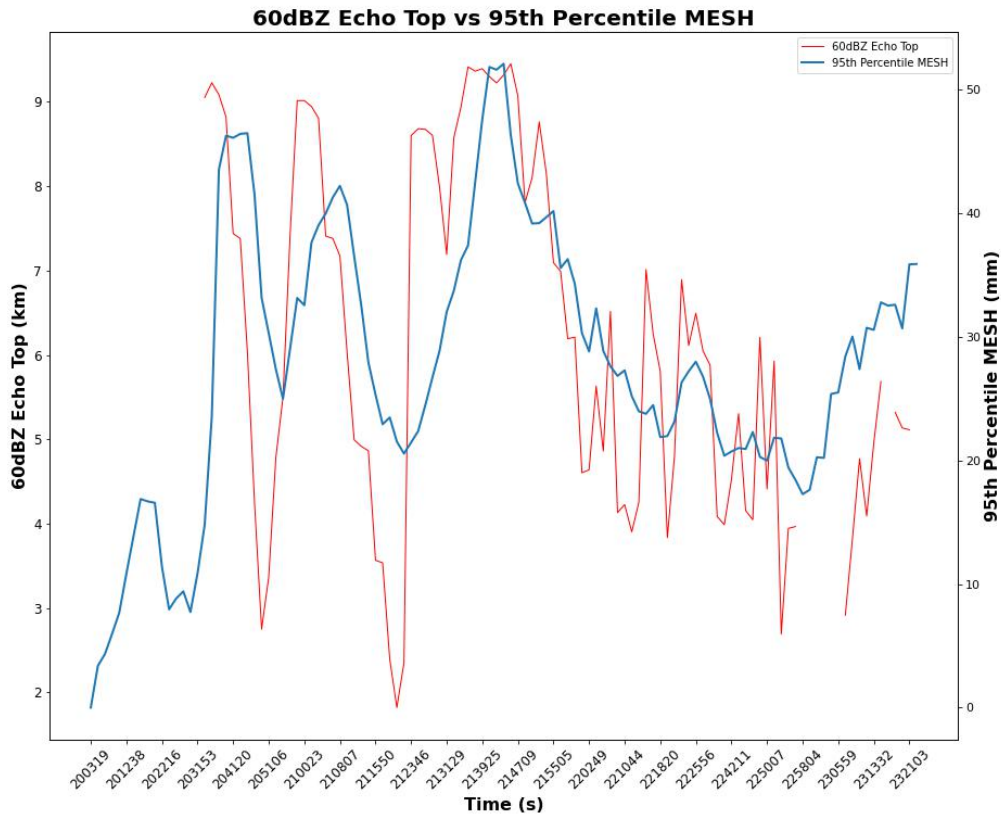
Figure 5.37: Time series of the 60 dBZ echo tops (red) and the 95$^\text{th}$ percentile MESH (blue) for the 9 May 2016 Katie, OK supercell.

This storm also featured a descending hail core, though it was weak in appearance, especially when compared to other hail fallout signatures noted in this study. The descending hail was noted as a core of Z_H >65 dBZ, embedded within a field of Z_H near 50 – 60 dBZ, around 2142 UTC. Due to its weak and the fact that it was deeply embedded within the rain shaft, cross sections of the core are not included. The core arrived at the surface around 2144 – 2145 UTC, best noted as a peak in the 0.9° elevation angle Z_H (Figure 5.39). Co-located with this intensification of Z_H at the low-levels was Z_DR returns <0 dB, which can be assumed to be indicative of large hail (Figure 5.35). ρ_hv within these highest Z_H returns had a magnitude of 0.95 – 0.99,
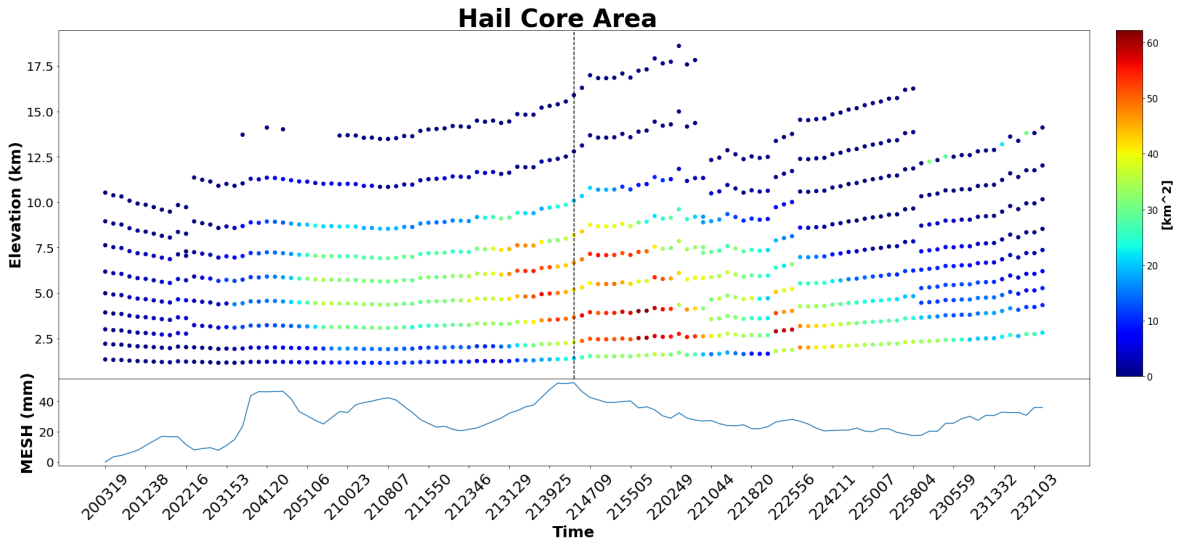
Figure 5.38: Time Height plot of the hail core area (top) along with the time evolution of MESH (bottom) for the 9 May 2016 Katie, OK supercell. The blank line in the top panel indicates the peak MESH time.

though such as been seen before, some of the lowest ρ_{hv} returns were spatially offset from the largest Z_H, located at the forward flank along the Z_H gradient. This lingered until 2148 UTC, at which point the MESH returns began to decline as well.

The time evolution of MESH for the Katie, OK supercell is provided in Figure 5.40. Of note for this supercell, NWS storm surveys determined the EF-4 tornadic intensity to occur from 2106 – 2127 UTC before momentarily cycling down and then re-intensifying into EF-3 strength beginning at 2134 UTC. The initial tornadic spinup at 2106 UTC was immediately preceded by a local maxima in MESH, and prior to this intensification, MESH displayed a cyclic nature to it, about 20 – 25 min per cycle. The EF-4 time period featured a local minima in MESH, with not much of a cyclic pattern to it, but MESH quickly increased after the tornado dissipated, resulting in the local maxima in MESH at 2139 UTC. After mesocyclogenesis occurred, an EF-3
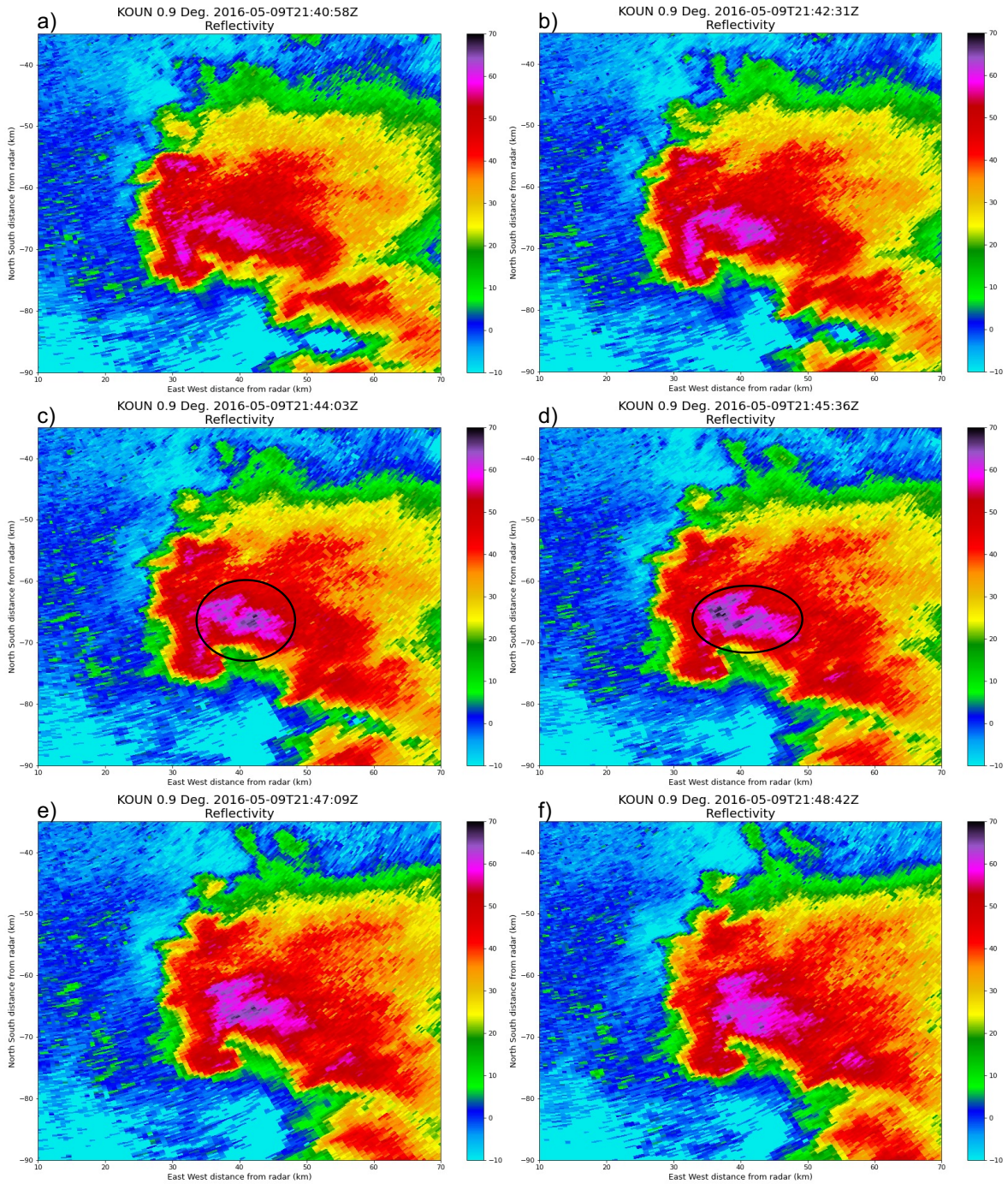
Figure 5.39: PPIs of the 0.9° elevation angle of Z_H on 9 May 2016 from 2140 – 2148 UTC near Katie, OK. The black ellipses in panels c) and d) indicate the location of the weak descending hail core, which was marked by a local region of Z_H >70 dBZ.
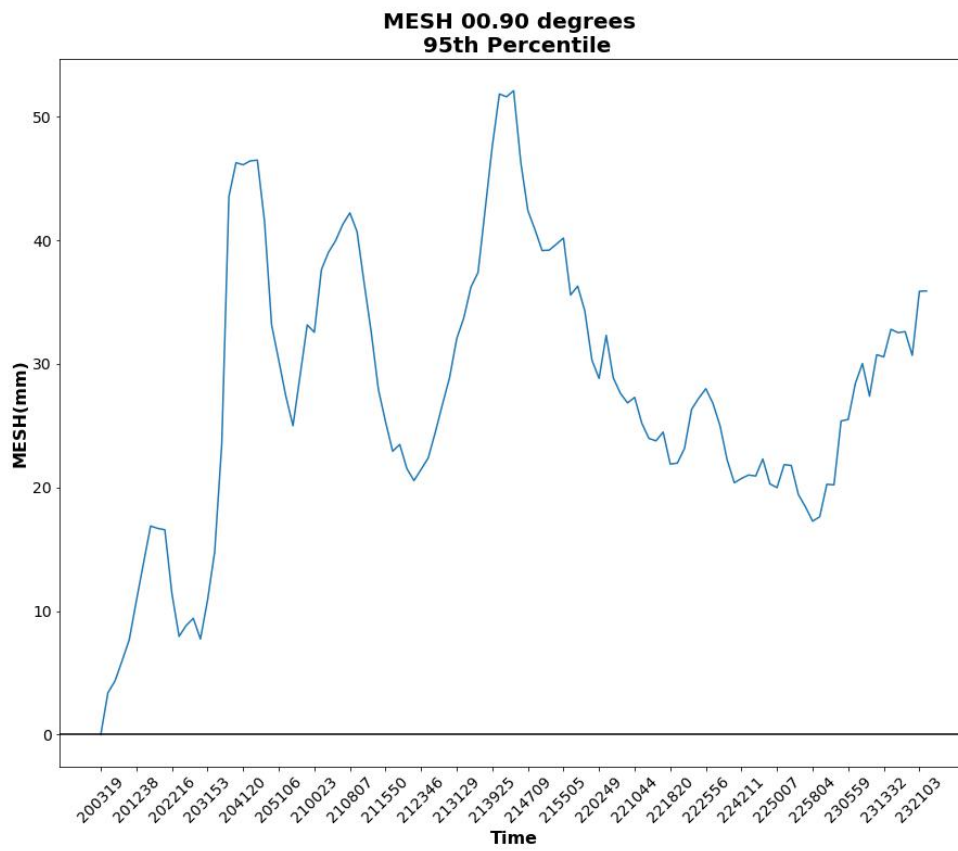
Figure 5.40: Time evolution of the 95$^{\text{th}}$ percentile MESH for the Katie, OK hail-producing supercell on 9 May 2016.

tornado formed. Most notable cyclic hail production ceased, and hail sizing estimates gradually declined.

5.4   Comparisons to NEXRAD Update Times

This study using KOUN revealed multiple pre-cursor signatures related to hail, such as the development and decay of the Z_{DR} arc, the mid-level TBSS and sidelobe spikes, BWERs and the rapid increases and descent of Z_H. The smaller scale evolution of these features were able to be observed in large part to the approximately 90-s update time that KOUN provided due to its volumetric sector scans. In order to evaluate the usefulness of future PAR systems as well as the rapid-scanning benefits for warning operations, the data were analyzed subjectively to match the update times of a NEXRAD system, updating on the order of 5 – 7 min. For the sake of brevity, the primary focus will be on the 2013 Edmond-Carney supercell described in Chapter 5.1.

From a PPI and RHI perspective, a traditional NEXRAD system will fail to capture some of the rapidly evolving features, especially surges in Z_H and Z_{DR} and descending hail cores. This is evident in the difference in update times and the gaps in data on KTLX, shown in Table 5.3. For the most part, KOUN had 2 – 3 additional volumetric scans compared to KTLX, which is a difference of 3 – 5 min of data. In even that short time frame, the structure and appearance of a storm can rapidly change, or in some cases, descending cores can be missed, such as the descending core observed with the Edmond, OK supercell.

In the case of the Edmond, OK supercell emulating the KOUN data to KTLX update times means that the evolution of the TBSS (such as the one at 5.1°) in Figure 5.5b will not be fully resolved. At that same elevation angle, the evolution of the change in the apparent mesocyclone structure in Figure 5.4a–d could be missed, though the

109

Table 5.3: Update times (UTC) based on the low-level elevation angles of KOUN versus KTLX from 19 May 2013 for the 2120 UTC hail fallout.

KOUN	2101	2103	2105	2107	2108	2110	2112	2114	2115	2117	2119	2120
KTLX	2102	–	2106	–	–	2110	–	–	2115	–	2119	–

change in structure (i.e., from a ring to isolated column) would still be observed. With regard to the Z_{DR} column, in a similar manner, utilizing slower update times like KTLX results in a loss of the evolution of the demise of the Z_{DR} column. In particular, the rapid demise that occurs from 2119 – 2122 UTC would potentially not be captured by a NEXRAD at all as this occurred within < 5 min (Figure 5.5d–f). From an application standpoint then, if studies like Kumjian et al. (2014) have shown utility in understanding and using the collapse of a Z_{DR} column as a signal to hail fallout, missing the evolution of this from an observational standpoint means that estimates of peak hailfall could be missed. This could then mean that estimating the timing of a hail cycle and when the next peak may occur could be incorrect, which would then be potentially tagged incorrectly in warning operations.

Additionally, approaching the peak MESH time, KTLX had the low-level scan update at 2115, 2119 and 2123 UTC. The hail fallout signature in KOUN for that same relative time frame in Figures 5.13 and 5.14 begins at 2115 UTC and reaches the surface at 2120 UTC. So, a NEXRAD like KTLX would only capture the core aloft and the core at the surface. It would fail to capture the descending properties, including the physical descent itself, which as we saw with the Hays, KS case in Chapter 4, means that the microphysical insight we can gain from the descending core is limited.

As another example of the impact of the rapid-scan observations from a PPI perspective, the Wynnewood TBSS evolved on a scale that a NEXRAD would capture, but the evolution and some of the descent of said TBSS would be missed. KTLX for that supercell in the lead time updated at 2257, 2304, 2310 and 2319 UTC, while the

TBSS on low-levels at least was observed from 2304 – 2312 UTC. In this case, KTLX captured the TBSS, but the almost the entirety of the rapid-evolution of the TBSS, including the transition from a dual-TBSS to singular elongated TBSS, was missed not only at the low-levels but also across most of the mid-levels. Similarly, this means then too that the descent of this TBSS was unable to be resolved in its fullest sense comparatively, which from an operational sense means that timing out the surface hail-fall is inaccurate and from a science perspective, the changes of the structure of the descending core are missed. Thus, rapid-scanning radar systems are needed not only for the scientific impact, but for the operational impact such as hailfall timing and verification, especially since the TBSS is assumed to be associated with a hail core.

The impacts of emulating a NEXRAD for calculated parameters, such as the hail core area follow a similar suit as the PPIs and RHIs. If we use the hail core area as an example in Figure 5.41, a few things of note arise. In this case, the timing of the expansion of the hail core area is still in line with what was observed with the 90 sec update times. This, however was not always the case, as the 2017 supercells had a time lag of 3 min between the 90 sec and 6 min update time (not shown), which may be an artifact of the user selected start times for temporally downsampling. But, it does show that the longer update times can give a time delay of a few minutes, relatively speaking on when the mid-level hail core area begins to expand.

The time evolution of MESH with NEXRAD update times is provided in Figure 5.42. Compared to the 90 sec update time from KOUN in Figure 5.15, the NEXRAD time series fails to capture some of the small-scale features of the evolution of MESH, such as secondary peaks. Additionally, the occurrence of the peak MESH time is missed using the 6 min update times, which is a pattern that was noted across all KOUN storms. While for this analysis, some of this is certainly influenced by the user
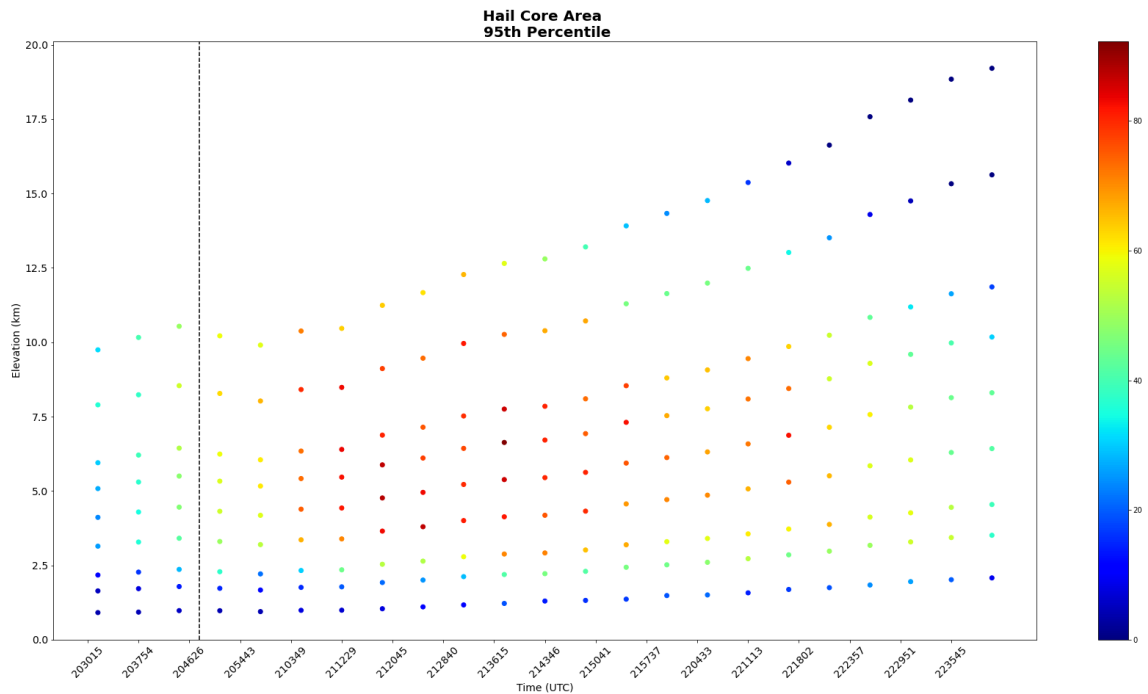
Figure 5.41: Time-Height plot of the hail core area with the graupel and hail classes for the Edmond, OK supercell on 19 May 2013, with update times of approximately 6 min in order to emulate a NEXRAD update time. Similar to Figure 5.10, the dashed black line indicates the peak MESH time.

selection of the start time to begin temporally downsampling the data, the general short lived nature of these peak MESH times means that they can and often may be missed in our present operations.

This general trend of a time lag in pre-cursor signatures and loss of small scale perturbations occurred across most facets of the data for the derived parameters. The overarching pattern generally persisted, but not always, and in some cases, its the small perturbations that from a science perspective especially may prove to be useful and beneficial in our observational understanding of hailstorms, if not severe convective storms as a whole. As such, the time series and time-heights combined with the PPI and RHI analysis argue the need for more in depth work with rapid-scan radar systems, and for an operational standpoint, more faster scanning S-band systems (and associated
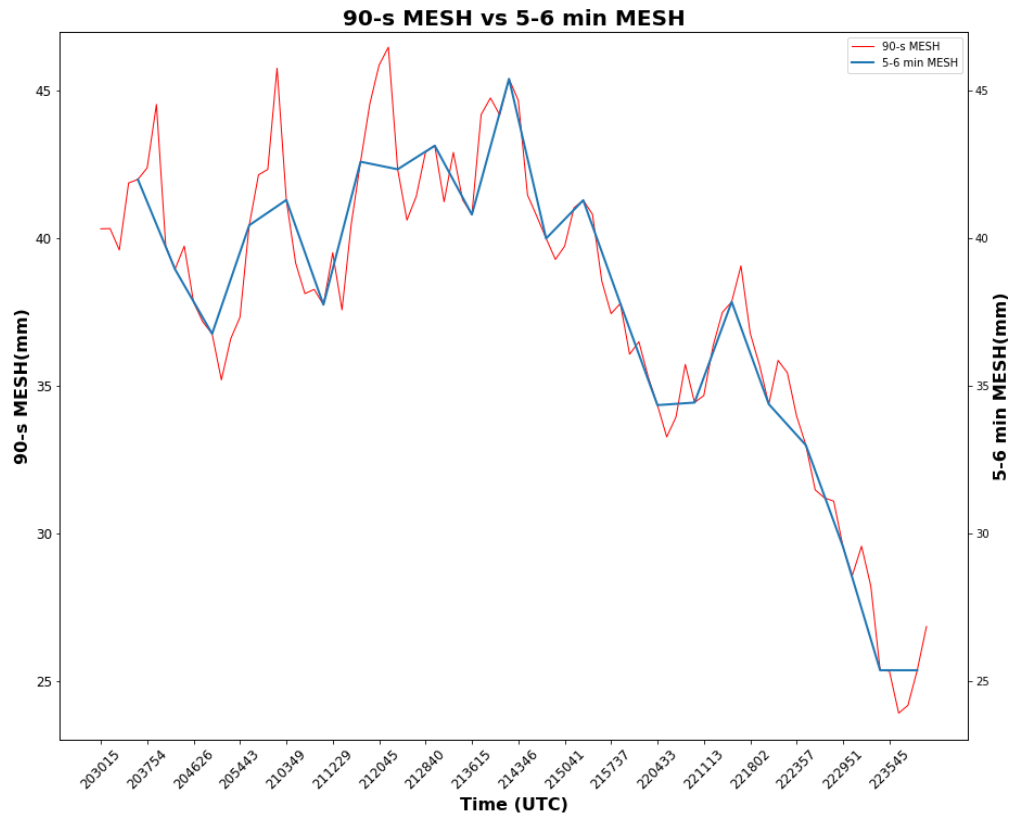
Figure 5.42: Time Series of the 95th percentile MESH for the Edmond, OK supercell on 19 May 2013. The red line indicates the 90-s MESH update times and the blue line indicates the 5 – 6 min update times of MESH.

studies in the process) are warranted in order to continue to improve our understanding and lead time of severe hail-producing supercells.

Chapter 6

Conclusions and Future Work

6.1 Summary of Findings

This study analyzed the rapidly-evolving features from 5 storms over 2 radar systems: 1 from RaXPol, and 4 from KOUN. RaXPol, a mobile X-Band system, provided full volumetric update times <1 min, allowing for the rapid growth of the Z_{DR} column and hail fallout to be resolved. The high spatial resolution and close proximity allowed for a descending hail core and its associated melting processes to be observed. This melting process combined with size sorting brought forth a stratification of the hail core into three distinct layers, outlined in Chapter 4.

KOUN, while not updating as rapidly as RaXPol, provided an operational view into the benefits of using more rapidly updating volumetric scans compared to the current NEXRAD system. The 90-sec updates in sector scan mode on 4 supercells of varying intensity and storm mode provided a range of pre-cursor signals and signatures associated with hail-producing storms. In a hail pre-cursor sense, this study did not find a singular, consistent radar signature to suggest an eventual increase in hail size, but numerous known features such as the growth and decay of the Z_{DR} column, the mid-level TBSS and sidelobe spikes, and changes to the mesocyclone appeared within the selected storms for this study. Increases to the mid-level hail core area, especially when factoring in graupel classifications to the HCA, occurred prior to the largest hail fallout, though the magnitude and duration before the peak hailfall remained relatively

114

inconsistent. The 50 and 60 dBZ echo tops showed some signals and potential utility, but again was not consistent across all storms. Hail fallout signatures, while not as clear cut across multiple radar variables, were able to be resolved with KOUN, but the <5 min descent implies that the current NEXRAD system may miss the entirety of these features.

While these descending hail cores may not be a pre-cursor signature in the sense that it occurred during hail growth, it still can serve as a beneficial tool in a forecasting and nowcasting sense, especially since this study supported prior studies such as Kumjian et al. (2021) which found that there was a cyclic behavior to hail production, particularly in the presence of a non-tornadic supercell. In this case, where the descending hail cores can be beneficial is to give forecasters a better estimate on the location of strong hail cores, which is especially important should the hail core occur in a rural area where storm reports are limited. Additionally, these descending hail cores can help forecasters pinpoint when a storm may begin cycling again so as to estimate when they may expect to see an increase in hail sizing, which will better aid in the warning operations, especially for significant hail producing storms.

One limitation to this study seemed to be tied to the size of the respective storm, mainly for the KOUN studies. The larger sized storms typically featured the most prominent signatures and generally also the most pre-cursor signatures to peak hail fallout. Smaller storms, such as Seminole and Wynnewood, featured much less notable pre-cursor signatures and sometimes were only observable as general storm structure changes, as opposed to microphysical changes. Of note as well is the limitation in the calculations of the echo tops and MESH. As mentioned, mis-calculations within the echo tops may have occurred due to KOUN either not topping out the storm or due to the storm top occurring between elevation angles. This also resulted in the potential for errors in the MESH calculations as well, as MESH is a result of the vertical integration

of Z_H. However, since MESH was used mainly for analyzing temporal trends and identifying peaks for PPI analysis, this does not impact the overall results from this study.

6.2 Applications to Future PAR Systems

This study not only highlights the continued need for rapid-scanning radar observations of hail-producing storms, but it gives an understanding of potential future applications to PAR-based studies. As PARs focus heavily on the vertical evolution of features such as convective storms, without the need for reconstructed RHIs, they serve as an ideal candidate for future radar-based convective studies. This is especially the case as PARs can provide vertically well-sampled data, which is necessary for proper calculations of parameters such as echo tops and MESH, which as we saw may have had miscalculations due to lapses in vertical data. Additionally, volumetric update times of <1 min that top out a storm are warranted to further the scientific progress being made on observational based studies of hail. By improving our scientific understanding, warning operations can also improve as more vertically focused pre-cursor signals may be able to be resolved, especially if the given PAR is the an S-band system, such as the Horus radar at the University of Oklahoma.

One such way to achieve these rapid evolving, vertical features, while still preserving the evolution of low-level features, such as the Z_{DR} arc, would involve using a combination of PPIs and RHIs, with the potential for using focusing on a single storm of interest, if there were a limited number within the observing domain. This concept was outlined recently in Tuftedal et al. (2022), where it was applied to the Stony Brook University SKYLER system. By applying this technique successfully, a full view of the storm, potentially on the order of seconds, will give a better picture of the dynamics

and interactions ongoing within a convective storm, such as the mid-level development of a hail core coupled with the lifecycle of a radar signature such as the Z_{DR} column.

One important factor scientists should consider for future studies involving dual-pol PAR systems is the storm size and storm mode. As this study showed, the size of the storm made an impact on the resolvability of pre-cursor signals, such as the development of a Z_{DR} column. As such, focus on marginal cases, and in particular storms that are smaller in area, should be given particular attention. In doing this, these storms can be used to test the practicality of future PAR networks and can further evaluate the benefits and limitations of these systems across a facet of storms, not just on the largest, most impactful storms.

6.3   Future Work

Since this study did not show one signature that appears in all results, an expansion of the number of storms analyzed is needed. In particular, emphasis should be placed on looking for large-scale repeatability, with comparisons to the storm environment, storm mode, and geographic location, as this study was only focused on central OK supercells. One potential avenue with this as well could involve applying a rapid-scanning dual-Doppler analysis of these storms in order to better analyze the impacts of the changes of the updraft on hail production in an observational sense.

One possible avenue of future and continuing work involves taking a deeper exploration into the nature of the cyclic behavior of hail-producing supercells and their connection to storm mode. Specifically, work trying to understand why some storms have a cyclic behavior and why some don't is needed. This pattern has been noted in the past, such as in Kumjian et al. (2021), but controlling factors, such as environmental influences or storm dynamics, remain a more limited understanding.

Most importantly, future work should place emphasis on using rapid-scanning dual-pol radar observation, in particular with current and future PAR networks. In particular, the Horus radar at the University of Oklahoma is presently in its final stages of production, with initial testing already underway (Palmer et al. 2019; Bodine et al. 2022). Future systems such as Horus will not only benefit the scientific community, but also the operational community, with the ultimate goal to increase forecasters conceptual model of hail production, thereby improving warning time and resilience against hailstorms.

Reference List

Allen, J. T., I. M. Giammanco, M. R. Kumjian, H. Jurgen Punge, Q. Zhang, P. Groen-emeijer, M. Kunz, and K. Ortega, 2020: Understanding Hail in the Earth System. *Reviews of Geophysics*, **58 (1)**, 1–49, https://doi.org/10.1029/2019RG000665.

Allen, J. T., M. K. Tippett, Y. Kaheil, A. H. Sobel, C. Lepore, S. Nong, and A. Muehlbauer, 2017: An extreme value model for U.S. hail size. *Monthly Weather Review*, **145 (11)**, 4501–4519, https://doi.org/10.1175/MWR-D-17-0119.1.

Allen, J. T., M. K. Tippett, and A. H. Sobel, 2015: An empirical model relating U.S. monthly hail occurrence to large-scale meteorological environment. *Journal of Advances in Modeling Earth Systems*, **6**, 513–526, https://doi.org/10.1002/2015MS000470.Received.

Barge, B., G. A. Isaac, W. Impacts, and C. Incorporated, 1973: The shape of Alberta hailstones. **(January 1973)**.

Blair, S. F., D. R. Deroche, J. M. Boustead, J. W. Leighton, B. L. Barjenbruch, and W. P. Gargan, 2011: A Radar-Based Assesment of the Detectability of Giant Hail. *Electronic J. Severe Storms Meteor.*, **6 (7)**, 1–30.

Blair, S. F., and Coauthors, 2017: High-resolution hail observations: Implications for NWS warning operations. *Weather and Forecasting*, **32 (3)**, 1101–1119, https://doi.org/10.1175/WAF-D-16-0203.1.

Bodine, D., and Coauthors, 2022: Examining the benefits of a future operational phased array radar network in the united states using rapid-scan radar observations and numerical simulations. *11th European Conference on Radar in Meteorology and Hydrology*, Locarno, Switzerland.

Bowden, K. A., P. L. Heinselman, D. M. Kingfield, and R. P. Thomas, 2015: Impacts of phased-array radar data on forecaster performance during severe hail and wind events. *Weather and Forecasting*, **30 (2)**, 389–404, https://doi.org/10.1175/WAF-D-14-00101.1.

Bringi, V. N., T. Seliga, and K. Aydin, 1984: Hail Detection with a Differential Reflectivity Radar. *Science*, **(September)**, 1145–1148.

Brooks, H. E., J. W. Lee, and J. P. Craven, 2003: The spatial distribution of severe thunderstorm and tornado environments from global reanalysis data. *Atmospheric Research*, **67-68**, 73–94, https://doi.org/10.1016/S0169-8095(03)00045-0.

Brown-Giammanco, T., and I. Giammanco, 2018: An overview of the insurance institute for business and home safety's hail research program. *29th Conference on Severe Local Storms*, Stowe, VT, Oral Presentation.

Conway, J., and D. S. Zrnic, 1993: A Study of Embryo Production and Hail Growth Using Dual-Doppler and Multiparameter Radars. *Monthly Weather Review*, **121**, 2511–2528.

Dawson, D. T., E. R. Mansell, Y. Jung, L. J. Wicker, M. R. Kumjian, and M. Xue, 2014: Low-level ZDR signatures in supercell forward flanks: The role of size sorting and melting of hail. *Journal of the Atmospheric Sciences*, **71 (1)**, 276–299, https://doi.org/10.1175/JAS-D-13-0118.1.

Dennis, E. J., and M. R. Kumjian, 2017: The impact of vertical wind shear on hail growth in simulated supercells. *Journal of the Atmospheric Sciences*, **74 (3)**, 641–663, https://doi.org/10.1175/JAS-D-16-0066.1.

Eilts, M., and Coauthors, 1996: Severe weather warning decision support system. *18th Conference on Severe Local Storms*, American Meteorological Society, San Francisco, CA, 536–540.

Foote, G. B., 1984: A Study of Hail Growth Utilizing Observed Storm Conditions. *Journal of Applied Meteorology and Climatology*, **23 (1)**, 84–101, https://doi.org/10.1175/1520-0450(1984)023⟨0084:ASOHGU⟩2.0.CO;2, URL https://journals.ametsoc.org/view/journals/apme/23/1/1520-0450_1984_023_0084_asohgu_2_0_co_2.xml.

Giammanco, I. M., B. R. Maiden, H. E. Estes, and T. M. Brown-Giammanco, 2017: Using 3D laser scanning technology to create digital models of hailstones. *Bulletin of the American Meteorological Society*, **98 (7)**, 1341–1347, https://doi.org/10.1175/BAMS-D-15-00314.1.

Goyer, G., 1970: The testing of airborne infrared detection systems for mapping hail-swaths and measuring hailfall coverage at the ground. the joint hail research project-summer 1969.

Gunturi, P., and M. K. Tippett, 2017: Managing severe thunderstorm risk: Impact of ENSO on U.S. tornado and hail frequencies. Willis Re, Minneapolis, MN, USA.

Heinselman, P. L., D. L. Priegnitz, K. L. Manross, T. M. Smith, and R. W. Adams, 2008: Rapid sampling of severe storms by the National Weather Radar Testbed Phased Array Radar. *Weather and Forecasting*, **23 (5)**, 808–824, https://doi.org/10.1175/2008WAF2007071.1.

Helmus, J. J., and S. M. Collis, 2016: The Python ARM Radar Toolkit (Py-ART), a Library for Working with Weather Radar Data in the Python Programming Language. *Journal of Open Research Software*, **4 (1)**, 25, https://doi.org/10.5334/jors.119.

Heymsfield, A., and R. Wright, 2014: Graupel and hail terminal velocities: Does a "Supercritical" Reynolds number apply? *Journal of the Atmospheric Sciences*, **71 (9)**, 3392–3403, https://doi.org/10.1175/JAS-D-14-0034.1.

Heymsfield, A. J., 1982: A Comparative Study of the Rates of Development of Potential Graupel and Hail Embryos in High Plains Storms. *Journal of Atmospheric Sciences*, **39 (12)**, 2867–2897, https://doi.org/10.1175/1520-0469(1982)039⟨2867:ACSOTR⟩ 2.0.CO;2, URL https://journals.ametsoc.org/view/journals/atsc/39/12/1520-0469_ 1982_039_2867_acsotr_2_0_co_2.xml.

Isom, B., and Coauthors, 2013: The atmospheric imaging radar: Simultaneous volumetric observations using a phased array weather radar. *Journal of Atmospheric and Oceanic Technology*, **30 (4)**, 655–675, https://doi.org/10.1175/jtech-d-12-00063.1.

Johnson, A., and K. Sugden, 2014: Evaluation of Sounding-Derived Thermodynamic and Wind-Related Parameters Associated with Large Hail Events. *E-Journal of Severe Storms Meteorology*, **9 (5)**, 1–42, URL http://www.ejssm.org/ojs/index.php/ ejssm/article/viewArticle/137.

Knight, C. A., D. H. Ehhalt, N. Roper, and N. C. Knight, 1975: Radial and Tangential Variation of Deuterium in Hailstones. *Journal of Atmospheric Sciences*, **32 (10)**, 1990–2000, https://doi.org/10.1175/1520-0469(1975)032⟨1990:RATVOD⟩ 2.0.CO;2, URL https://journals.ametsoc.org/view/journals/atsc/32/10/1520-0469_ 1975_032_1990_ratvod_2_0_co_2.xml.

Knight, C. A., and N. C. Knight, 1970: Hailstone Embryos. *Journal of Atmospheric Sciences*, **27 (4)**, 659–666, https://doi.org/10.1175/1520-0469(1970)027⟨0659:HE⟩ 2.0.CO;2, URL https://journals.ametsoc.org/view/journals/atsc/27/4/1520-0469_ 1970_027_0659_he_2_0_co_2.xml.

Knight, C. A., and N. C. Knight, 1970a: Lobe Structures of Hailstones. *Journal of Atmospheric Sciences*, **27 (4)**, 667–671, https://doi.org/10.1175/1520-0469(1970) 027⟨0667:LSOH⟩2.0.CO;2, URL https://journals.ametsoc.org/view/journals/atsc/ 27/4/1520-0469_1970_027_0667_lsoh_2_0_co_2.xml.

Knight, C. A., and N. C. Knight, 2005: Very Large Hailstones From Aurora, Nebraska. *Bulletin of the American Meteorological Society*, **86 (12)**, 1773– 1782, https://doi.org/10.1175/BAMS-86-12-1773, URL https://journals.ametsoc. org/view/journals/bams/86/12/bams-86-12-1773.xml.

Knight, N. C., 1981: The Climatology of Hailstone Embryos. *Journal of Applied Meteorology and Climatology*, **20 (7)**, 750–755, https://doi.org/10.1175/ 1520-0450(1981)020⟨0750:TCOHE⟩2.0.CO;2, URL https://journals.ametsoc.org/ view/journals/apme/20/7/1520-0450_1981_020_0750_tcohe_2_0_co_2.xml.

Knight, N. C., 1986: Hailstone Shape Factor and Its Relation to Radar Interpretation of Hail. *Journal of Applied Meteorology and Climatology*, **25 (12)**, 1956–1958, https://doi.org/10.1175/1520-0450(1986)025⟨1956:HSFAIR⟩2.0.CO;2, URL https://journals.ametsoc.org/view/journals/apme/25/12/1520-0450_1986_025_1956_hsfair_2_0_co_2.xml.

Kumjian, M., 2013a: Principles and applications of dual-polarization weather radar. Part I: Description of the polarimetric radar variables. *Journal of Operational Meteorology*, **1 (19)**, 226–242, https://doi.org/10.15191/nwajom.2013.0119.

Kumjian, M., 2013c: Principles and applications of dual-polarization weather radar. Part III: Artifacts. *Journal of Operational Meteorology*, **1 (21)**, 265–274, https://doi.org/10.15191/nwajom.2013.0121.

Kumjian, M. R., 2013b: Principles and applications of dual-polarization weather radar. Part II: Warm and cold season applications. *Journal of Operational Meteorology*, **1 (20)**, 243–264, URL http://www.nwas.org/jom/articles/2013/2013-JOM20/2013-JOM20.pdf%5Cnpapers3://publication/uuid/8F595571-BC5F-452A-9C69-4A3CD6A953FC.

Kumjian, M. R., A. P. Khain, N. Benmoshe, E. Ilotoviz, A. V. Ryzhkov, and V. T. Phillips, 2014: The anatomy and physics of ZDR columns: Investigating a polarimetric radar signature with a spectral bin microphysical model. *Journal of Applied Meteorology and Climatology*, **53 (7)**, 1820–1843, https://doi.org/10.1175/JAMC-D-13-0354.1.

Kumjian, M. R., Z. J. Lebo, and A. M. Ward, 2019: Storms producing large accumulations of small hail. *Journal of Applied Meteorology and Climatology*, **58 (2)**, 341–364, https://doi.org/10.1175/JAMC-D-18-0073.1.

Kumjian, M. R., K. Lombardo, and S. Loeffler, 2021: The Evolution of Hail Production in Simulated Supercell Storms. *Journal of the Atmospheric Sciences*, 1–76, https://doi.org/10.1175/jas-d-21-0034.1.

Kumjian, M. R., and A. V. Ryzhkov, 2008: Polarimetric signatures in supercell thunderstorms. *Journal of Applied Meteorology and Climatology*, **47 (7)**, 1940–1961, https://doi.org/10.1175/2007JAMC1874.1.

Kumjian, M. R., and A. V. Ryzhkov, 2010: The impact of evaporation on polarimetric characteristics of rain: Theoretical model and practical implications. *Journal of Applied Meteorology and Climatology*, **49 (6)**, 1247–1267, https://doi.org/10.1175/2010JAMC2243.1.

Kumjian, M. R., A. V. Ryzhkov, V. M. Melnikov, and T. J. Schuur, 2010: Rapid-scan super-resolution observations of a cyclic supercell with a dual-polarization

WSR-88D. *Monthly Weather Review*, **138 (10)**, 3762–3786, https://doi.org/10.1175/2010MWR3322.1.

Kumjian, M. R., and Coauthors, 2020: Gargantuan Hail in Argentina. *Bulletin of the American Meteorological Society*, **101 (8)**, E1241 – E1258, https://doi.org/10.1175/BAMS-D-19-0012.1, URL https://journals.ametsoc.org/view/journals/bams/101/8/bamsD190012.xml.

Kuster, C. M., J. C. Snyder, T. J. Schuur, T. T. Lindley, P. L. Heinselman, J. C. Furtado, J. W. Brogden, and R. Toomey, 2019: Rapid-update radar observations of ZDR column depth and its use in the warning decision process. *Weather and Forecasting*, **34 (4)**, 1173–1188, https://doi.org/10.1175/WAF-D-19-0024.1.

Lakshmanan, V., K. Hondl, C. K. Potvin, and D. Preignitz, 2013: An Improved Method for Estimating Radar Echo-Top Height. *Weather and Forecasting*, **28 (2)**, 481–488, https://doi.org/10.1175/WAF-D-12-00084.1, URL https://journals.ametsoc.org/view/journals/wefo/28/2/waf-d-12-00084{_}1.xml.

Lakshmanan, V., T. Smith, G. Stumpf, and K. Hondl, 2007: The Warning Decision Support System–Integrated Information. *Weather and Forecasting*, **22 (3)**, 596–612, https://doi.org/10.1175/WAF1009.1, URL https://journals.ametsoc.org/view/journals/wefo/22/3/waf1009{_}1.xml.

Lakshmanan, V., and A. Witt, 1997: A fuzzy logic approach to detecting severe updrafts. *AI Applications*, **11 (1)**, 1–12.

Lamb, D., and J. Verlinde, 2011: *Physics and chemistry of clouds*. Cambridge University Press, United Kingdom, https://doi.org/10.1017/CBO9780511976377.

Lemon, L. R., 1998: The radar "three-body scatter spike": An operational large-hail signature. *Weather and Forecasting*, **13 (2)**, 327–340, https://doi.org/10.1175/1520-0434(1998)013⟨0327:TRTBSS⟩2.0.CO;2.

Ludlam, F. H., 1958: *The hail problem*. Nubila, 13-96 pp.

Murillo, E. M., and C. R. Homeyer, 2019: Severe hail fall and hailstorm detection using remote sensing observations. *Journal of Applied Meteorology and Climatology*, **58 (5)**, 947–970, https://doi.org/10.1175/JAMC-D-18-0247.1.

Nelson, S. P., 1983: The influence of storm flow structure on hail growth. 1965–1983 pp., https://doi.org/10.1175/1520-0469(1983)040⟨1965:TIOSFS⟩2.0.CO;2.

Ortega, K. L., J. M. Krause, and A. V. Ryzhkov, 2016: Polarimetric radar characteristics of melting hail. Part III: Validation of the algorithm for hail size discrimination. *Journal of Applied Meteorology and Climatology*, **55 (4)**, 829–848, https://doi.org/10.1175/JAMC-D-15-0203.1.

Ortega, K. L., T. M. Smith, K. L. Manross, K. A. Scharfenberg, W. Arthur, A. G. Kolodziej, and J. J. Gourley, 2009: The severe hazards analysis and verification experiment. *Bulletin of the American Meteorological Society*, **90 (10)**, 1519–1530, https://doi.org/10.1175/2009BAMS2815.1.

Palmer, R. D., C. J. Fulton, J. Salazar, H. Sigmarsson, and M. Yeary, 2019: The "Horus" radar: An all-digital polarimetric phased array radar for multi-mission surveillanceitle. *35th Conference on Environmental Information Processing Technologies*, American Meteorological Society, Phoenix, AZ, URL https://ams.confex.com/ams/2019Annual/webprogram/Paper349962.html.

Park, H. S., A. V. Ryzhkov, D. S. Zrnić, and K. E. Kim, 2009: The hydrometeor classification algorithm for the polarimetric WSR-88D: Description and application to an MCS. *Weather and Forecasting*, **24 (3)**, 730–748, https://doi.org/10.1175/2008WAF2222205.1.

Pazmany, A. L., J. B. Mead, H. B. Bluestein, J. C. Snyder, and J. B. Houser, 2013: A mobile rapid-scanning X-band polarimetric (RaXPol) doppler radar system. *Journal of Atmospheric and Oceanic Technology*, **30 (7)**, 1398–1413, https://doi.org/10.1175/JTECH-D-12-00166.1.

Picca, J., and A. Ryzhkov, 2012: A dual-wavelength polarimetric analysis of the 16 may 2010 Oklahoma city extreme hailstorm. *Monthly Weather Review*, **140 (4)**, 1385–1403, https://doi.org/10.1175/MWR-D-11-00112.1.

Rasmussen, R. M., and Heymsfield, 1987: Melting and shedding of graupel and hail. Part I: Model Physics. 2754–2763 pp.

Rasmussen, R. M., V. Levizzani, and H. R. Pruppacher, 1984: A wind tunnel and theoretical study of the melting behavior of atmospheric ice particles. III: Experiment and theory for spherical ice particles of radius < 500 micrometers. *Journal of the Atmospheric Sciences*, **41 (3)**, 381–388, https://doi.org/10.1175/1520-0469(1984)041⟨0381:AWTATS⟩2.0.CO;2.

Rauber, R., and S. Nesbitt, 2018: *Radar Meteorology: A First Course*. https://doi.org/10.1002/9781118432662.

Ryzhkov, A. V., M. R. Kumjian, S. M. Ganson, and A. P. Khain, 2013a: Polarimetric radar characteristics of melting hail. Part I: Theoretical simulations using spectral microphysical modeling. *Journal of Applied Meteorology and Climatology*, **52 (12)**, 2849–2870, https://doi.org/10.1175/JAMC-D-13-073.1.

Ryzhkov, A. V., M. R. Kumjian, S. M. Ganson, and P. Zhang, 2013b: Polarimetric radar characteristics of melting hail. Part II: Practical implications. *Journal of Applied Meteorology and Climatology*, **52 (12)**, 2871–2886, https://doi.org/10.1175/JAMC-D-13-074.1.

Schumann, T., 1938: The theory of hailstone formation. *Quarterly Journal of the Royal Meteorological Society*, **64**, 3–21, https://doi.org/10.1002/qj.49706427303.

Shedd, L., M. R. Kumjian, I. Giammanco, T. Brown-Giammanco, and B. R. Maiden, 2021: Hailstone shapes. *Journal of the Atmospheric Sciences*, **78 (2)**, 639–652, https://doi.org/10.1175/JAS-D-20-0250.1.

Smith, T. M., and Coauthors, 2016: Multi-radar multi-sensor (MRMS) severe weather and aviation products: Initial operating capabilities. *Bulletin of the American Meteorological Society*, **97 (9)**, 1617–1630, URL https://www.jstor.org/stable/26243578.

Snyder, J. C., H. B. Bluestein, V. Venkatesh, and S. J. Frasier, 2013: Observations of polarimetric signatures in supercells by an X-band mobile Doppler radar. *Monthly Weather Review*, **141 (1)**, 3–29, https://doi.org/10.1175/MWR-D-12-00068.1.

Snyder, J. C., H. B. Bluestein, Z. B. Wienhoff, C. M. Kuster, and D. W. Reif, 2020: An Analysis of an Ostensible Anticyclonic Tornado from 9 May 2016 Using High-Resolution, Rapid-Scan Radar Data. *Weather and Forecasting*, **35 (5)**, 1685–1712, https://doi.org/10.1175/WAF-D-20-0055.1, URL https://journals.ametsoc.org/view/journals/wefo/35/5/wafD200055.xml.

Snyder, J. C., H. B. Bluestein, G. Zhang, and S. J. Frasier, 2010: Attenuation correction and hydrometeor classification of high-resolution, X-band, dual-polarized mobile radar measurements in severe convective storms. *Journal of Atmospheric and Oceanic Technology*, **27 (12)**, 1979–2001, https://doi.org/10.1175/2010JTECHA1356.1.

Straka, J., and D. S. Zrnić, 1993: An algorithm to deduce hydrometeor types and contents from multiparameter radar data. *26th Conf. on Radar Meteorology*, 513 – 516.

Tanamachi, R. L., and P. L. Heinselman, 2016: Rapid-scan, polarimetric observations of central Oklahoma severe storms on 31 May 2013. *Weather and Forecasting*, **31 (1)**, 19–42, https://doi.org/10.1175/WAF-D-15-0111.1.

Tuftedal, K. S., E. Luke, and P. Kollias, 2022: Best of both worlds: Applications of a mobile polarimetric phased-array radar system. *102nd American Meteorological Society Annual Meeting*, AMS.

Witt, A., D. W. Burgess, A. Seimon, J. T. Allen, J. C. Snyder, and H. B. Bluestein, 2018: Rapid-scan radar observations of an Oklahoma tornadic hailstorm producing giant hail. *Weather and Forecasting*, **33 (5)**, 1263–1282, https://doi.org/10.1175/WAF-D-18-0003.1.

Witt, A., M. D. Eilts, G. J. Stumpf, J. T. Johnson, E. D. Mitchell, and K. W. Thomas, 1998: An enhanced hail detection algorithm for the WSR-88D. *Weather and*

Forecasting, **13 (2)**, 286–303, https://doi.org/10.1175/1520-0434(1998)013⟨0286: AEHDAF⟩2.0.CO;2.

Zrnic, D. S., G. Zhang, V. Melnikov, and J. Andric, 2010: Three-body scattering and hail size. *Journal of Applied Meteorology and Climatology*, **49 (4)**, 687–700, https://doi.org/10.1175/2009JAMC2300.1.

Zrnić, D. S., 1987: Three-body scattering produces precipitation signature of special diagnostic value. *Radio Science*, **22 (01)**, 76–86, https://doi.org/10.1029/RS022i001p00076.